TIO2-EMBEDDED AG NANOCRYSTALS WITH TUNABLE PLASMON RESONANCE

A Dissertation

Submitted to the Graduate School

of the University of Notre Dame

in Partial Fulfillment of the Requirements

for the Degree of

Doctor of Philosophy

by

Vincenzo Balzano

Christopher Hinkle, Director

Graduate Program in Physics

Notre Dame, Indiana

August 2025

UNIVERSITÀ CATTOLICA DEL SACRO CUORE

UNIVERSITY OF NOTRE DAME

International PhD in Science – XXXVI Ciclo di Dottorato

TIO2-EMBEDDED AG NANOCRYSTALS WITH TUNABLE PLASMON RESONANCE

Dissertation

For the degree of

Doctor of Philosophy

by

Vincenzo Balzano

Supervisors:

Prof. Luca Gavioli

Prof. Christopher Hinkle

Academic Year 2024/2025

© Copyright 2025

Vincenzo Balzano

TIO2-EMBEDDED AG NANOCRYSTALS WITH TUNABLE PLASMON RESONANCE

Abstract

by

Vincenzo Balzano

Recent advancements in materials engineering have led to the development of novel composite systems that exploit plasmon-enhanced light matter interactions to significantly improve optical, electronical, and catalytic processes. These materials, which integrate plasmonic nanostructures with semiconductors, dielectrics, or 2D materials, enable unprecedented control over light absorption, charge carrier dynamics, and energy transfer. So far, the effectiveness of plasmonic structures in enhancing the local electric field has been confirmed by several theoretical, computational and experimental studies, and has brought drastic enhancements in a variety of light-matter interaction processes including fluorescence, Raman scattering, heat generation, photoacoustic effects, photocatalysis and solar energy conversion. Despite significant progress in the fabrication of plasmonic nanostructures, there are several limitations that hinder the scalability, precision and reproducibility of commonly used fabrication techniques. Nanolithography techniques such as electron beam lithography and nanoimprint lithography, for example, provide high spatial resolution and well-defined architectures, but are constrained by high costs, low throughputs, and challenges in large-area

patterning. On the other hand, chemical synthesis methods such as colloidal synthesis offer higher throughput, but often lack a precise control over the size, shape and composition of the nanostructures. Additionally, chemical synthesis often involves organic ligands or surfactants that can introduce surface contamination, altering the intended physicochemical characteristics of the material. Furthermore, many synthesis methods rely on hazardous reagents and solvents, raising environmental and safety concerns, particularly for large-scale production.

The goal of this work is to investigate the potential and limitations of post-deposition annealing as a way to tune the optical and morphological properties of a paradigmatic plasmonic nanocomposite, Ag/TiO_2, deposited by supersonic cluster beam synthesis (SCBD) on silica and sapphire. SCBD is a sustainable, high-throughput technique with high control over the composition of the target material. Due to the cluster-based nature of the technique, Ag/TiO_2 films deposited by SCBD exhibit very small and finely dispersed Ag nanoparticles embedded in a TiO_2 matrix, providing the perfect starting point for annealing treatments. Furthermore, since the nanoparticle deposition is ballistic in nature, films with the same properties can be deposited on different substrates, allowing a deeper understanding of film-substrate interactions. We address the role of the substrate during thermal annealing, outlining how using different substrates can steer the evolution of the film morphology and optical properties in drastically different directions. Furthermore, we show how the combination of conventional oven annealing and light-induced photothermal melting allow us to tune the size and distribution of the Ag nanoparticles inside the material over a wide range of configurations, opening new potential applications for the material.

Finally, we investigate the viability of the Ag/TiO_2 nanostructured material described so far in the fabrication of novel plasmon-based substrates for superresolution fluorescence

microscopy, plasmonic structured illumination microscopy (LPSIM). To do so, we first define an effective dielectric function for our material, using the Drude-Lorentz multioscillator model and Bruggeman's effective medium approximation. Then, we perform finite-element modeling simulations in COMSOL to ensure that the behavior of the electric field generated by the nanostructures satisfies the requirements of conventional LPSIM. Finally, we show a fabrication method for said nanostructures, which involves electron beam lithography (EBL) patterning of the desired nanostructures and SCBD deposition of the Ag/TiO_2 cluster-based nanocomposite.

To my friends and family, for their invaluable support and affection.

CONTENTS

FIGURES

ACKNOWLEDGMENTS

I would like to express my deepest gratitude to my teachers and supervisors at both Università Cattolica del Sacro Cuore, and in University of Notre Dame, Prof. Luca Gavioli, Prof. Christopher Hinkle, and Prof. Anthony Hoffmann, for their invaluable knowledge and support throughout my research. Their guidance and feedback have been instrumental in shaping this dissertation. I am also grateful to the members of my mentoring committee, for their valuable insight.

A heartfelt thank you to my colleagues and friends at Università Cattolica del Sacro Cuore and University of Notre Dame, who have provided thoughtful discussions, intellectual stimulation and new interesting points of view. Their support and sincere friendship have made this journey more rewarding.

I am also deeply indebted with my family – my parents, Francesco and Angela, and my brother Carlo Alberto, for their unconditional love and patience. Their support has been my foundation, and I am forever grateful for their sacrifices and encouragement.

Finally, I would like to thank all my friends outside academia: my friends in board game clubs, role-playing groups, theater companies and music bands, who helped me maintain balance and perspective.

CHAPTER 1:

INTRODUCTION

1.1 Overview

Plasmonic materials have emerged as a cornerstone in modern materials science, leading to tremendous advancements in a variety of fields, including spectroscopy, optoelectronics and biomedical diagnosis. The integration of plasmonic nanostructures with emerging materials, such as semiconductors and two-dimensional systems, further expands their potential, driving advancements in both fundamental research and technological innovation. In order to develop such innovative materials, it is first essential to understand the microscopic nature of plasmonic oscillations, which determine the desired light absorption and electric field enhancement properties. As we will see, these properties depend on the type of material used and its morphology at the nanoscale. Secondly, it is necessary to understand the extent to which these characteristics can be directly modified, both during the deposition of the material itself and through processing techniques. Finally, to integrate these novel plasmonic materials into practical applications, one has to outline a fabrication process based on the acquired knowledge, while also taking into account factors such as accessibility and cost efficiency.

In this work, we study the case of an important metal-oxide nanocomposite, Ag/TiO_2, whose properties are strongly influenced by the presence of plasmonic oscillations. In this

chapter, we introduce some of the concepts that will be addressed in the body of the work, providing the necessary background information and framework for this manuscript. In Chapter 2, we describe the deposition technique, which determines the starting properties of the material. In Chapter 3, we explore the substrate-dependent behaviour of the Ag/TiO_2 thin films during post-deposition thermal annealing, and the impact of this technique on the microscopic properties of the material. In Chapter 4, we exploit the photothermal heating of plasmonic nanoparticles to further affect their morphology at the nanoscale, combining this technique with conventional oven annealing. Finally, in Chapter 5, we show a promising application for our Ag/TiO_2 nanocomposite material as a substrate for a superresolution fluorescence microscopy technique.

1.2 Plasmonic materials and localized surface plasmons

Surface plasmons (SPs) are coherent and collective electron oscillations confined at the surface between a metal and a dielectric. When excited by light, the induced charge oscillation creates an electromagnetic field at the metal-dielectric interface, which can propagate along the surface (surface plasmon polariton, SPP) or be confined in the case of a small particle (localized surface plasmon polariton, LSPP). Among the most widely used materials in plasmonics, noble metals such as gold and silver are excellent candidates because of their relatively low loss in the visible and NIR range: gold is preferred for its chemical stability, while silver offers strong resonance absorption and low-cost fabrication. Other materials include metals like copper, palladium, platinum and nickel, heavily doped semiconductors and 2D materials like graphene [1–3].

Over the past decades, SPs have been extensively used to enhance the interaction strength between photons and materials in a variety of applications. In Raman spectroscopy, for example, the excitation of a surface plasmon resonance (SPR) in the substrate can lead to a drastic amplification of the Raman signals produced by the analysed samples, allowing single-molecule sensitivity and an increase in spatial resolution for the detection of small molecules, living cells and other targets [4,5]. In photocatalysis, plasmonic materials such as noble metal nanoparticles are employed to enhance light absorption, hot carrier generation and overall catalytic efficiency: in fact, such materials can harvest light in the visible and near-infrared spectrum, overcoming the intrinsic bandgap limitations of conventional semiconductors [6,7]. The light-harvesting properties of plasmonic materials are also exploited to enhance the efficiency of novel solar energy conversion devices [8]. The efficient resonant absorption of light due to the presence of SPPs or LSPPs can also result in the conversion of energy into heat through non-radiative decay processes [9]. As we will further explore in Chapter 4, photothermal heating of plasmonic nanostructures can be exploited in a variety of applications, and can even be used as a processing tool to impact the shape and size of plasmonic nanoparticles. Finally, the electric field amplification produced by plasmonic structures can increase the excitation of fluorescent molecules, leading to drastically increased performances in biosensing, medical imaging and optoelectronics [10–13]. We will further discuss about plasmon-enhanced fluorescence in Chapter 5, where we will investigate the application of plasmonic nanostructures to a super-resolution fluorescence microscopy technique. In this section, we will provide an introduction to the SPPs and LSPPs, which are a fundamental aspect to the operation of the plasmonic materials mentioned above.

To provide the fundamentals of surface plasmon polaritons, we start by modelling the interaction between an electromagnetic wave and a generic material. Since plasma oscillations

occur predominantly in materials where the electrons exhibit high mobility, such as metals, a free electron gas model is usually employed to describe the properties of plasmonic materials. Here, we prefer a more general description of the propagation medium, since our samples consist of bielement nanocomposites. If we consider that the mass of atomic nuclei is several orders of magnitude greater than the mass of electrons, we can model the electrons as driven damped harmonic oscillators, bound to nuclei by a hypothetical spring with spring constant C. The driving force is represented by an electric field, which we can write as $E = E_0 \cos(-\omega t)$ in the case of an incoming electromagnetic wave, where E_0 is the amplitude of the electric field. The damping force, proportional to velocity, represents collisions occurring during motion, occurring with a characteristic collision frequency γ (At room temperature, typical values for γ are around 100 THz). From Newton's second law, we can derive the motion equation of an electron:

$$\frac{d^2x}{dt^2} + \gamma \frac{dx}{dt} + \frac{C}{m}x = \frac{qE_0}{m}\cos(-\omega t) \tag{1.1}$$

Where m is the effective mass of the electron and q its charge. Here, we can define the natural frequency of oscillation for the electron, $\omega_0 = \sqrt{C/m}$, and write:

$$m\frac{d^2x}{dt^2} + m\gamma \frac{dx}{dt} + \omega_0^2 x = qE_0 \cos(-\omega t) \tag{1.2}$$

The solution to this equation is of the form $x = x_o \cos(-\omega t + \Phi)$, or:

$$x = x_0 e^{i\Phi} e^{-i\omega t} = \tilde{x}_0 e^{-i\omega t}; \tag{1.3}$$

where the complex amplitude $\tilde{x}_0$ incorporates the phase shift between the driving field and the oscillating electron. By plugging this solution into Equation 1.1, also converting the cosine into a complex exponential, we obtain:

$$(-i\omega)^2 \tilde{x}_0 e^{-i\omega t} + \gamma(-i\omega)\tilde{x}_0 e^{-i\omega t} + \omega_0^2 \tilde{x}_0 e^{-i\omega t} = \frac{qE_0}{m} e^{-i\omega} \tag{1.4}$$

This equation ultimately gives the expression for the amplitude of the oscillation:

$$\tilde{x}_0 = \frac{qE_0}{m} \frac{1}{\omega_0^2 - \omega^2 - i\omega\gamma} \tag{1.5}$$

The oscillating dipole moment is:

$$\tilde{p} = q\tilde{x} = \frac{q^2}{m} \frac{1}{\omega_0^2 - \omega^2 - i\omega\gamma} E; \tag{1.6}$$

From here, we can recall that the dielectric function of a material depends on the atomic dipole moment according to the relation:

$$\epsilon_r = 1 + \frac{Np}{\epsilon_0 E}; \tag{1.7}$$

where ϵ_0 is the electric permittivity of vacuum. Therefore, the dielectric function of the material is:

$$\epsilon_r(\omega) = 1 + \frac{Nq^2}{m\epsilon_0}\frac{1}{\omega_0^2 - \omega^2 - i\omega\gamma} = 1 + \frac{\omega_p^2}{\omega_0^2 - \omega^2 - i\omega\gamma} \tag{1.8}$$

Here, we have defined the plasma frequency ω_p of our material as:

$$\omega_p = \sqrt{\frac{Nq^2}{m\epsilon_0}} \tag{1.9}$$

This is the frequency a plasma will naturally oscillate at when the positive and negative charges are displaced. Equation 1.8 clearly shows that permittivity depends on the frequency of the electric field, besides the plasma frequency and damping. In other words, the material is dispersive. The damped driven harmonic oscillator is often referred to as the Lorentz oscillator model for permittivity. In the case of a metal, however, the valence electrons in metals are not anchored to their nuclei (as shown in Figure 1.1a), but are instead free to move against a fixed background of positive ion cores (Figure 1.1b). They still experience collisions, expressed by the damping term, however their restoring force (indicated by the term ω_0 in Equation 1.8) can be set to 0.

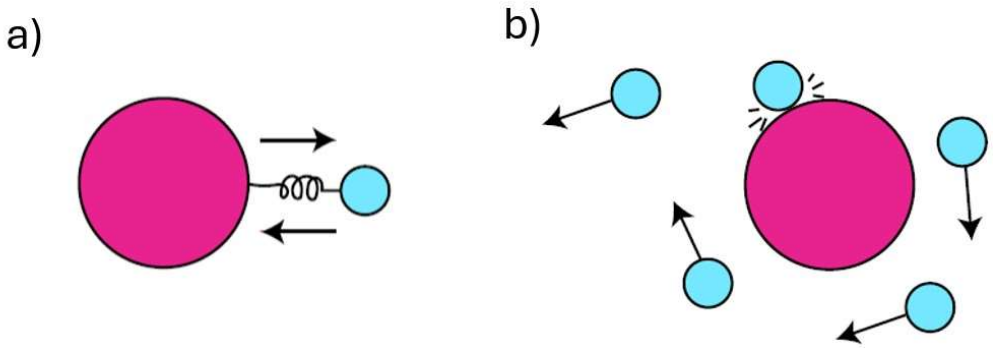

Figure 1.1: a) A scheme of the Lorentz oscillator model, where the attractive force between electrons and nuclei is represented by a hypothetical spring. b) Representation of the Drude model for a free electron gas.

The free electron gas model is usually called the Drude model and results in:

$$\epsilon_r(\omega) = 1 - \frac{\omega_p^2}{\omega^2 + i\omega\gamma} \tag{1.10}$$

The Drude and Lorentz models are often combined into a more general Drude-Lorentz multioscillator model [14,15], where the Drude component describes the intraband electron contribution to the dielectric function, while a sum of Lorentz oscillators are used to describe the interband contributions:

$$\varepsilon_r(\omega) = \varepsilon_r^{(D)}(\omega) + \varepsilon_r^{(L)}(\omega) = \varepsilon_\infty - \frac{\omega_p^2}{\omega^2 + i\omega\gamma} + \sum_{l=1}^{K} \frac{f_l \omega_p^2}{\omega_{0l}^2 - \omega^2 - i\omega\gamma_l} \tag{1.11}$$

Here, ε_∞ is the high frequency permittivity, γ is the damping term for the Drude oscillator and ω_p is the plasma frequency. In the last term, K is the number of oscillators with resonance frequency ω_{0l}^2, strength f_l and lifetime $1/\gamma_l$. Figure 1.2 shows the real (Panel a) and imaginary part (Panel b) of the permittivity of gold, which is a well-known plasmonic material, calculated using the Drude-Lorentz model, showing a good agreement with the experimental values. Note that the Drude model alone cannot accurately describe the high frequency permittivity, below the energy threshold of transitions between electronic bands.

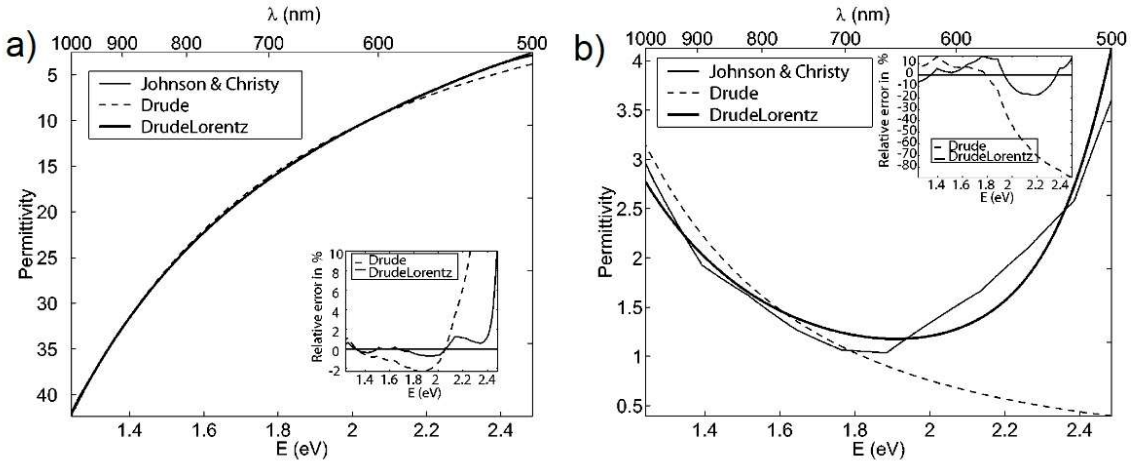

Figure 1.2: a) Real and b) imaginary part of the permittivity of gold, experimental (thin solid line) and calculated using Drude and Drude-Lorentz oscillator models.

The existence of SPPs, i.e. propagating electromagnetic modes at the interface between a metal and a dielectric, can then be inferred by solving Maxwell's equation for eigenmodes at the interface, in conjunction with the material-specific dielectric functions. At the interface, the continuity of the tangential components of the electric and magnetic fields yields a unique

solution to the wave equation characterized by a complex wavevector (Figure 1.3a). Solving the resulting dispersion relation reveals a bound mode where the local charge displacements on the surface of the metal results in an evanescent wave propagating along the interface and decaying exponentially away from it into both the metal and dielectric sides [14]. Given the properties of SPP dispersion, coupling light into SPPs is not a straightforward process, since it requires overcoming the inherent momentum mismatch between free-space photons and the evanescent plasmonic modes confined at the metal-dielectric interface. This is typically achieved through momentum matching techniques such as prism coupling (Kretschmann and Otto configurations), grating coupling, or near-field excitation [15–17]. However, if the particle supporting the oscillation is sufficiently small (i.e. smaller than the wavelength of the incident light), the collective oscillation of electrons takes the name of localized surface plasmon polariton (LSPP). Differently from SPPs, LSPPs are non-propagating excitations which arise naturally from the scattering problem of a small conductive particle in an oscillating electromagnetic field.

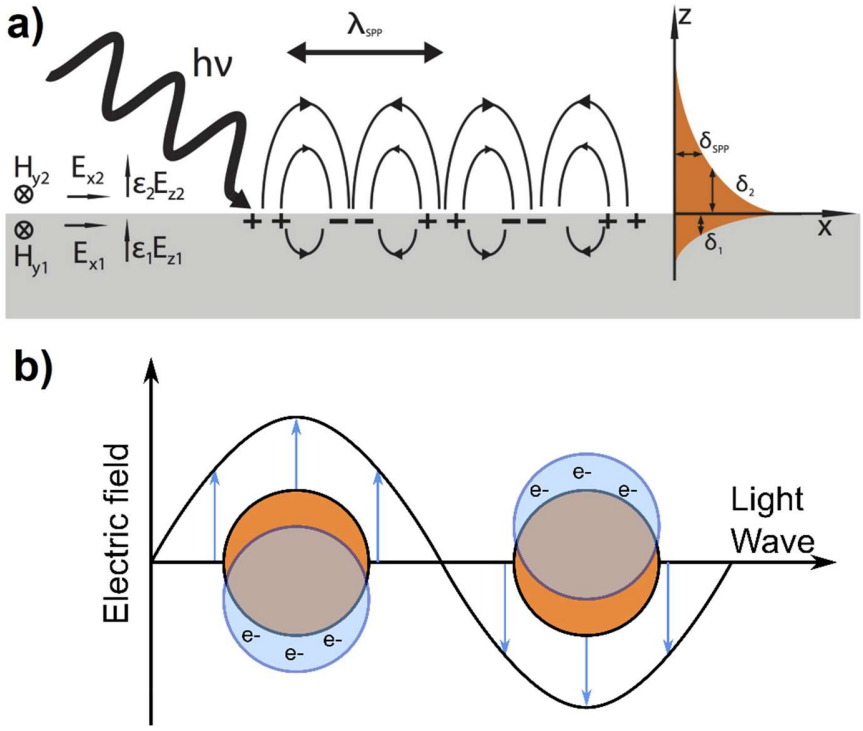

Figure 1.3: a) A representation of surface plasmons in a metal-dielectric planar interface, where the collective oscillation of electrons at the interface gives rise to evanescent waves that decay in both sides of the interface. b) A representation of localized surface plasmon oscillations, where the free electrons oscillate in response to an external electric field.

Here, the curved surface of the particle exerts an effective restoring force on the driven electrons, in a similar fashion to the Lorentz oscillator introduced earlier (Figure 1.3b). Contrary to SPP, LSPPs can be coupled to through by direct illumination with coherent light, and do not require the momentum matching techniques mentioned earlier. However, in order to maximize the coupling efficiency, a precise fabrication of the metal structures is often required.

1.3 Deposition and tuning of plasmonic nanocomposites

Aside from the material's electrical properties, the key features of plasmonic oscillations, such as the plasmon resonance frequency, strongly depend on the size, geometry and dielectric environment of the particles and structures involved in the oscillation. For this reason, in recent years, much attention has been dedicated to finding reliable ways to tailor the plasmon resonance frequency of plasmonic materials through precise control of their morphology. At the deposition stage, key parameters such as nanoparticle size, shape, and composition can be controlled by through a variety of different methods: for particles in solution, shape-controlled synthesis is achieved by using different solvents and precursors [18,19]. Additionally, nanofabrication techniques such as focused ion beam (FIB) milling, electron beam lithography (EBL), nanoimprint lithography and optical lithography have been employed to fabricate plasmonic nanostructures for use in applications like plasmon-enhanced Raman scattering and fluorescence microscopy [20]. Larger nanoparticles typically exhibit redshifted plasmonic resonances, while anisotropic geometries, such as nanorods or nanostars, can exhibit multiple resonating modes as well as enabling polarization-dependent tunability. Figure 1.4, for example, shows the dependence of the optical scattering and absorption profile of colloidal silver nanoparticle on their size and shape: Panel a shows the scattering profile of particles with different shape [21], while Panel b shows the absorption profile of gold particles with different size [22].

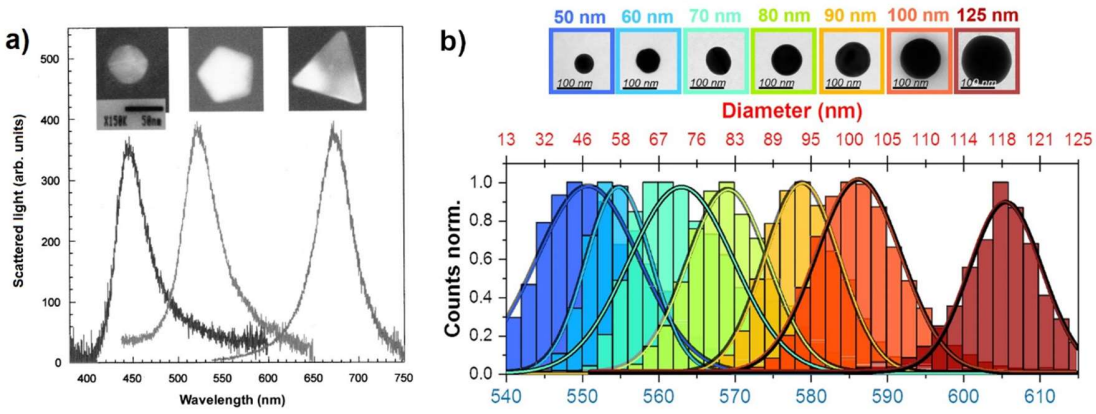

Figure 1.4: a) Optical scattering spectrum of individual silver nanoparticles, showing a TEM image of the respective particle (see Ref. 21). b) Histogram distributions of the plasmon resonance peak for gold nanoparticles of different diameter (See Ref. 22)

One of the most important aspects of plasmonic structures, however, is their integration with other materials to fully exploit their ability to concentrate light and enhance electric fields. In plasmon-assisted photocatalysis, for example, the interaction between metal particles with oxide supports can radically enhance the performance of supported-metal catalysts [23,24]. In photovoltaics devices, designs based on small plasmonic particles can be used to improve efficiency and/or extend the spectral range, allowing a considerable reduction in the thickness of solar cells [25]. Moreover, the production of thin films composed of noble metal NPs supported by a host matrix is paramount to the development of LSPR-based optical sensing platforms [26].

In recent years, significant effort has been focused on the development of self-assembled plasmonic nanocomposites, i.e. materials composed of metal nanoparticles

integrated with a polymer, semiconductor or dielectric host matrix. However, in plasmonic nanocomposites such as metal-oxide thin films, the optimization of plasmon resonance frequency is not always feasible at fabrication. For this reason, post-deposition treatments such as high-temperature annealing have been attracted lots of attention due to their ability to affect several crucial aspects during the fabrication of plasmonic materials. In fact, thermal annealing is already a widely used technique in device manufacturing: it is used, for example, to reduce stress and structural defects in thin films or silicon wafers, to activate ion-implanted dopants or to improve adhesion in multilayer systems [27–29]. In metal-oxide nanocomposites, if the melting temperature of the metal is lower than that of the surrounding dielectric matrix, the metal particles can undergo an Ostwald-like ripening process, where smaller particles merge into larger ones in order to reach a more thermodynamically stable configuration [30–33]. In turn, the change in size, morphology and distribution of the metal particles deeply affects the optical and electrical properties of the material, as we have seen in Figure 1.4, allowing the functionalization of the nanocomposites for different applications. Post-deposition thermal treatments can also be used as a tool to control the oxidation state of the elements in the film. One notable example of this technique is given by Zhang et al., where the reduction of Ag(I) to Ag(0) was obtained in Ag-TiO_2 nanocomposites by subjecting the material to thermal annealing [34]. Another promising application for annealing treatments is to impact the surface roughness of thin films as an alternative to chemical etching or electrochemical roughening. As we will further explore in Chapter 3, annealing promotes the crystallization of TiO_2 to rutile or anatase, while also increasing the surface roughness of the films. In the fabrication of TiO_2 electrodes for photocatalysis, both effects are highly desirable, since the formation of a crystalline phase increases electron mobility while a larger surface roughness increases the active surface area of the electrode [35]. Furthermore, in the case of SERS-active substrates,

surface roughening can induce an amplification in the surface enhancement factor of one to three orders of magnitude in the Raman signals [36,37].

Since thermal annealing is a scalable, accessible and cost-effective technique, it plays a fundamental role especially in the large-scale production and implementation of plasmon-based materials, such as photocatalytic devices and solar conversion platforms. However, in smaller scale applications such as plasmon-enhanced microscopy or other optoelectronic devices, thermal annealing can be used as a complementary technique, unlocking behaviours that would be otherwise unattainable through direct deposition alone.

1.4 Fluorescence microscopy and the diffraction limit

Among the various microscopy techniques, fluorescence microscopy is one of the most widely used in biology and biomedical sciences due to its ability to observe specific cellular components through molecule-specific labelling and to study the evolution of specific cellular processes inside a live sample in real time. However, despite the advancements in analysis and fabrication techniques, optical microscopes are still hampered by an ultimate limit in the optical resolution that is imposed by the diffraction of visible light wavefronts. According to Huygens' principle, wave propagation can be understood by considering each point on a wavefront as generating its own spherical wavelet, and the future position of the wavefront is formed as the sum of these secondary waves [38]. A direct outcome of this principle is that, when light is passed through apertures as in microscopy, it gives rise to diffraction patterns on the imaging plane. For a circular aperture, the diffraction pattern takes the shape of an Airy disk, characterized by a brighter region in the center together with a series of concentric rings of decreasing intensity around it, as shown in Figure 1.5.

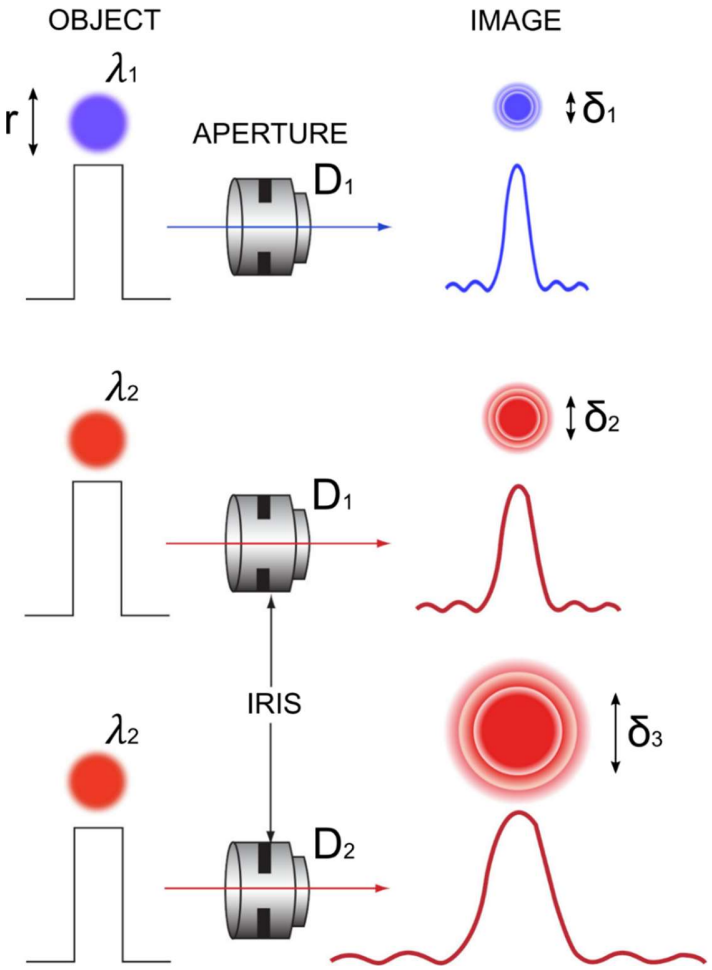

Figure 1.5: Airy disks produced by the same object with different wavelengths (λ_1 and λ_2) and different lens apertures (D_1 and D_2)

The angular diameter of the central peak of the Airy pattern depends on the wavelength λ of the illuminating light and the diameter D of the aperture, according to the formula:

$$\delta_s = \frac{1.22\,\lambda}{D} \tag{1.12}$$

Determining the size of the diffraction pattern also allows to define a resolution for a microscope system via the Rayleigh criterion. In fact, if we define the resolution as the minimum separation between two objects that can be resolved, we can deduce that the Airy disc peaks corresponding to the objects must also be distinguishable from each other. According to the Rayleigh criterion, this happens if the maximum of the Airy disk of one object is lined up with the first minimum of the diffraction pattern of the other. For a lens aperture, this happens when:

$$r = \frac{0.61\lambda}{NA} \tag{1.13}$$

Here, NA is the numerical aperture of the system, defined as:

$$NA = n \sin\alpha\,; \tag{1.14}$$

where n is the index of refraction and α is half of the angular aperture of the lens or microscope objective used, also defined as:

$$\alpha = 2\arctan\left(\frac{D/2}{f}\right); \tag{1.15}$$

where f is the focal length of the lens and D its diameter.

The Rayleigh criterion is represented conceptually in Figure 1.6 for two point-like objects. A system is said to be diffraction-limited or unresolved (leftmost image) if the main diffraction peaks of the objects are within the range defined by the Rayleigh criterion.

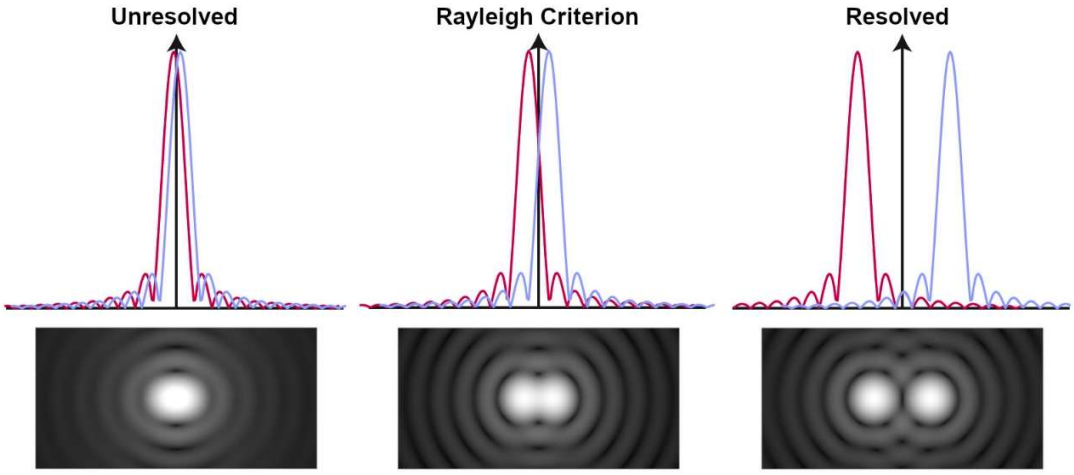

Figure 1.6: Graphical representation of the Rayleigh principle for two point-like objects: in the center image, the main diffraction peak of one object corresponds to the first minimum of the diffraction pattern of the other. The leftmost image represents an unresolved system, where the distance between the main diffraction peaks is lower than the limit set by the Rayleigh criterion. The rightmost image shows a resolved image, where the two diffraction patterns are sufficiently spaced.

For a typical optical microscopy setup (λ=550 nm, NA=1.2), the smallest structures that can be resolved are on the order of half the wavelength of the light used, or typically around 250 nm, which is comparable to or larger than many subcellular features. This resolution limit can be improved by using shorter wavelengths, as shown in Figure 1.5;

however the higher photon energy can easily lead to photodamage in the case of biological imaging [39].

To visualize smaller cellular features, researchers have relied on electron microscopy (EM), which offers a high resolution due to the short De Broglie wavelength of electrons [40]. However, when it comes to biological research, EM has several limitations, requiring samples to be fixed, dehydrated and thinly sectioned in vacuum to avoid electron interactions with air and the samples themselves. These preparations can introduce artifacts and prevent live-cell imaging. As a result, there's a strong need for a microscopy method that combines the high resolution of EM with the non-destructive and live-cell imaging capabilities of optical microscopy. In recent years, numerous techniques, commonly referred to as super-resolution microscopy, have been developed to surpass the diffraction limit while still relying on optical microscopy. Stimulated-emission depletion microscopy (STED) was the first concrete method to break the diffraction limit [41]. Since then, many other techniques have been developed for nano-imaging of fluorescent samples, such as photo-activated localization microscopy (PALM) [42,43], stochastic optical reconstruction microscopy (STORM) [44] and structured illumination microscopy (SIM) [45]. We will further discuss the peculiarities and differences between the different super-resolution techniques in the introduction to Chapter 5. For now, we will focus on SIM, since it will be the focus of the final part of this work.

1.5 Structured illumination microscopy and Blind-SIM

Compared to other super-resolution techniques, SIM is of special interest for biological applications because of its compatibility with a wide array of fluorophores and its

capability for high imaging speeds, which are needed for the observation of cellular processes. In this technique, the sample is illuminated with a spatially structured excitation light, which makes high-resolution features visible in the observed image in the form of moiré fringes. In microscopy, any observed image can be thought of as the multiplication of an object pattern and an illumination pattern, convolved with the point spread function (PSF) of the optical system employed, which represents the intensity distribution of light in the image plane resulting from observing a single point object (delta function) in the object plane. In the case of SIM, the object pattern is the spatial distribution of the fluorescent dye, which is unknown, while the illumination pattern is the structured excitation light intensity, usually a known sinusoidal or grid-like pattern. When these two fine patterns are multiplied, a beat pattern will appear (moiré fringes), which encode sub-wavelength information about the object. Figure 1.7 shows an example of the working principle of structured illumination microscopy by using a sinusoidal illumination pattern. By acquiring multiple images of the object under varying pattern orientation and phases, one can reconstruct the super-resolution image of the sample by feeding the set of diffraction-limited sub-images to an image reconstruction algorithm [48].

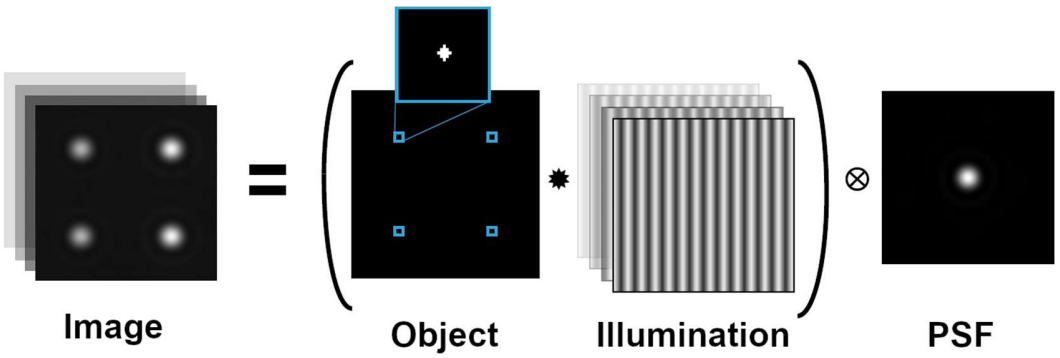

Figure 1.7: A simulated representation of Equation 1.16, where a set of diffraction-limited images (to the left) is obtained by multiplying the object image (i.e. the spatial distribution of the fluorophores in the sample) with a set of illumination patterns with different phases. The result is then convolved with the PSF of the optical system.

As an example, let's suppose we want to reconstruct an object pattern o(x,y) through the acquisition of a set of diffraction-limited images. According to what we have learned so far, the equation for a recorded image will be of the form:

$$m_l(x,y) = [o(x,y)I_l(x,y)] \otimes p(x,y); \tag{1.16}$$

where $m_l(x,y)$ is the l -th acquired image, I_l is the l -th illumination pattern, and p is the PSF of the optical system. Let's take a sinusoidal pattern in the x-direction as our illumination pattern:

$$I_l(x,y) = 1 + \cos(2\pi x k_{ill} + \Phi_l)\,; \tag{1.17}$$

where k_{ill} represents the spatial frequency of the illumination pattern and Φ_l the phase of the l-th illumination pattern. Substituting this into Equation 1.16, we can write the Fourier transform of the acquired images:

$$M_l(k_x, k_y) = \left[O(k_x, k_y) + \frac{1}{2}O(k_x + k_{ill}, k_y)e^{-i\Phi_l} + \frac{1}{2}O(k_x - k_{ill}, k_y)e^{-i\Phi_l}\right]P(k_x, k_y) \quad (1.18)$$

As we can see in the equation, the spatial frequency of the object is shifted by the frequency of the illumination pattern k_{ill}. To retrieve the super-resolution real space image, one must solve Equation 1.18 for every different illumination pattern, separating the sub-image frequency information from the shifted high-frequency information. Then, the final image can be retrieved via inverse Fourier transform. This approach can be implemented with an arbitrary number of desired illumination patterns, providing that one has control over their phase and orientation. As we can infer from Equations 1.17 and 1.18, the final increase in resolution depends on the frequency of the illumination pattern k_{ill}. For this reason, there is a strong push towards researching novel substrates that are able to support illumination patterns with a high k_{ill}. In this perspective, substrates that support plasmonic oscillations (either SPPs or LSPPs) are excellent candidates, giving rise to plasmonic structured illumination microscopy and localized plasmonic illumination microscopy (PSIM and LPSIM, respectively). Compared to SPPs, LSPPs have an additional advantage when it comes to generating illumination patterns for SIM: in fact, in small metal structures, the electromagnetic modes are discretized, which means that an efficient coupling is achieved by matching the momentum of the incident wave to the momentum associated with the LSPR frequency, or

vice versa. For this reason, having access to a material with a tuneable LSPR frequency represents an invaluable tool to optimise the illumination pattern for specific fluorescent dyes or molecules. An experimental demonstration of this localized plasmonic structured illumination microscopy (LPSIM) has been given by Ponsetto et al., showing a potential 3x improvement in the imaging of subcellular features compared to the diffraction-limited case [46].

Another interesting aspect of SIM is that the image reconstruction can also be performed without knowing the illumination patterns, by using an algorithm called Blind-SIM [47]. This technique dramatically simplifies the experimental set-up and allows the use of a wider variety of nanostructures as platforms for structured illumination microscopy. The principle of Blind-SIM is similar to that of conventional SIM, except that it not only seeks to reconstruct the original image, but also the incident illumination patterns. Referring to Equations 1.16, this means that the system has L+1 unknowns: the object image $o(x, y)$ and the l illumination patterns $I_l(x, y)$. In this state, the system is highly undetermined. To avoid this, we introduce a constraint on the illumination patterns, requiring that the sum of all intensities be roughly homogeneous over the sample plane, or:

$$\sum_{l=1}^{L} I_l \approx L I_0 \,; \tag{1.19}$$

where I_0 is constant over the sample plane. The last intensity can then be written as:

$$I_L(x,y) = LI_0 - \sum_{l=1}^{L-1} I_l\,(x,y) \tag{1.20}$$

By combining this expression with Equation 1.16, we obtain a formula for the L -th image:

$$m_L(x,y) = \left[\left(LI_0 - \sum_{l=1}^{L-1} I_l\,(x,y)\right) o(x,y)\right] \otimes p(x,y) \tag{1.21}$$

Here, note how I_L is now absent, outlining how the constraint introduced in Equation 1.19 can be effectively used to reduce the number of unknowns. By iterating this approach, the object image and the first $L-1$ illumination patterns are jointly estimated so as to minimize the cost functional:

$$F\left(o, I_{1,\dots,L-1}\right) = \sum_{l=1}^{L-1} \|m_l - (I_l o) \otimes p\|^2 + \left\| m_l - \left[\left(LI_0 - \sum_{l=1}^{L-1} I_l\right) o\right] \otimes p \right\|^2 ; \tag{1.22}$$

where $\|\cdot\|$ is a Euclidian norm over the image space. A conjugate gradient algorithm is then used to modify the estimates of $o(x,y)$ and $I_{1,\dots,L-1}$ to minimize F.

A graphic representation of the Blind-SIM algorithm is represented in Figure 1.8 for a simulated object pattern and a set of L random speckle patterns, outlining how the reconstruction algorithm is able to simultaneously estimate object image and the random illumination patterns. As we will see in Chapter 5, Bind-SIM has been validated experimentally by using a variety of different substrates as a source for the random speckle illumination

patterns, including small beads [47], silver nanodiscs [46] and self-assembled gold nanoparticles [48]. In Chapter 5 of this work, we will explore the viability of cluster-based Ag/TiO_2 nanostructured thin films as a substrate for SIM.

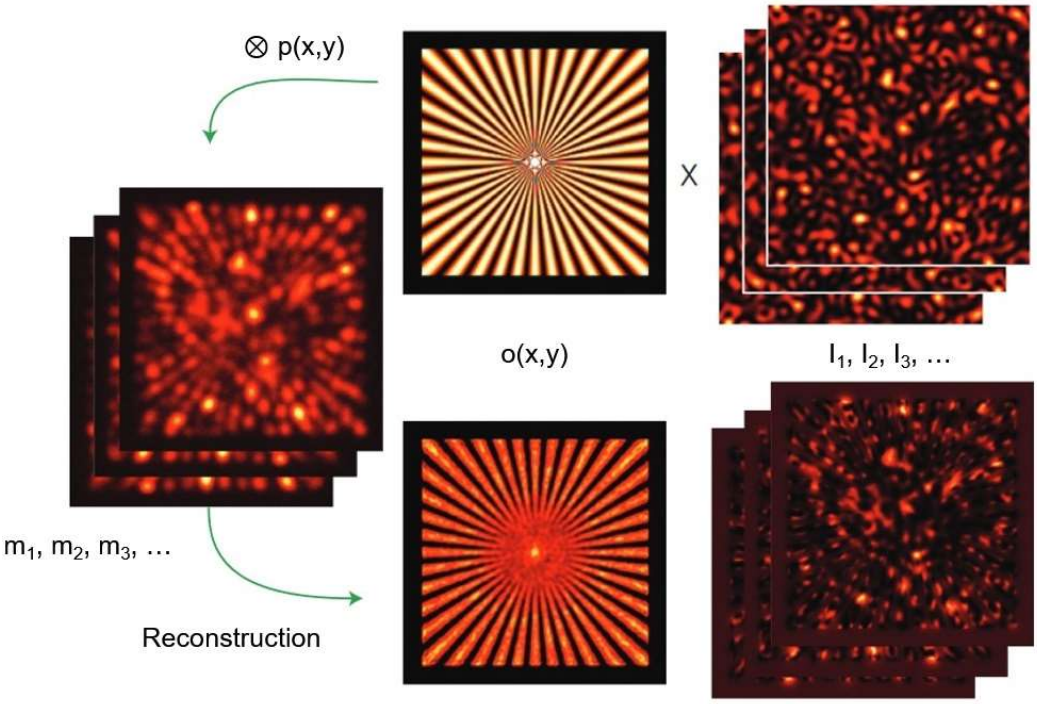

Figure 1.8: Illustration of the different steps of a Blind-SIM experiment: the different illumination patterns I_1, I_2, I_3, … are multiplied by the object pattern and convolved by the microscope PSF to provide a set of diffraction-limited images. The algorithm then simultaneously reconstructs the object pattern and the illumination patterns.

CHAPTER 2:

MATHERIALS AND METHODS

2.1 Fabrication and Processing Techniques

In this chapter we will provide detailed information on the tools, materials and techniques used to fabricate, process and characterize our samples.

Ag/TiO_2 samples described in Chapters 3, 4 and 5 were deposited in Università Cattolica del Sacro Cuore, Brescia, using a custom-built supersonic cluster beam source, which will be described in better detail in Section 2.3. The SCBD apparatus is provided with a quartz microbalance, which is used to measure the final thickness of the sample. As more and more mass is deposited on the quartz oscillator, its oscillation frequency decreases. The final thickness of the material was obtained in every deposition via the following steps: first, a test sample is deposited on a Si wafer placed directly on the side of the quartz microbalance; then, the thickness of the test sample is then measured via AFM by performing a scratch on the sample itself or by using a simple tin foil mask, to obtain the relation (in Hz/nm) between the drop in oscillation frequency of the quartz microbalance and the corresponding deposited thickness. This proportionality factor depends on the nature of the target material and, to a lesser extent, on the deposition parameters such as the gas pressures. The final samples are then deposited by calculating the expected drop in Hz for a sample of the desired frequency.

In Chapter 5, the Ag layer was deposited at Notre Dame Nanofabrication Facility using an AIRCO TEMESCAL FC-1800 e-beam evaporator with an in-build thickness monitor. The lithography was achieved using a Raith EBPG5200 electron beam lithography system with a

100kV accelerating voltage and a beam size of 36 nm during the fabrication of the nanridges and of 50 nm for the nanocylinders.

The oven annealing described in Chapters 3 and 4 were performed using a Zeta Magnum Colac FQ5005 oven, with a power of 0.9 kW and a maximum heating temperature of 1100°C. For samples annealed at temperatures up to 500°C, the samples were inserted directly into the oven and annealed for 1 hour at the setpoint. For annealing temperatures higher than 500°C, the sample was inserted at 500°C, then the temperature was ramped up to the desired temperature and kept at setpoint for 1 h. The heating ramp was about 40°C/min. In all cases, no ramp down was used and the samples were extracted immediately after the annealing process and let to cool at room temperature. For characterization, we used different samples for each defined temperature.

During the annealing process, the samples were placed on alumina slabs in order to minimize heating by contact with the oven surface. The white light exposure described in Chapter 4 was achieved via a 175W Xenon lamp, placed orthogonally at a distance of 30 cm from the samples.

2.2 Characterization Techniques

All AFM measurements performed on the samples were acquired using a Park NX10 AFM system in tapping mode. A PPP-XYNCSTR-50 cantilever with 10 nm nominal tip radius and a typical resonating frequency of 160 kHz was employed. When analyzing sparse particles (See for example Figure 3.2), particles were deposited on a polished Si wafer with an estimated RMS roughness of ~0.5 nm. All AFM images were analyzed via the software Gwyddion. For

sparse particle analysis, after applying a background leveling algorithm, we removed particles with a diameter smaller than 4σ, where σ is the standard deviation of the background height.

To determine the GSD, we applied a watershed algorithm to deduce the grain size. The film transmittance and reflectance were obtained in the UV-Vis-NIR range (2002500 nm) with a Perkin-Elmer Lambda 950 spectrophotometer (Perkin Elmer Inc., Waltham, MA, USA) equipped with a 150 mm integrating sphere. The Raman spectra were acquired on a Renishaw inVia microscope equipped with a 633 nm laser (Renishaw RL633, maximum nominal power of 10 mW). A 50× objective and a laser beam intensity of 1% were used.

The film composition was evaluated by X-ray photoelectron spectroscopy (XPS) at the end of the annealing cycle using a dual anode (Mg-Al) X-Ray source and a Phoibos 100 SPECS analyser. The samples were introduced directly after deposition in the XPS system without any further treatment. The incident photon energy was 1253.6 eV. The corresponding photoelectron sampling depth for the elements composing the film is up to 5 nm. A field emission scanning electron microscopy (SEM) apparatus (FESEM, JEOL JSM 7100F TTLS) operating at a base pressure of $<1 \times 10-4$ Pa and equipped with secondary and backscattered electron detectors was used for imaging of the film. The spatial distribution and the relative concentration of Ag and Ti were evaluated by energy dispersive X-ray spectroscopy (EDX) (spectrometer: Oxford X-Max 80) installed on the same microscope. Prior to the SEM/EDX analysis, the samples were coated with a 6 nm thick carbon film to avoid charging.

2.3 Supersonic Cluster Beam Deposition

In the previous chapter, we have mentioned how post-processing techniques such as thermal annealing are becoming an important part in the manufacturing of plasmonic nanocomposites, allowing to control different crucial aspects of the selected material, such as the nanoscale morphology, crystallinity and roughness. However, to unlock the full potential of post-deposition tuning, it is necessary to start from a deposition technique which is accessible and offers a high deposition rate. This is especially true for large-scale production of plasmonic nanocomposites. In this perspective, cluster-based synthesis has attracted a lot of attention and has brought considerable advancements in the production of plasmonic nanocomposite films [4,50–52]. Clusters are defined as aggregates ranging from a few atoms to a few thousands of atoms, where the structure and chemical composition is well-defined and dependent on the type of process used for deposition. In this work, we used supersonic cluster beam deposition (SCBD) to fabricate plasmonic metal-oxide thin films made of Ag and TiO_2.

Figure 2.1 shows the schematic of the SCBD process: the clusters are formed using a pulsed microplasma cluster source (PMCS), where ablation of the target material is achieved via a pulsed gas discharge and the vaporized metal atoms undergo a rapid nucleation phase. The mixture of carrier gas (usually helium) and nanoclusters undergoes a free expansion into the deposition chamber, where the larger clusters are filtered by a set of aerodynamic lenses. Here, a skimmer is used to select the central part of the beam. In the deposition chamber, the carrier gas is removed via differential pumping, and the clusters are ballistically deposited onto the chosen substrate.

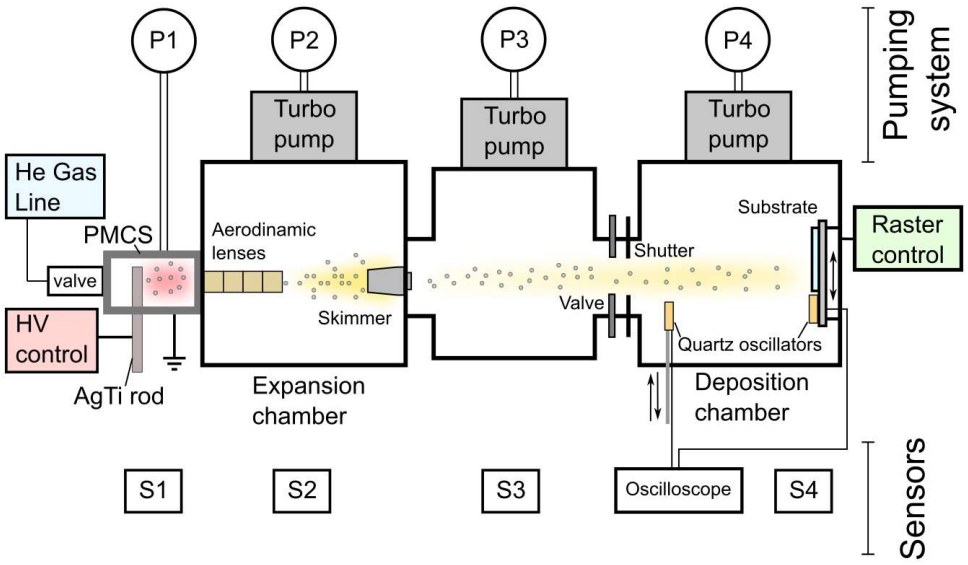

Figure 2.1: Scheme of the SCBD apparatus.

PMCS-SCBD is a physical, bottom-up approach to thin film synthesis, where the fundamental structure of the building blocks (i.e. the clusters) is maintained during deposition. This characteristic of SCBD is extremely important, since it allows to deposit the same substrate on different materials. As we will see in Chapter 3, this allows a deeper understanding of the film-substrate interactions during post-deposition annealing treatments, which is crucial to achieve tuneability in metal-oxide nanocomposites. Furthermore, since the aerodynamic lenses can be used to filter the size of the clusters during the expansion, the deposition of clusters with a precisely controlled size distribution is allowed. In particular, the size of the nanoscale components of the films (i.e. nanoparticles or nanoclusters) should be minimized to allow a larger number of possible outcomes during annealing. In the case of metal-oxide nanocomposites, for example, we have mentioned how the morphological evolution of the

metal nanoparticles mainly happens through an Ostwald-like ripening, meaning that the initial size distribution should be as small as possible in order to provide true tuneability over the nanoparticle size. Finally, the chemical composition and structure of the clusters can be easily modified by changing the target material, providing additional control over the final result.

Regarding the deposition of the Ag/TiO_2 samples described in Chapters 3, 4 and 5, the target material was an Ag-Ti rod (ACI Alloys, San Josè, CA, USA) with a mass abundance of 50% Ag and 50% Ti. After deposition, the films were exposed to air to obtain titanium oxidation to TiO_2. The oxidation of TiO_2 was confirmed via XPS analysis performed on the samples after deposition (See Supplementary Information of [49]). He gas at a pressure of 50 bar was used as a carrier. The gas was injected into the PMCS through a needle valve, opening for 322 μs at a frequency of 3 Hz. The discharge was triggered after every gas injection, with a delay of 0.75 ms and a pulse duration of 120 μs. The applied voltage between the cathode (rod) and anode (located inside the PMCS) was 800 V. The base pressure of the PMCS was $\sim 10^{-3}$mbar, while the pressure of the deposition chamber was $\sim 10^{-6}$mbar.

CHAPTER 3:

EFFECT OF SUBSTRATE ON THE THERMAL EVOLUTION OF AGTIO$_2$ NANOMATERIALS

3.1 Background and motivation

The functionalities of metal/oxide thin films depend on the physical properties of the constituents and on the microscopic interactions at the film/substrate interface. Several factors such as the morphology, composition, crystalline phase and porosity of the materials may be controlled at deposition by using synthesis methods such as cold gas dynamic spray [53], jet printing [54], supersonic cluster beam deposition (SCBD) [52,55], sol-gel methods [56,57], magnetron sputtering [58–60] and dip-coating [61]. After deposition, annealing treatments such as oven and laser annealing can further tweak the properties of a large variety of thin films, able to impact both microscopic (surface morphology, crystallinity) and macroscopic (conductivity, absorption profile) properties [57,58,60,62,63]. Being able to functionalize these properties after deposition is a major advantage in terms of efficiency, because one can optimize the deposition process and the properties functionalization separately, leading to a dramatic increase in deposition rates and to a more streamlined fabrication process. This is especially true for self-assembled structures, where little or no lithography steps are involved and where the final morphology of the film is only determined

by the deposition parameters and by the chemical and thermodynamical transformations induced by post-deposition processing. In recent years, much research has been devoted to understanding the potential of post-deposition annealing. Most of the times, however, film-substrate interactions during annealing are neglected or ignored. This is probably due to the fact that, to properly identify the substrate influence on the film behaviour as a function of temperature, one should be able to deposit the same film independently on the support type. Such opportunity is provided by spray synthesis techniques such as SCBD, where the film building blocks are maintained during landing and the film morphology at the nanoscale is determined only by the NP assembly [50,64–66].

In this chapter, we will investigate the temperature-induced transformation of a paradigmatic model constituted by a nanostructured film composed of metal and oxide nanoparticles (NPs). In fact, Metal/titanium dioxide (TiO_2) nanostructures have unique properties for applications in photocatalysis [67–70], antibacterial coatings [51,66], sensors [71–74], solar cells [75,76], and energy storage [77]. The addition of NPs of different materials to a host matrix of TiO_2 usually results in an increase of the stable temperature range of the composite film, due to the pinning force introduced by the NPs that hampers the coalescence and crystallization [78,79]. For example, the addition of small silica and alumina particles in TiO_2 allows for a stabilization of the anatase phase up to 800°C [80]. In this perspective, SCBD, which allows the deposition of clusters composed of both the host material and the pinning particles [51], is a promising technique for the deposition of multielement heat-resistant thin films.

Temperature may also lead to structural modifications and variation of the optical response of the system. Ag/TiO_2 nanocomposites exhibit an optical absorption band around 400-500 nm, which is usually associated to the plasmonic nature of nanometer-sized Ag

particles [81–84]. After annealing, Ag interdiffusion and the NPs coalescence inside the film results in the formation of larger Ag clusters on the film surface [30,32,58,81,85]. The wavelength and shape of the absorption feature can then be drastically modified by heat treatments: for example, in Ag-TiO_2 coatings prepared by atom beam sputtering, annealing at 600°C causes a redshift and a width increase of the absorption band [30]. Modification of the Ag morphology and distribution within the film would hence affect also the multicolour photochromism [86,87], the surface-enhanced Raman scattering [88,89] and the antimicrobial activity of such systems [66]. Since the amount, dimension and distribution of Ag NPs determine the optical properties of the films [34,90,91], understanding the mechanics of Ag segregation and clustering is a necessary step towards the synthesis of new materials with specific absorption and transmission bands. This is especially important for applications in photocatalysis: for example, the inclusion of Ag NPs can be used to extend the photoresponse of TiO_2 to the visible range of the spectrum.

In the study of the temperature dependent morphological changes of Ag/TiO_2 nanostructured materials, however, the role of the substrate was only considered in a single case, where a large decrease in optical absorption in the 400 – 500 nm wavelength range after an annealing at 450 °C was attributed to the diffusion of Ag atoms into the substrate [92]. This indicates a lack of a deep understanding of the substrate role for this type of nanocomposites, that would be of paramount importance to fully understand the formation of tailor-sized Ag clusters in the development and engineering of applications. This open issue asks for a synthesis technique of nanogranular systems allowing the deposition of films with the same properties independently of the substrate characteristics. SCBD presents several advantages in terms of deposition rate, control over the film thickness and roughness and mass selection of the particles by aerodynamic effects, which allow to fabricate nanostructured system with the

desired structural properties in an effective way [50,93–95]. Furthermore, SCBD allows for the simultaneous deposition of both metal and oxide NPs, maintaining the nanostructured nature of the building blocks, the $AgTiO_2$ NPs. Since the films deposited by SCBD are the same independently of the substrate on which they are deposited, this technique is suitable to investigate the role of the substrate on the evolution of the films during thermal annealing.

In this chapter, we will discuss the case of a paradigmatic metal-oxide thin film, Ag/TiO_2, and study the temperature-induced transformation of its optical and morphological properties on two different substrates. In Section 2, we will focus on the surface morphology of Ag/TiO_2 thin films deposited by SCBD, and study the impact of post-deposition annealing on the grain structure and roughness of the films. In Section 3, we will focus on the optical properties of the films, and specifically on the plasmonic absorption properties related to the presence of Ag nanoparticles embedded in a dielectric matrix. In Section 4, we will discuss the effect of substrate on silver diffusion and make some hypotheses to explain the experimental outcomes. Finally, in Section 5, we will address the impact of silver inclusions on the phase transition of TiO_2 nanocrystals.

3.2 Surface morphology of $AgTiO_2$ nanocomposites

The morphological properties of the Ag/TiO_2 films were investigated at room temperature by AFM on the as-deposited films and after every annealing step on film deposited on both silica and sapphire. Films deposited by SCBD are unaffected by the substrate at deposition, since their structure is only determined by the properties of the Ag/TiO_2 NPs and their aggregation on the substrate. In particular, the landing energy per

atom allows for the conservation of the NPs integrity [50,96–98]. It is worth recalling that the NPs forming the nanogranular film are constituted by Ag nanocrystals partially embedded into an amorphous TiO_2 matrix, as reported in details elsewhere [51,52].

Figure 3.1a shows a high-angle annular dark field scanning transmission electron microscopy (HAADF-STEM) image of sparse Ag-TiO_2 nanoclusters produced with SCBD: the clusters show a Janus-like profile, where both Ag and Ti components are present at the nanoscale. As shown in Figure 3.1b, the size distribution of the Ag nanoparticles is bimodal, where the modes have an average size of 1.2 nm and 2 nm, respectively [52].

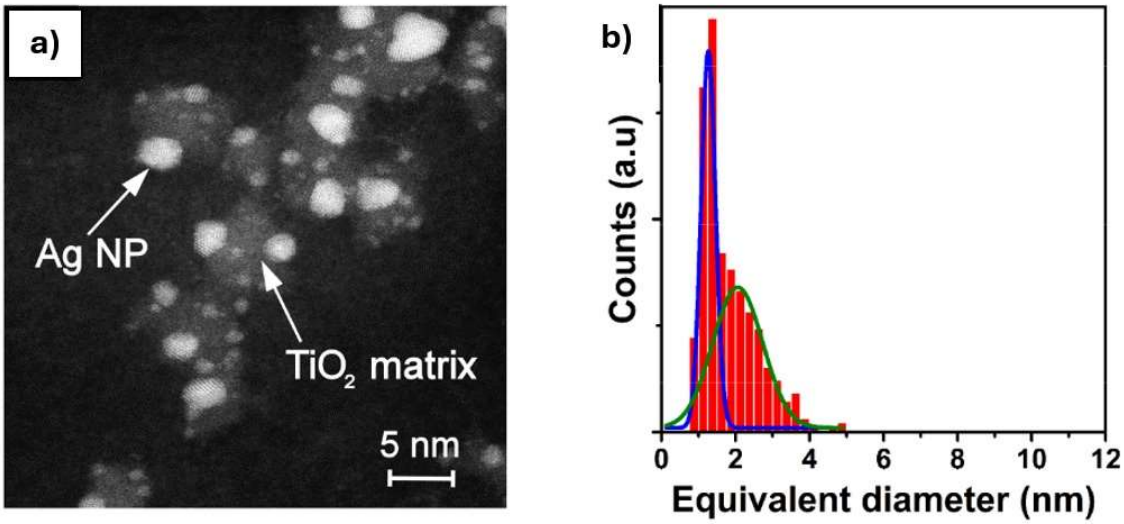

Figure 3.1: a) HAADF-STEM of low coverage Ag/Ti 50-50 NP film on the same type of substrate; b) Ag NP size distribution as extracted from a collection of 70 40x40 nm^2 wide frames, only sizes of Ag NPs embedded in oxide matrix are considered.

The average dimension of the $AgTiO_2$ nanoclusters was further investigated by AFM profiling of a sparse sample of nanoclusters on a Si wafer (Figure 3.2a). After background levelling, the max z height of each particle compared to the Si background, obtained by AFM data, has been used to trace a size distribution histogram of the Ag-TiO_2 clusters, shown in Figure 3.2b. The size distribution is trimodal, with most of the particles having a radius of 2.81 nm. Since TiO_2 has a lower density than Ag, this result is compatible with the nature of the Ag-TiO_2 clusters.

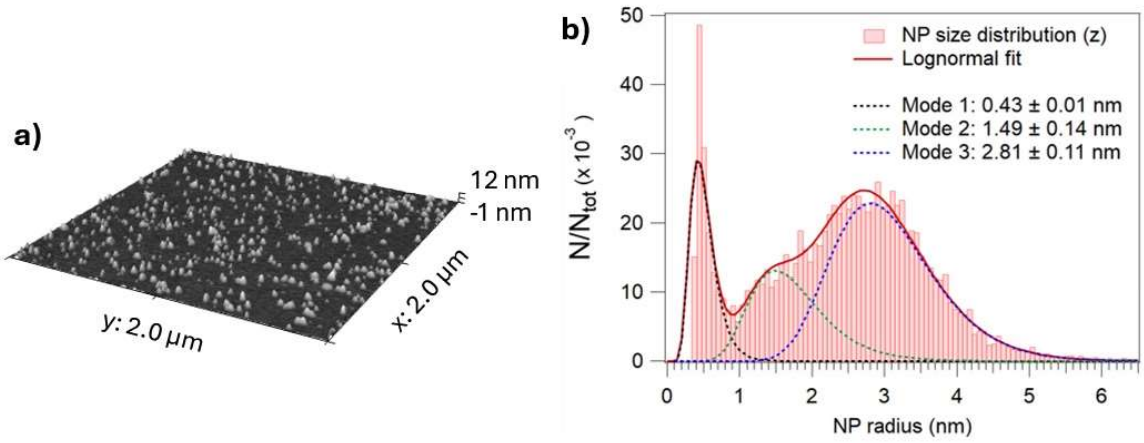

Figure 3.2: a) AFM image of sparse Ag-TiO_2 nanoclusters on a Si wafer; b) Z size distribution (radius) of the Ag-TiO_2 nanoclusters as investigated by AFM data: the distribution is trimodal. The lognormal functions used in the fit are commonly used to describe the size distribution of particles generated by Ostwald ripening, which is comparable to the cluster formation mechanism inside the PMCS.

To study the effect of annealing on thin films, we deposited a 50 nm film of Ag-TiO_2 (50-50) on single crystal (0001) α-Al_2O_3 single-crystal and amorphous fused silica substrates. Silica and sapphire were chosen due to their chemical and thermal stability at high

temperatures and constant dielectric constant in the Vis-IR range. The target material was a 99.99% purity Ag/Ti rod with a nominal 50–50 Ag-Ti wt.%. The nominal thickness and deposition rate of the films were monitored using a quartz microbalance, while the actual film thickness, measured on an edge using atomic force microscopy (AFM), is 50 ± 2 nm. Annealing steps of 1 h were performed in an oven at standard atmosphere and pressure at temperatures of 200°C to 900°C, with a step of 100°C. After annealing, the samples were characterized using via UV-VIS spectrophotometry, AFM, x-ray photoelectron spectroscopy (XPS) and Raman spectroscopy.

Figure 3.3 shows the evolution of the surface morphology of the two films obtained by AFM. The as-deposited films exhibit a granular and homogeneous morphology which is typical of cluster-based thin films [50–52]. For annealing temperatures up to 500°C, no significant change in the surface structure or grain size is observed. Above 500°C, the formation of new island-like structures on the surface are visible on the sample deposited on sapphire. The size of these structures increases gradually with subsequent annealing steps, reaching a mean width of 570 ± 12 nm at 900°C, with a mean height of 360 ± 8 nm. The presence of such islands is compatible with the migration and clustering of Ag [32]. On the sample deposited on silica, however, no such structures can be observed at any stage of the annealing process. In addition to the migration and surfacing of Ag, the annealing of the films for temperatures higher than 600°C also results in a noticeable coarsening of the Ag/TiO_2 grains on both substrates. Moreover, on the sapphire deposited film one observes the formation of 50 ± 1 nm deep pits, thus reaching the substrate.

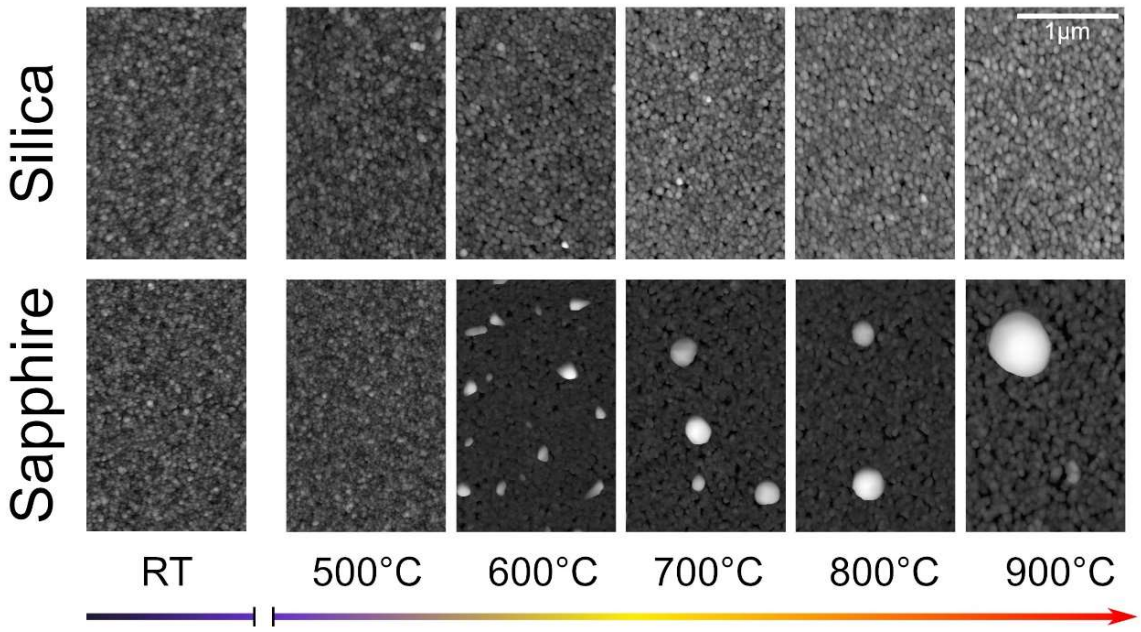

Figure 3.3: AFM images of the Ag/TiO_2 (Ag/Ti 50–50) films on silica (top) and sapphire (bottom) as a function of the different annealing steps.

To quantify the grain coarsening effect, we extracted the normalized grain size distribution (GSD) from AFM data, shown in Figure 3.4a, for the silica-deposited film as a function of the annealing temperature. For each GSD, we used three different AFM images of the same sample in different spots, with a total of 1200 – 1500 grains per distribution. Here, "grains" does not indicate the crystal domains, since the TiO_2 is amorphous; rather, it indicates cluster aggregates which are formed during deposition. The grain size was measured from the grain projected surface area, a value that is influenced by tip-sample convolution effects. The GSD follows a lognormal shape typical of films deposited by SCBD [50]. The evolution of the mode and standard deviation of the GSD patterns are shown in Figure 3.4b, while the root mean square roughness (RMS) of the surface is given in Figure 3.4c. For temperatures up to

500°C, the GSD maintains the lognormal shape with the most recurring grain radius being 20 ± 1 nm, indicating that the film is nearly unaffected by the annealing process, as expected from our earlier analysis of the surface. This behaviour is different from pure TiO_2 NPs films, where grain coarsening is taking place for temperatures as low as 300°C [35,99–101].

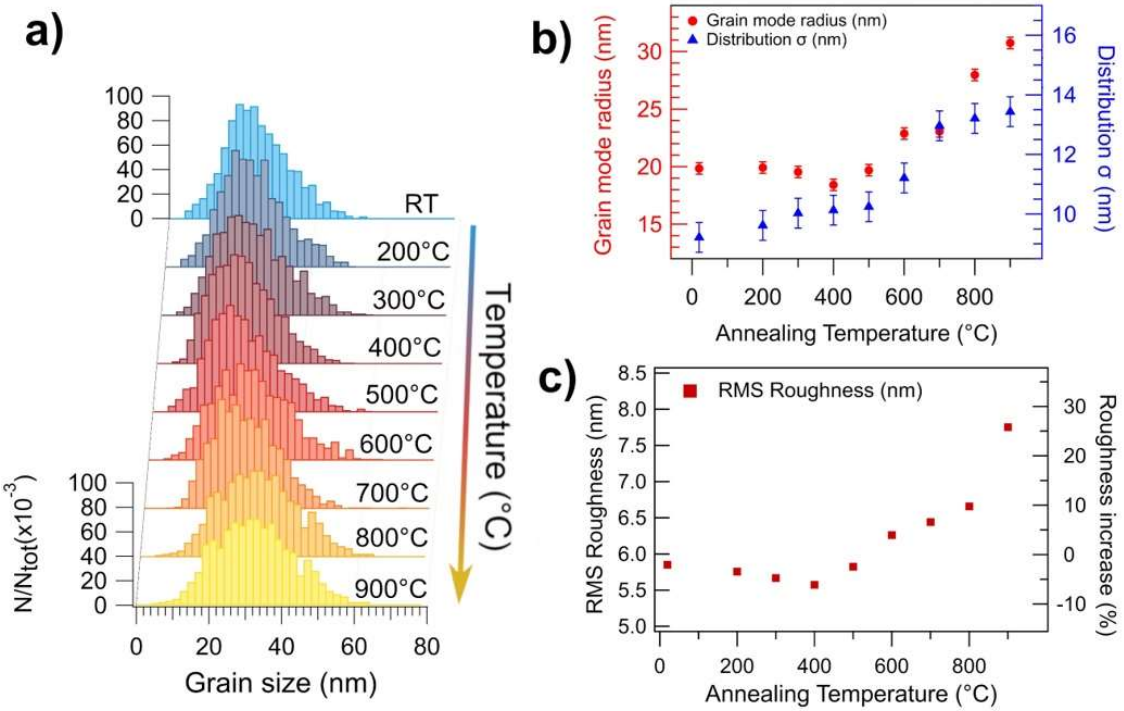

Figure 3.4: a) Evolution of the GSD of the Ag/TiO_2 (Ag/Ti 50-50) film on silica as a function of the annealing temperature. b) Evolution of the mode (red dots, left axis) and standard deviation (blue dots, right axis) of the GSD as a function of the annealing temperature. c) RMS roughness of the Ag/TiO_2 (Ag/Ti 50-50) film on silica as a function of the annealing temperature. The percentage increase in RMS roughness, compared to the as-deposited film, is reported on the right axis referring to the same data.

The thermal stability of the grains in the present Ag-TiO_2 nanocomposite is compatible with the hypothesis of a Zener pinning pressure exerted by the Ag NPs on the grain boundaries of the TiO_2 NPs [102]. This effect, related to the presence of a finely dispersed distribution of secondary particles or defects within a granular material, is known to prevent or delay the temperature-induced nucleation and recrystallization of the principal grains in a variety of polycrystalline materials [103]. The intensity of the pinning force is determined by several factors, including the radius (r) and volume fraction (f) occupied by the secondary particles. In a three-dimensional, polycrystalline material, temperature-induced grain growth is inhibited when the Zener pinning pressure overcomes the driving force for grain growth [104]. This happens when the grain size of the main phase (R) reaches the Zener limit $R_z = 4r/3f$.

In order to apply the Zener pinning hypothesis to our system, we consider that the mean radius of the Ag NPs in our material is 0.75 nm [51], and that the volume fraction of Ag is $f = \rho_{TiO2}/\rho_{Ag} = (3.4\ g/cm^3)/(10.5\ g/cm^3) \approx 0.32$, thus obtaining a Zener limit R = 3 nm for the TiO_2 NPs. Most of the Ag-TiO_2 NPs in our film have a mean radius of 2.8 ± 1 nm. Since they are composed by a main TiO_2 body partially embedding Ag NPs, as observed by previous transmission electron microscopy measurements [51], we may assume a mean radius of 2 nm for the TiO_2 NPs, which is reasonably close to the radius predicted by the Zener limit. Moreover, since the Zener pinning is not the only force to counteract grain growth, the limit we obtained is likely an overestimation of the grain stagnation limit. The presence of pores and other defects, for example, can introduce an additional energy barrier to the grain coalescence phenomenon [105]. Also, the Zener pinning in 2D systems is a quite different phenomenon than its 3D counterpart. In fact, it has been suggested [106] that the

Zener limit in 2D systems depends on $f^{-1/2}$ rather than f^{-1}, which means that the grain stagnation radius should decrease further as we approach lower-dimensionality systems such as thin films. Since we observe no grain coalescence for temperatures up to 500°C, we deduce that the radius of the TiO_2 particles in the as-deposited film is already higher than the grain stagnation limit. This result indicates SCBD as a preferred method to deposit multielement thin films with high heat resistance.

Above 600°C, the Ag-TiO_2 grain coarsening starts to take place, as shown in Figure 3.4b, where the mode radius of the GSD increases linearly from 20 nm at 500°C to 30 nm at 900°C. This could indicate that the driving force for grain growth has overcome the Zener pinning pressure, leading to a higher grain boundary mobility. The release of the Zener force can be explained by considering a temperature-induced modification of the Ag NPs (see also the optical behaviour described below), by analogy with a statistical mean-field model simulating the grain growth in systems with a time-decreasing pinning force [107]. In the model, the GSD evolution presents an initial stagnation of the average grain size followed by a roughly linear growth regime with time. Even though this is very close to our observations, we recall that here the pinning force decreases with every successive annealing, and not over time, hence we are cannot directly apply such model to our system. However, this approach could likely be used as a starting point for a theoretical description of many types of multielement nanogranular materials.

The RMS follows the temperature dependence of the GSD, as shown in Figure 3.4c. The initial value is almost unchanged up to 500°C, then rapidly increases by up to 25% with subsequent annealing, the sharpest increase being after the annealing step at 900°C. The sharp increase in surface roughness is mainly due to the formation of pits and cracks, which originate

during the grain coarsening of the film. The depth of the cracks ranges from 25 nm up to 50 nm, thus partially exposing the underlying silica substrate.

3.3 Optical properties of the Ag/TiO_2 films

The difference in behaviour between the silica and sapphire-deposited samples during annealing is reflected in the evolution of their optical properties. Panels (a) and (b) of Figure 3.5 show the optical absorption spectra of the films deposited on silica and sapphire, respectively, as a function of the annealing temperature. The spectra are similar for the two substrates up to 600°C. The steep increase in absorption located between 320 and 360 nm is due to TiO_2 interband transitions. The RT spectrum broad absorption band, centered at 451.8 ± 0.8 nm on silicon and at 453.2 ± 0.8 nm on sapphire, has been observed in other Ag/TiO_2 nanocomposite thin films [82,92] and attributed to the surface plasmon absorption of Ag NPs having a radius of 5–9 nm. To the best of our knowledge, there is little to no record of smaller Ag nanoparticles embedded in TiO_2. However, it is well documented that embedded metal nanoparticles usually show a broad absorption band due to the interaction with the surrounding material, like the one we observe in our samples.

Upon annealing the films at temperatures up to 500°C, the maximum of the absorption band is shifted to 522.6 ± 0.8 nm and 526.4 ± 0.8 nm, for the film deposited on silica and on sapphire, respectively. If one considers the size-dependent plasmon frequency of the metal NPs, the redshift could be explained by Ag diffusion through an unmodified TiO_2 matrix forming larger NPs. Diffusion-based coalescence between Ag NPs has been observed in Ag/TiO_2 thin films for temperatures up to 600°C [32]. In this temperature range we did not observe variations of GSD (Figure 3.4a) nor of RMS (Figure 3.4c), that are measured on the

film surface, which implies that the coalescence between Ag NPs doesn't affect the Zener pinning applied to the TiO_2 grains. This can be explained by considering the Ag diffusion along the TiO_2 grain boundaries. As we will see in Chapter 4, the diffusion of Ag for annealing temperatures lower than 500°C is observable via SEM and can justifies the shift in plasmon resonance frequency as larger Ag particles are formed. Also, we have to take into account that defects in the TiO_2 material, such as oxygen vacancies and impurities, could also affect the absorption bands in the visible spectrum. Since annealing can modify such defects, it cannot be excluded that the modification in the optical absorption band could also be caused by a modification of TiO_2, too.

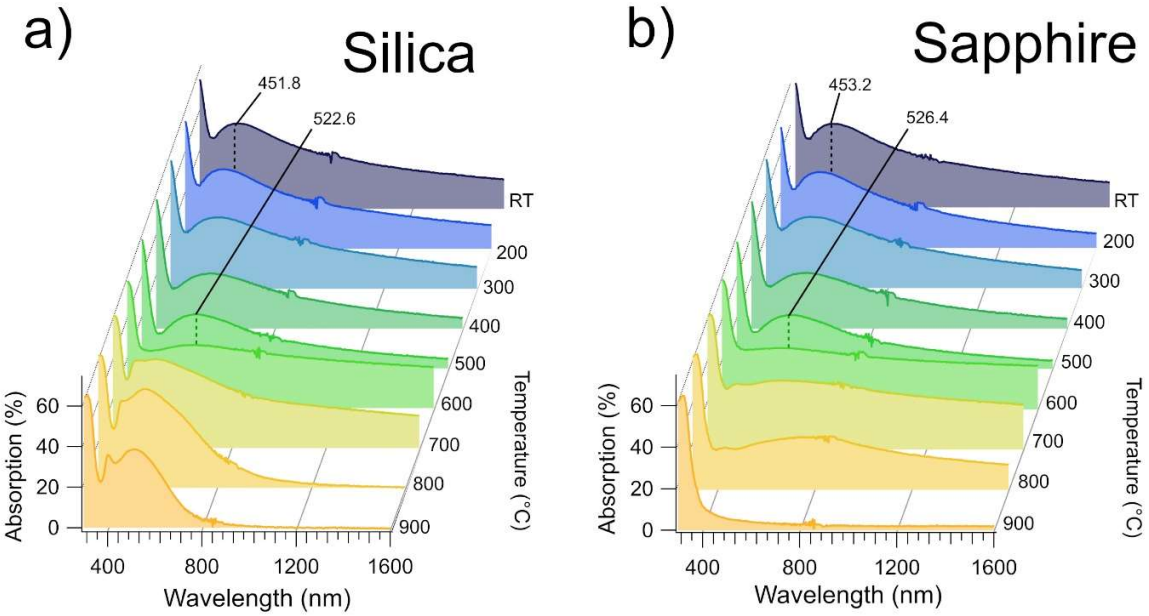

Figure 3.5: a) Optical absorption spectrum of the Ag/TiO2 (AgTi 50-50) film on silica as a function of the annealing temperature. b) Optical absorption spectrum of the Ag/TiO2 (AgTi 50-50) film on sapphire as a function of the annealing temperature.

At 600°C, both films exhibit a broadband absorptivity of 30-32% for wavelengths above 380 nm. It is worth noting that broadband plasmonic absorbers are excellent candidates for light harvesting and hot carrier generation [108,109]. From this perspective, our Ag/TiO_2 film annealed at 600°C could be a very interesting material to study for application in the fields of photo-catalysis, photovoltaics and photodetection.

For temperatures of 700°C and above, the films exhibit a very different behaviour depending on their substrate. For the sample deposited on sapphire (Figure 3.5b), the absorptivity of the film at $\lambda > 800$ nm is steadily reduced after every annealing step, with the film becoming transparent (A = 2.4%) for wavelengths above 380 nm at 900 °C. As observed from AFM data, annealing at 900 °C for 1h on this film results in the formation of Ag clusters on the surface of the film, whose dimensions (570 ± 12 nm) are too large to produce an LSPR oscillation in the visible range, justifying the absence of absorption features in this sample after annealing at 900 °C. In the sample deposited on silica (Figure 3.5a), the annealing process brings to the formation of a new absorption band in the 400–600 nm range of the spectrum.

3.4 Substrate effect on silver diffusion

From the AFM observations, it is clear that silver diffusion in Ag/TiO_2 films can lead to drastically different outcomes depending on the underlying substrate. To fully understand the difference between the samples, and in particular what happens in the silica-deposited sample, we investigated the Ag amount and distribution via SEM and EDX at the end of the annealing process. Panels (a) and (b) in Figure 3.6 show the SEM images taken after annealing at 900°C for 1h on the films deposited on silica and sapphire, respectively, while panels (c)

and (d) show the corresponding Ag EDX maps. On the sapphire-deposited substrate, the images are compatible with AFM data, showing the presence of large (~500 nm) islands on the surface of the film. We can also see that almost all of the Ag signal is concentrated in these islands, as shown by the EDX map. On the other hand, panels (a) and (c) in Figure 3.6 clearly show that Ag is distributed into smaller particles evenly dispersed throughout the TiO_2 film. The overall Ag/(Ag+Ti) atomic ratio, calculated via EDX, is the same for the two substrates within the statistical error (0.205 ± 0.009 for the film on silica and 0.189 ± 0.010 for the film on sapphire).

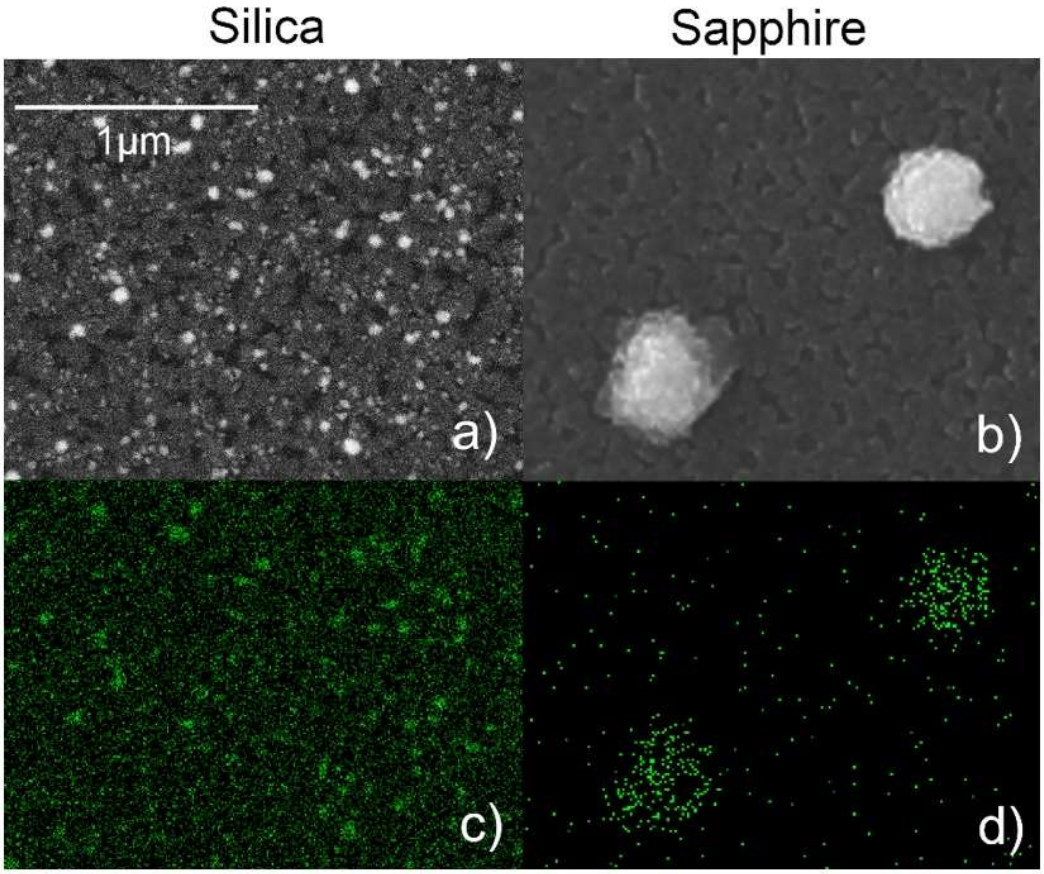

Figure 3.6: a) SEM image (backscattered mode) of the Ag/TiO_2 (AgTi 50-50) film on silica after annealing at 900°C for 1h. b) SEM image (secondary electrons) of the Ag/TiO_2 (AgTi 50-50) film on sapphire after annealing at 900°C for 1h. c) EDX map of the Ag La emission acquired on the same area of (a). d) EDX map of the Ag La emission acquired on the same area of (b).

On each sample, this parameter was calculated by averaging the results obtained on four different areas, spanning a total surface of 120x90 μm^2. Since EDX has a surface sensitivity of about 2 μm, this Ag/Ti ratio is not referred to the film only, but also to a portion of the underlying substrate, meaning that, despite being arranged differently, the overall quantity of Ag is roughly the same on the uppermost part of the samples.

The temperature and composition of the substrate has been shown to play a key role in determining the crystallinity and orientation of TiO_2 [30,110] during deposition. Singh et al. [111] observed that the deposition of TiO_2 on $LaAlO_3$ (001) at 650°C leads to the formation of anatase crystals with a (100) preferred orientation, while the deposition of the same material on Al_2O_3 (0001) at the same temperature leads to rutile crystals with a (200) orientation. Nevertheless, our data clearly show that the evolution of the optical and morphological properties of the films under post-deposition treatments is drastically different depending on the underlying material. Since the films were grown simultaneously by SCBD, their properties are unaffected by the substrate at deposition, depending only on the low-energy ballistic aggregation of the clusters on the surface of the deposition substrates. Moreover, all the samples underwent the same annealing steps, meaning that the difference in distribution of Ag in the two substrates is to be ascribed only to the differences in physical and chemical properties of the substrates. It is hence possible that temperature-induced crystallization of TiO_2 grains develops in different ways depending on the thermal properties and composition

of the underlying material. A substrate-dependent evolution of the morphology during annealing was previously observed in other nanogranular materials such as ZnO [112] and Pt [113] thin films, where the mean dimension and arrangement of the surface grains were different depending on substrate material. However, to our current knowledge, there was no comparative study between annealing-related transformations of TiO_2 on different substrates.

Although the accurate determination of the thermal and physical exchanges at the film-substrate interface is beyond the scope of this work, requiring a considerably different experimental setup and sample preparation, we identified three possible factors which may play a significant role in determining the thermodynamics of the annealing and cooling process of the Ag/TiO_2 films:

Difference in Ag diffusivity: silver atoms are able to diffuse through SiO_2 under annealing temperatures below 600°C [114–116]. Above this temperature, part of the Ag contained in the film deposited on silica film would hence be able to migrate within the substrate during the annealing process, thus lowering the Ag concentration inside the film. To the best of our knowledge, we did not find any work regarding the Ag diffusion through sapphire. We, hence, suppose that this phenomenon could be far less significant in the sapphire-deposited film, thus resulting in the Ag migration towards the surface and the formation of the large islands.

Difference in cooling rate: the thermal conductivity of single-crystal sapphire (30.3 W/mK) [117] is 30 times that of fused silica (1.1 W/mK) [118] at room temperature. Even if the conductivity of sapphire decreases with temperature, it is always at least one order of magnitude higher than that of silica during the entire annealing process: this could play a key role during the heating and cooling cycles of the films. Viana et al. [81] have observed the formation of Ag aggregates on the surface of Ag/TiO_2 nanocomposite films after annealing,

where the dimensions of the aggregates was dependent on the cooling rates: a faster cooling rate produces bigger clusters, and vice versa. In our case, the higher thermal conductivity of the sapphire substrate could lead to a faster cooling process of the associated Ag/TiO_2 film. This, according to Viana et al., could explain the higher cluster size of Ag in the sapphire-deposited sample. It is also worth noting that the sapphire substrate has a lower thickness compared to the silica substrate, which could further affect the cooling rate of the films. However, since the thermal conductivity of sapphire is 10 to 30 times that of silica, while the thickness differs by a factor 2, we expect the effect of thermal conductivity to be the most important factor in determining the cooling rate of the films.

Difference in thermal expansion coefficient: the thermal expansion coefficient of sapphire ($5.0x10^{-6}$ /°C) [117] is nearly an order of magnitude higher than that of fused silica ($4.1x10^{-7}$ /°C) [119]. This may lead to a higher stretching of the deposited film on sapphire and hence favouring the Ag migration towards the surface of the film.

3.5 Effect of silver on the phase transition of TiO_2

Nanocrystalline TiO_2 exists in several polymorphic forms, including amorphous, anatase and rutile depending on synthesis conditions and post-synthesis heat treatments. Since amorphous TiO_2 is thermally unstable, it transforms into anatase or rutile if heated. The temperatures of the amorphous-to-anatase and anatase-to-rutile phase transitions are different, depending on the film synthesis methods and the annealing atmosphere [32,120]. In SCBD-deposited TiO_2 thin films annealed in the air atmosphere, amorphous-to-anatase phase

transition onsets at 400°C, while, after 600°C, there is coexistence of both anatase and rutile phases [65,70].

To investigate the evolution of the crystalline phase of TiO_2, we acquired the vibrational spectra of Ag/TiO_2 films via Raman spectroscopy after every annealing step. Figure 3.7a and 3.7b show Raman spectra of the Ag/TiO_2 films on sapphire and silica for selected temperatures, respectively. At RT, the absence of the characteristic anatase and rutile Raman peaks indicate that the films are amorphous, as previously observed [4]. The weak band located at 150 cm^{-1} is commonly observed in the Raman spectra of silver oxides [121,122].

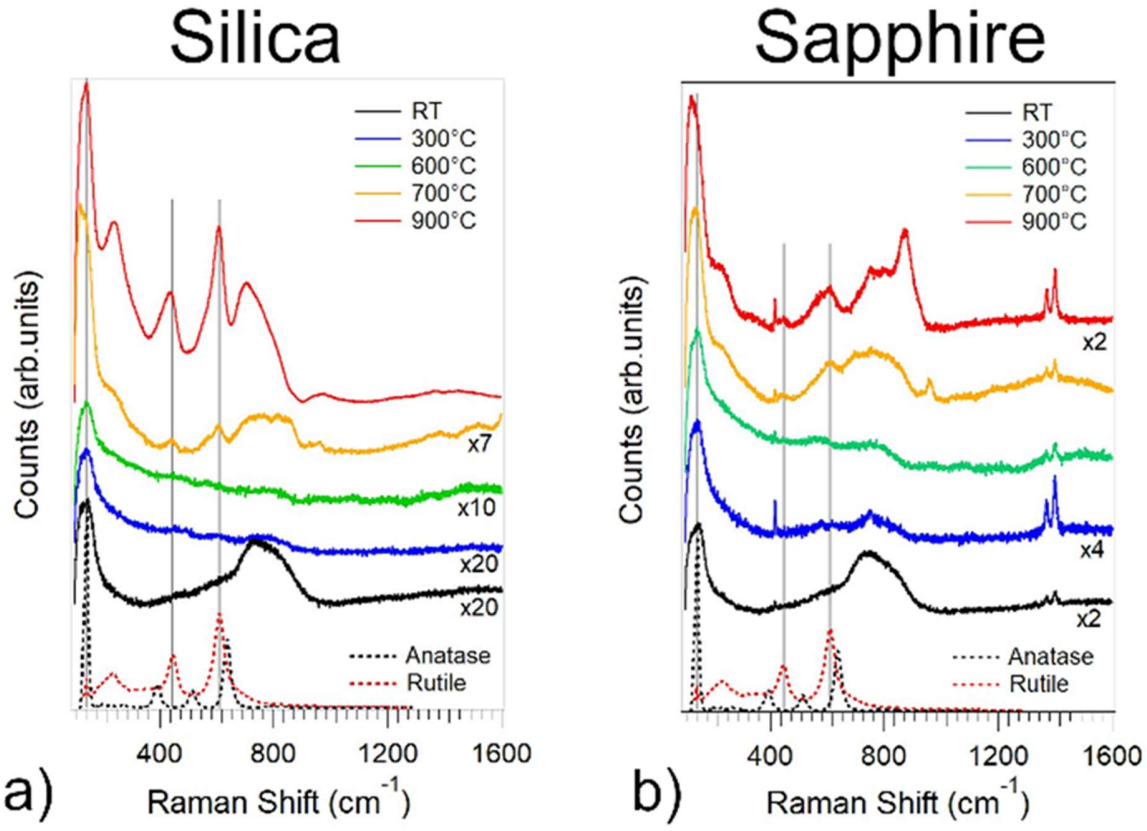

Figure 3.7: Raman spectra of the Ag/TiO2 film on silica (a) and sapphire (b) as a function of the annealing temperature, respectively. The dotted lines represent the Raman spectra of anatase (red) and rutile (black).

The films remain amorphous for annealing temperatures up to 600°C, differently from TiO_2 films only deposited by SCBD, where the phase transition of amorphous TiO_2 to anatase onsets at 400°C [65]. After annealing at 700°C, the Raman peaks of rutile at 244, 440 and 610 cm^{-1} are clearly visible in both films, as shown in Figure 3.7a and Figure 3.7b. Also, the band at 150 cm^{-1} becomes sharper and more intense, presenting a maximum at 144 cm^{-1}, which corresponds to the main vibrational mode of anatase.

The inclusion of Ag NPs in TiO_2 thin films has been observed to deeply affect the phase transition temperatures of TiO_2. In Ag/TiO_2 thin films grown by pulsed cathodic arc, for example, an increase in Ag concentration causes a delay in the amorphous-to-anatase phase transition [32]. For Ag/TiO_2 thin films with Ag:Ti atomic ratio higher that 28% (which is equal to a mass percentage of 46%), amorphous TiO_2 is stable for temperatures up to 600°C, while, for T > 600°C, there is coexistence of both anatase and rutile phases, which is compatible with our observations. Therefore, it is likely that the difference between our films and the TiO_2 films deposited by SCBD is due to the presence of Ag. In particular, the delay of the crystallization process could be related to the Zener pinning pressure applied by the Ag NPs on the grain boundaries of TiO_2.

3.6 Conclusions

We investigated the substrate role on temperature activated processes in nanogranular Ag/TiO_2 thin films deposited on fused silica and sapphire, thanks to the SCBD synthesis method that allowed to deposit identical films on the two different supports. Our observations clearly show that the evolution of the optical and morphological properties of the films under post-deposition treatments is drastically different depending on the substrate. The film morphology is stable up to 600°C, likely due to the Zener pinning pressure exerted by the Ag NPs on the TiO2 grain boundaries. Above this temperature, we observe grain coalescence and formation of both anatase and rutile phases begins, accompanied by a drastic change in the film optical properties. This is explained by hypothesizing Ag diffusion through TiO_2, thus releasing the Zener pinning. Above 600°C, the silver distribution ends up in a completely different way depending on the deposition substrate: on silica, Ag is still present as NPs distributed into the TiO_2 matrix, while on sapphire hundreds of nm wide Ag aggregates are left on top of the film. The optical properties of the annealed films reflect the different size and distribution of the Ag NPs, with the silica-deposited film presenting a broad absorption band in the visible range even after annealing at 900°C, and the sapphire-deposited film becoming almost transparent for wavelengths above 380 nm.

Since the materials were grown by SCBD, their structure at deposition depends only on the low-energy ballistic aggregation of the clusters on the surface of the substrate. Moreover, all the samples underwent the same annealing steps, meaning that the difference in distribution of Ag in the two substrates is to be ascribed only to the differences in physical and chemical properties of the substrates. In particular, the different Ag diffusivity, cooling rate, and thermal expansion coefficient between silica and sapphire could all play an important

role in determining the thermodynamics of the annealing process and the final properties of the film [49].

CHAPTER 4:

PHOTOTHERMAL TRANSFORMATIONS IN ANNEALED AGTIO$_2$ THIN FILMS

4.1 Background and motivation

Localized surface plasmons are known to not only produce an intense localized electric field, but to also give rise to local photothermal heating when excited by an external light source [123,124]. The heating effect is enhanced at plasmon resonance, i.e. when the energy of the incident photons is close to the plasmon frequency of the nanoparticles. The large absorption cross sections and tunability of plasmonic nanoparticles makes them prime candidates for photothermal agents in applications such as plasmon-enhanced photochemistry, where the local heating produced by the nanoparticles is exploited to activate reactant molecules and boost numerous types of chemical reactions [125,126]. The generated heat can also be used for melting the surrounding matrix, like in the case of ice or polymers [123,127], as well as for cancer diagnosis and therapy [128]. However, in the case of metal-oxide nanocomposites, where the surrounding matrix exhibits a higher melting temperature, photothermal heating can lead to the melting of the metal nanoparticles themselves, followed by a drastic change in the properties of the material. This phenomenon can be exploited to induce specific transformations in the material after deposition.

The melting of nano-objects is a well-known and well-studied phenomenon. If the heating happens by conduction only, the melting process of small metal particles is usually modelled as a Stefan problem, where the melting point of the nanoparticle decreases with the particle size [129–132]. However, particles embedded in a matrix can behave differently, leading to the phenomenon of overheating, as found for example in Pb and In nanocrystals embedded in aluminium matrix [133,134], or Ag particles embedded in Ni [135]. Several reports indicate that superheating only happens in some matrices, while the same nanoparticles embedded in some other matrices show lower melting temperature. According to Sheng et al., this could be related to the epitaxy between the nanoparticles and the embedding matrix [134]. Furthermore, in the melting of nanocomposite materials, a large difference in thermal conductivity between the embedded particles and the surrounding matrix can lead to longer annealing times and a less efficient heating. In the case of Ag-TiO_2 nanocomposites, for example, the reported thermal conductivity of Ag is $430\ Wm^{-1}K^{-1}$, while the thermal conductivity of TiO_2 is much smaller at $7\ Wm^{-1}K^{-1}$ [136].

When it comes to light-induced melting, new and not fully understood mechanisms emerge. In the case of photothermal heating of plasmonic nano-objects, for example, heating is no longer achieved by conduction only, but electron excitation and subsequent electron-electron and electron-phonon scattering [137,138]. This can lead to large temperature gradients near the excited nano-objects near resonance, due to the plasmon-enhanced optical absorption and highly localized electric fields involved in the plasmonic oscillation [138]. For this reason, light-induced melting can be used as a more versatile alternative to conventional thermal annealing for inducing microstructural modifications in nanocomposite materials.

In the case of metal-semiconductor nanocomposites such as Ag-TiO_2 thin films, metal nanoparticles are often specifically designed to harvest light at visible wavelengths. After light absorption, "hot electrons" can be created in the metal particle and injected into the semiconductor, greatly increasing the performance of the material in novel applications such as photocatalysis and photovoltaics [139,140]. In this perspective, given the high absorption profile of metal nanoparticles in the visible range of the spectrum, light-induced melting can be used to control the final size of the metal particles, which in turn deeply affects the carriers' injection yield [139,140]. A significant example of this technique is given by the work of Liu et al., where the authors were able to obtain a large variety of different Ag size distributions by changing the scanning speed of the incident laser [141]. In fact, silver nanoparticles subjected to laser illumination can either shrink as a result of photo-oxidation or grow as a result of the high temperature rise and coalescence. This oxidation-reduction process depends on the initial Ag nanoparticle size and is also responsible for the multicolour photochromism often found in Ag-TiO_2 nanocomposites [86,87,142].

In this chapter, we will address the light-induced transformations of Ag-TiO_2 thin films deposited by SCBD on a silica substrate, combining both traditional oven annealing and white light illumination to achieve different outcomes for the final Ag nanoparticle size distribution. For embedded Ag nanoparticles, the plasmonic absorption peak is rather large due to the interaction with the surrounding matrix, which is why we used a continuous white light source instead of a laser, with the added advantage of being able to illuminate larger samples without the need for a raster process. Also, while pulsed laser annealing and flash-lamp annealing of plasmonic structures are well-studied, especially in recent years, continuous white light annealing is a relatively unexplored technique.

In Section 2, we will show the heat-induced diffusion and growth of Ag nanoparticles in the TiO_2 matrix during oven annealing at high temperatures, while in Section 3 we will show the effect of white light illumination on the Ag-TiO_2 nanocomposite samples and analyse the changes in optical properties and nanoscale structure.

4.2 Heat-induced diffusion of silver in Ag/TiO_2 thin films on silica

In the previous chapter, we have shown that thermal annealing can lead to Ag diffusion and segregation in Ag/TiO_2 thin films deposited by SCBD. However, this phenomenon produces different results depending on the underlying substrate. On the films deposited on sapphire, the Ag diffusion is also accompanied by segregation leading to the formation of nanoislands on the surface of the films, observed via AFM. On the films deposited on silica, however, the Ag diffusion activates Ag clustering taking place under the surface [49]. Since the Ag clustering induces a drastic modification in the optical absorption profile of the films, we expect that the photothermal heating of the films will be more or less noticeable depending on the annealing temperature: for example, films with a broader absorption feature should be able to generate more heat than films exhibiting a single, sharp absorption peak. Furthermore, the oxidation-reduction processes observed during the illumination of Ag-TiO_2 nanocomposites have already been shown to depend on the initial size of Ag nanoparticles [141]. To further investigate the physical behavior induced by annealing in metal-oxide thin films at the nanoscale, we deposited 48 ± 2 nm thick $AgTiO_2$ thin films on silica via SCBD and we analysed their behaviour after annealing at high temperatures via SEM. The annealing

steps were performed in the same way as previously mentioned [49]. The SEM images were taken in both backscattered and secondary electrons mode, to obtain information about the vertical distribution of silver during annealing. In fact, while secondary electrons are usually used to investigate the uppermost few nanometers of a sample, backscattered electrons can gather information from the entire depth of our film, up to ~1 μm, and is therefore more suitable to investigate the entirety of the sample [143].

Figure 4.1 shows the backscattered electrons map for different annealing temperatures. Here, we can clearly identify Ag as the brighter component in the image, due to the atomic number sensitivity of SEM. In the as-deposited sample, the Ag nanoparticles are finely distributed in the TiO_2 matrix. As we have seen in previous chapters, the average size of the Ag component in the clusters is smaller than 2 nm, which is below than the spatial resolution of the SEM. This is why the nanoparticles don't appear as clearly defined objects, but rather like a finely dispersed distribution. However, as the sample is annealed at higher temperatures (400°C), we clearly see the result of diffusion and coalescence of Ag, as larger (~5-10 nm) nanoparticles are formed. Given the lower melting temperature of Ag compared to TiO_2, it is likely that the nanopores in the TiO_2 matrix act as molds in this phase of the annealing process, playing a key role in the dynamics of Ag diffusion [86]. Nevertheless, the vast majority of the silver nanoparticles remains finely dispersed inside the TiO_2 matrix.

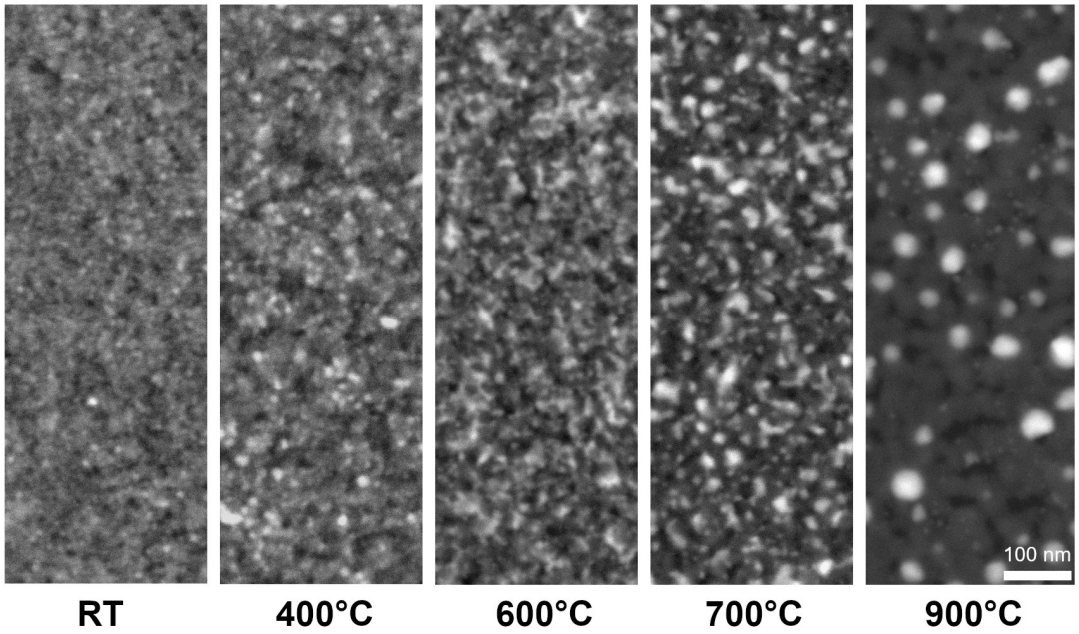

Figure 4.1: Backscattered SEM images of 50 nm Ag-TiO_2 thin films on silica as a function of the annealing temperature (magnification: 100.000x). The brighter parts of the image represent the distribution of Ag inside the film.

For annealing temperatures of 600-700°C, some of the smaller aggregates are still present, while larger interconnected structures (~50-100 nm) start forming. By comparing Figure 4.1 with Figure 3.3 in the previous chapter, we can clearly see that similar structures also form on $AgTiO_2$ thin films deposited on sapphire, albeit on the surface of the sample, instead of inside the TiO_2 matrix. Finally, after annealing the films at 900°C for 1h, Ag segregates in clearly defined nanoparticles with a measured average diameter of 22 ± 3 nm, as measured by SEM. It is likely that the size of the nanoparticles at this point is only defined by

the initial density of Ag in the film, which can be easily modified in SCBD by using a different target rod.

4.3 Photothermal heating of Ag nanoparticles

After annealing the samples at high temperatures, we investigated the effect of room temperature white light illumination on the as deposited and thermally annealed films, via SEM and optical spectrophotometry. The light source was a 175W Xenon gas discharge lamp, set at 30 cm from the sample. White light exposure was performed in 3 steps of 10 minutes each. After each step, spectrophotometry was performed to monitor the evolution of the absorption behaviour of the samples. Figure 4.2 shows the optical absorptivity of the samples annealed at different temperatures, before and after exposure to white light. The spectra obtained after annealing are compatible with previous measurements of the optical properties of Ag-TiO_2 films deposited on silica [49] and mirror the evolution of the morphological properties of the films at the nanoscale. In particular, the redshift of the plasmonic absorption band from 458 nm to 538 nm (Figure 4.2, panels a and b) can be attributed to the increase in the average size of the Ag nanoparticles observed by SEM (Figure 4.1). In fact, larger metal nanoparticles are usually associated to a larger absorption wavelength [145].

For annealing temperatures of 600°C and 700°C, the broadband optical absorption band (Figure 4.2, panels c and d) can be justified by the presence of a large variety of different Ag nanostructures inside the TiO_2 matrix: as observed by SEM, this stage of the annealing process is associated with the formation of large (50-100 nm) silver aggregates, which coexist with smaller particles (Figure 4.1). This broadband absorption feature could be of great interest

for applications in photocatalysis, photovoltaics and photodetection. In fact, much effort has been devoted in the past years to design broadband plasmonic absorbers with the aim of enhancing hot-electron charge generation and separation [108,146,147]. Furthermore, a spectrally broad LSPR band is highly desirable in detection applications via surface-enhanced Raman spectroscopy, to achieve resonant matching to a large variety of electronic transitions in the detected species [148]. Finally, in the samples annealed at 900°C (Figure 4.2e), the double-peak absorption band can be associated to the coalescence of Ag into more clearly defined nanoparticles, as seen by SEM (Figure 4.1).

After exposing the samples with white light, we can observe a drastic difference in behaviour between the samples, depending on their annealing temperature (Figure 4.2). The unannealed sample (panel a) and the sample annealed at 900°C (panel e) show no substantial change in optical absorptivity after light exposure, while the sample annealed at 400°C (panel b) shows a shift of the optical absorption band from 538 to 464 nm after 10 minutes of white light exposure. This phenomenon is interesting, since we observe a blueshift, and not a redshift, of the plasmonic absorption band. Following our consideration on the dependence of the plasmon resonance frequency, this should correspond to particles shrinking after white light illumination. A possible explanation of this phenomenon is that white light is responsible for breaking down larger Ag aggregates, which have a broader absorption profile, into smaller particles. In fact, the final spectrum of the film annealed at 400°C closely resembles that of the as-deposited film, except for a ~20% drop in absorption in the visible range due to the annealing process. On the other hand, the samples annealed at 600°C and 700°C (panels c and d) show a dramatic decrease in absorptivity after white light illumination, from ~25% to less than 3% in the visible and infrared region of the spectrum, after which the broadband absorption feature transforms into a narrower band centered at 456 nm.

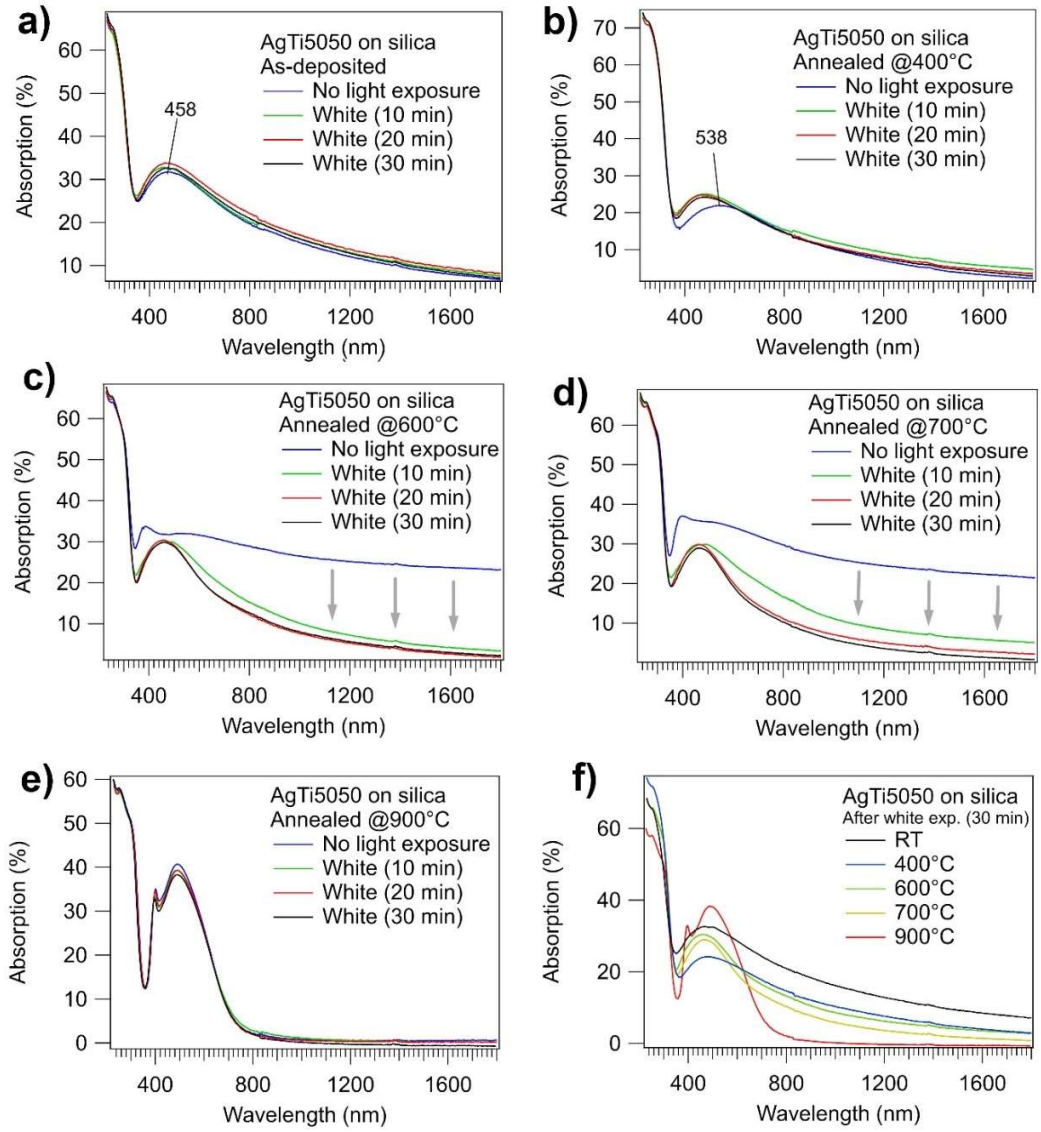

Figure 4.2: Panels a-e): optical absorption spectrum of the Ag/TiO_2 (AgTi 50-50) film on silica at different annealing temperatures, before and after exposure to continuous white light. Panel f): optical absorption spectra of the Ag/TiO_2 (AgTi 50-50) film on silica annealed at different temperatures, then exposed to white light (30 min).

This remarkable transformation is not unexpected: in fact, as we have already mentioned, the samples annealed at 600°C and 700°C exhibit a much broader absorption feature in the visible range. This allows them to more effectively collect light from the entirety of the visible spectrum, transforming it into localized heat. In turn, the heat heavily modifies the structure of the particles: Figure 4.3 shows the SEM images of the sample annealed at 700°C before and after light exposure. From the comparison between the images, we can see that the exposure to white light causes the silver particles to recrystallize into more clearly defined particles. Furthermore, in the comparison between the secondary electrons emission map (panels b and d) we can see, thanks to the atomic number sensitivity of the SEM, that the Ag particles are also brought to the surface by the exposure to light.

The ability to manipulate the spatial distribution of plasmonic nanoparticles is especially useful in plasmon-enhanced microscopy techniques: in fact, similar metal-semiconductor heterostructures have been widely used recently as effective SERS substrates for biosensing and detection of dye molecules [4,149–151]. Such materials present a double advantage: first, metal-semiconductor interfaces can show enhanced synergistic charge transfer effects [152]; second, metal nanoparticles embedded in a matrix show enhanced chemical stability, increasing the durability of the substrate compared to single and dispersed nanoparticles [4].

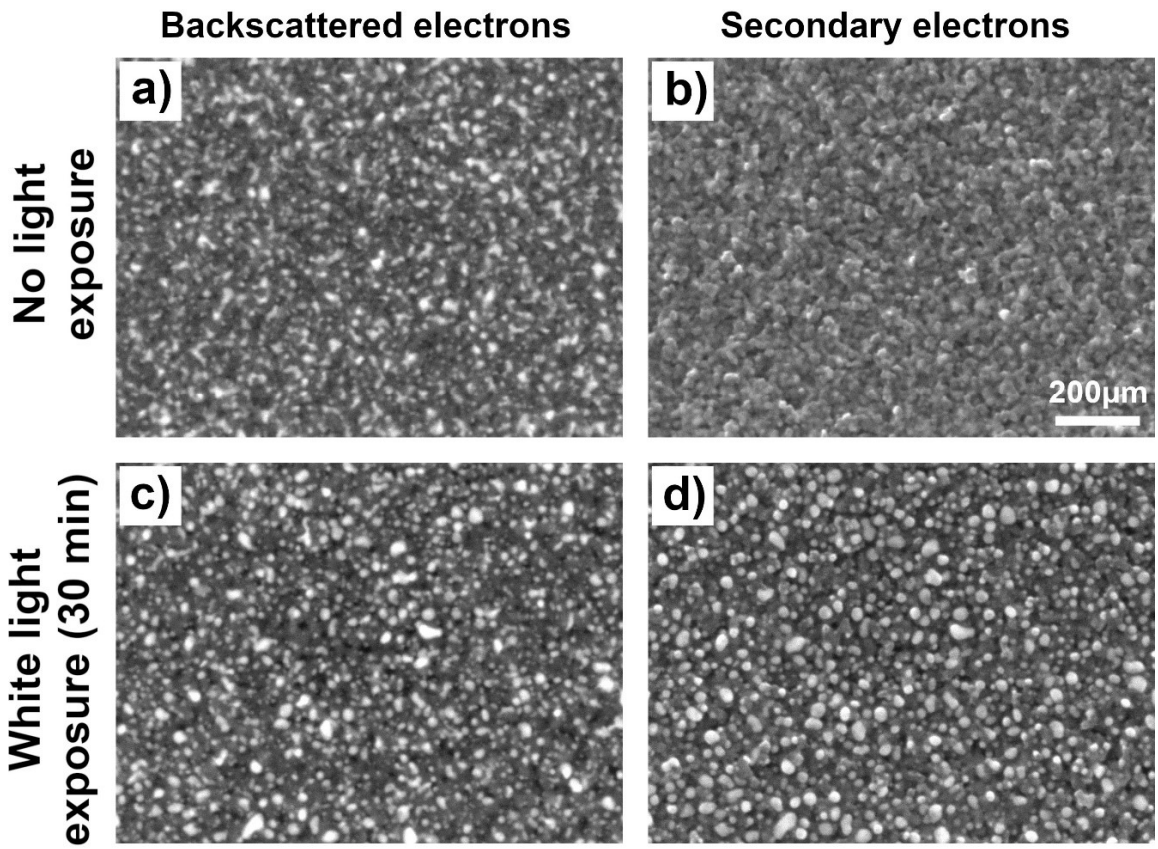

Figure 4.3: Backscattered (panels a and c) and secondary electrons emission (panels b and d) SEM images of 50 nm Ag-TiO_2 thin films on silica annealed at 700°C for 1 h, before and after exposure to white light (30 min). The brighter parts of the image represent the distribution of Ag inside the film.

4.4 Conclusions

We studied the optical and morphological transformations induced by both conventional oven annealing and white light illumination in 48 nm thick Ag-TiO_2 thin films deposited by SCBD on silica. Our findings show how post-deposition processes can impact the nanoscale properties of metal-semiconductor nanogranular thin films deposited by SCBD, allowing to functionalize them for different applications depending on the qualities required. The electron microscopy images taken on the films before and after annealing show that the diffusion and coalescence of silver nanoparticles onsets at 400°C, leading to a redshift in the absorption band of the film: this is compatible with the lowering of the melting temperature of small nanoparticles compared to the bulk material observed in literature. After annealing at 600-700°C, we observe the formation of larger interconnected silver nanostructures, which are responsible for the broadband optical absorption of the samples.

The formation of self-assembled broadband absorbers in metal-semiconductor thin films is very interesting, since it can be used to improve the light harvesting and hot electron generation in photovoltaic and photocatalytic devices [108,146,147]. In this perspective, oven annealing can be used as a cheap and scalable way to achieve large-scale production of these devices. Finally, after annealing at 900°C for 1h, we see the formation of clearly defined, spherical silver nanoparticles inside the TiO_2 matrix. It is likely that the final size of the nanoparticles can be easily modified by changing the Ag percentage in the target material at deposition. In addition, the combined effect of oven annealing and light-induced transformations have a dramatic effect on the overall silver distribution: for example, in the samples annealed at 600 and 700°C, exposure to white light leads to the nucleation and surfacing of Ag nanoparticles, whose final size distribution is 3.9 ± 4.1 nm. The surfacing of

silver nanoparticles is particularly interesting for application in plasmon-enhanced microscopy techniques such as SERS, where embedded metal nanoparticles are used to increase the durability and reusability of the substrates [4]. Furthermore, the self-assembled nature of our Ag-TiO_2 films implies a lower production cost compared to other laboratory techniques such as nanolithography.

From our observations, it's clear how the localized heating produced by the photothermal effects in the Ag nanoparticles and the diffuse heating produced by oven annealing lead to completely different outcomes. It is also worth mentioning that the post-deposition functionalization of $AgTiO_2$ is made possible by the exceptionally small initial size distribution of silver nanoparticles (1-2 nm) [51], which allows silver diffusion and coalescence. For this reason, cluster-based deposition techniques such as SCBD are here reaffirmed to be prime choices for the production of tunable plasmonic devices.

CHAPTER 5:

CLUSTER-BASED METACRYSTALS FOR STRUCTURED ILLUMINATION MICROSCOPY

5.1 Background and motivation

Fluorescence microscopy is an indispensable tool in modern biology, enabling high-resolution visualization of cellular structures, molecular interactions, and dynamic biological processes with exceptional specificity and sensitivity. Since the development of the first fluorescence microscopes in the early 1900s, by the companies Carl Zeiss and Carl Reichert, fluorescence microscopy has undergone significant advancements that have transformed biological research [153]. The ways of labeling a specimen greatly expanded over the decades: in the early 1940s, fluorescent antibody labeling was developed [154], while in the 1990s the cloning of the green fluorescent protein (GPF) and its spectral variants allowed protein labeling and tracking in real time [155,156]. Furthermore, the development of new instrumentation and techniques such as confocal microscopy greatly enhanced the optical sectioning capabilities and image clarity [157].

However, compared to other microscopy techniques such as electron microscopy, conventional fluorescence microscopy is limited by the diffraction of the light. In fact, the resolution of a traditional optical microscope can be expressed as $\Delta x \sim \lambda/2NA$, where λ is the wavelength of light and NA the numerical aperture of the setup [158]. For most imaging setups, this results in a lateral resolution of 200-300 nm, which is comparable to or larger than many subcellular structures [159].

To overcome this resolution limit, one can use light with a shorter wavelength, however, using high-energy illumination can lead to photodamage to biological cells, limiting the ability to observe their behavior [160]. For this reason, a variety of "super-resolution" techniques have been developed in recent years to overcome the diffraction barrier without resorting to high-energy illumination.

A successful approach to super-resolution developed by S. W. Hell and J. Wichmann [41] and later experimentally demonstrated by Klar et al. [161] is stimulated emission depletion (STED), which employs nonlinear effects to selectively suppress fluorescence in specific regions of the sample, minimizing the illumination area at the focal point. A related, more general method employs reversible saturable optically linear fluorescence transitions (RESOLFTs) to overcome the diffraction limit of light [162]. This approach works by employing specific fluorophores which can be switched between an "on" and "off" state using reversible optical or chemical transitions. Compared to STED, RESOLFTs microscopy uses lower-intensity light, making it less phototoxic and better for live-cell imaging. However, it shares the low imaging speed of STED, while also requiring specific fluorophores to enable the required transitions.

Other techniques, such as stochastic optical reconstruction microscopy (STORM) [163] and photoactivated localization microscopy (PALM) [42,43], achieve nanoscale imaging by slowly controlling the activation of blinking fluorophores or photo-activable fluorescent proteins, which act as point-like emitters. A high-resolution image can then be obtained by acquiring a large number of images each with a very small number of excited fluorophores. For this reason, image acquisition is usually very slow, requiring thousands of images. Also, depending on the observed sample, the computational demand for reconstructing the high-resolution image can be complex and time-consuming. Near-field scanning microscopy

(NSOM) [164] employs a different approach, focusing the exciting laser through a nanoscale aperture or sharp tip and exploiting the properties of evanescent waves to scan the sample at a distance smaller than the wavelength of light. Requiring a precise tip-sample control, the use of NSOM is often limited to small scan areas; furthermore, the probe cannot penetrate deep into biological tissues, limiting the technique to surface imaging.

Compared to the aforementioned techniques, structured illumination microscopy (SIM) has several advantages when it comes to the observations of cellular processes, being a wide-field technique with a higher imaging speed and compatibility with a wide variety of fluorophores [45,165]. In SIM, the sample is illuminated with different high-frequency illumination patterns, creating moiré fringes that encode high-resolution information from structures smaller than the diffraction limit. By acquiring multiple images with different illumination patterns, it becomes possible to mathematically extract and reconstruct fine spatial details that would otherwise remain unresolved in conventional fluorescence microscopy.

Standard SIM usually employs two-beam or three-beam interference to produce sinusoidal interference patterns [166–168]. However, recent advances in the field have explored new ways to generate the illumination patterns: in this perspective, plasmonic materials stand out because of their ability to produced high intensity localized electric fields. Plasmonic structured illumination microscopy (PSIM) employs surface plasmon polaritons (SPPs) to generate a high-frequency illumination pattern. Since SPPs are confined to the substrate surface, the intensity of the illumination pattern decays within tens of nanometers from the surface, effectively suppressing background fluorescence. Furthermore, in certain setups, the high-frequency illumination pattern can be excited with a single beam using appropriately structured metal films [169,170]. A variant of PSIM, named localized plasmonic

structured illumination microscopy (LPSIM), makes use of localized plasmons (LPs) excited near nanostructures periodically placed directly on the microscope slide [46,171]. Here, the frequency of the illumination pattern is not determined by that of the illumination light, but only by the spatial period of the chosen nanostructured pattern. In conventional SIM, the precise knowledge of the illumination patterns is required in order to precisely reconstruct the object pattern from the diffraction-limited images. However, as we mentioned in Chapter 1, recent advances in the field have introduced new algorithms that allow image reconstruction without knowing the illumination patterns. The validity of this blind structured illumination microscopy (Blind-SIM) was demonstrated both theoretically and experimentally by Mudry et al. [47], who achieved a resolution about two times better than conventional wide-field microscopy by illuminating the sample with several uncontrolled random speckles, provided that their density is roughly homogeneous over the sample. Ponsetto et al. have successfully integrated the Blind-SIM algorithm with LPSIM, by using a silver nanodisc array as a substrate [172]. In this perspective, self-assembled supported plasmonic metal nanoparticles could provide an excellent substrate for Blind-SIM, providing the required different speckle illumination patterns while also being relatively easy to manufacture. Furthermore, tuning the nanoparticle size and material could be extremely important in the optimization of SIM substrates, allowing their use with different fluorophores and excitation wavelengths.

So far, we have shown how the optical properties of a paradigmatic metal-oxide plasmonic nanocomposite, Ag/TiO_2, deposited by supersonic cluster beam deposition (SCBD), can be tweaked using post-deposition annealing and a careful design of the deposition substrate [49]. In particular, the size and distribution of the silver nanoparticles are dependent on the annealing temperature, ranging from ~1-2 nm at deposition to ~600 nm after annealing at 900°C. We have also shown that the plasmon-mediated photothermal heating can be

exploited to further affect the Ag distribution in AgTi thin films deposited on silica, promoting Ag nucleation and surfacing. Furthermore, the plasmonic absorption band of the Ag/TiO_2 nanocomposites deposited by SCBD sits in the visible range at ~450-500 nm, corresponding to some of the most commonly used excitation sources in standard fluorescence microscopy setups. All these properties suggest that Ag/TiO_2 nanocomposites could be versatile LPSIM substrates, providing a random speckle pattern with a controllable size and satisfying the homogeneity requirements of the Blind-SIM reconstruction algorithm. In this chapter, we will analyze the viability of this material in existing LPSIM configurations: in section 2, we will focus on deriving the dielectric function of our material by combining the Drude-Lorentz oscillator model with Bruggeman's effective medium approximation (EMA). In section 3, we will use the derived effective optical constants of Ag/TiO_2 to simulate the response of the electric field around the substrate under external illumination. Finally, in section 4, we will propose a method for fabricating cluster-based metacrystals, which involves EBL nanopatterning and SCBD deposition of the desired material.

5.2 Effective optics model for nanogranular $AgTiO_2$

To evaluate the possible application of a substrate in structured illumination microscopy, one must verify that the designed structure is able to produce different illumination patterns. This is usually achieved by exciting a specific resonant state of the system, usually a nanopatterned material, with an external electromagnetic wave. These modes correspond to standing waves of electromagnetic fields, phonons, plasmons, or other excitations that are characteristic of the nanostructure's geometry and material properties

[172,173]. A simulation of the excited electromagnetic field can be achieved in dedicated software like COMSOL or Lumerical, by replicating the geometrical features of the substrate and simulating the response of the material after being irradiated by a plane wave. This is a straightforward process if the dielectric constants of the materials involved are well-known, as in the case of silver and gold nanostructures. However, in the case of composite systems with a large number of interfaces, like our Ag/TiO_2 nanogranular thin film, the derivation of the dielectric constants can be challenging: in fact, replicating the actual geometry of the thin films is a highly inefficient and time-consuming approach. Instead, since the lengths associated with local variation in permittivity in our material are well below the wavelength of light, we can treat our material as an effective homogeneous medium characterized by a dielectric function ε_{eff}.

To do that, however, we must consider that the presence of voids or pores inside the film, can deeply affect the overall dielectric function of the medium [174]. The same can be said for films with a surface roughness comparable with the film thickness. In both cases, Bruggeman's effective medium approximation (BEMA) can be used to calculate the effective dielectric function of the material [175–177]. In the BEMA model, if a material is composed of N elements, the effective dielectric function ε_{eff} can be found by solving Bruggeman's equation:

$$\sum_{i=1}^{n} f_{(i)} \frac{\varepsilon_{(i)} - \varepsilon_{eff}}{\varepsilon_L + q\left(\varepsilon_{(i)} - \varepsilon_{eff}\right)} = 0; \tag{5.1}$$

where $\varepsilon_{(i)}$ are the dielectric functions of each of the components, $f_{(i)}$ their volume fraction, and q the depolarization factor, which is related to the shape of the inclusions: for $q = 0$, the inclusions have a sheet shape with an oscillation parallel to the electric field; for $q = 1/3$, the inclusions are sphere-like, while for $q = 1$ the inclusions become pillar-like with sides normal to the electric field.

To find the dielectric function of our Ag/TiO_2 film, we modeled our film using a recently developed code (Determination of Effective Multilayer Optical constants for Nanotechnology – DEMON) [178]. This code allows us to build a multilayer geometry, where each layer can be described by any number of custom oscillators. The code then calculates the dielectric function of each layer through BEMA, giving the overall R and T spectra of the film. To model our Ag/TiO_2 composite film, we used a bilayer geometry comprised of a core layer and a roughness layer, as shown in Figure 5.1. In Chapter 1, we mentioned how the optical permittivity of a general medium can be expressed analytically by a Drude-Lorentz (DL) multioscillator model of the form:

$$\varepsilon_r(\omega) = \varepsilon_r^{(D)}(\omega) + \varepsilon_r^{(L)}(\omega) = \varepsilon_\infty - \frac{\omega_p^2}{\omega^2 + i\omega\gamma} + \sum_{l=1}^{K} \frac{f_l \omega_p^2}{\omega_{0l}^2 - \omega^2 - i\omega\gamma_l}; \qquad (5.2)$$

where $\varepsilon_r^{(D)}(\omega)$ is a Drude oscillator describing the intraband contributions, and $\varepsilon_r^{(L)}(\omega)$ is a sum of N Lorentz oscillators describing the interband contribution to the dielectric function of the medium. This model has been extensively used to describe both noble and transition metals, including Ag and Ti [179]. Since the clusters in our material are composed of two

elements, one way to find the effective medium of our system is to double our DL oscillator model, since Ag and Ti have their own characteristic interband and intraband transitions:

$$\varepsilon_{AgTi} = \varepsilon_{TiO2}^{(D)}(\omega) + \varepsilon_{TiO2}^{(L)}(\omega) + \varepsilon_{Ag}^{(D)}(\omega) + \varepsilon_{Ag}^{(L)}(\omega). \quad (5.3)$$

Here, $\varepsilon_{TiO2}^{(D)}(\omega)$ and $\varepsilon_{Ag}^{(D)}(\omega)$ are Drude oscillators, and $\varepsilon_{TiO2}^{(L)}(\omega)$ and $\varepsilon_{Ag}^{(L)}(\omega)$ are Lorentz oscillators. Here, instead of taking a sum of N independent Lorentz oscillators, we simplify the equation by taking a single Lorentz oscillator to model the interband transitions in TiO_2. In a similar fashion, the function for the interband transitions in Ag can be expressed as a single modified Lorentz oscillator:

$$\varepsilon_{Ag}^{(L)}(\omega) = A_{lor}\frac{(\Gamma_{lor}^2)}{(\omega-\omega_{lor})^2+\Gamma_{lor}^2} + i\left[b + \frac{H}{1+e^{(\omega_c-\omega)/s}}\right]; \quad (5.4)$$

where the real part is a Lorenz oscillator with amplitude A_{lor}, width Γ_{lor} and position ω_{lor}, and the imaginary part is a step function centred at ω_c with amplitude H, width s, and offset b [178]. To validate our model, we compared the calculated reflectivity and transmissivity spectra obtained from the dielectric function of the composite material with the experimental spectra obtained via UV-Vis spectrophotometry on a 50 nm Ag-TiO_2 thin film on silica. The samples were deposited via SCBD using the deposition process explained in previous chapters [49].

Table 5.1 shows all the parameters for the Drude and Lorentz oscillators used in our calculations (no errors are present since they are simulation parameters rather than fit

parameters). To account for the pores in the film structure, a BEMA was performed using ε_{AgTi} as one of the components and vacuum ($\varepsilon = 1$) as the second one. For the core layer, we obtained a thickness of 36.8 nm with a vacuum volume fraction of 22%, while for the roughness layer, we obtained a thickness of 8.34 nm with a vacuum volume fraction of 50%. Fig. 5.1b shows the experimental (dotted line) and calculated (solid line) transmissivity, reflectivity, and absorptivity of a 50 nm as-deposited Ag/TiO_2 thin film. The calculated optical spectra show a good agreement with the experiments, highlighting how the combination of a multilayer geometry and the BEMA approach can be an effective tool to model the dielectric properties of complex porous materials.

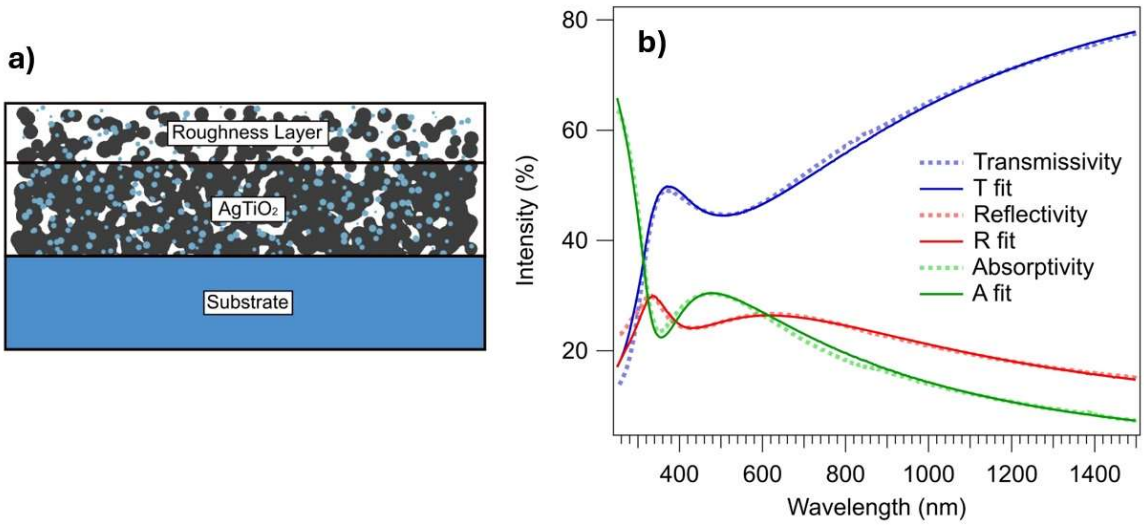

Figure 5.1: a) Multilayer model scheme for Ag/TiO_2 nanoparticles on silica; b) Measured (dotted line) and simulated (solid line) transmissivity, reflectivity and absorptivity spectra for a 50 nm Ag/TiO_2 thin film on silica.

TABLE 5.1

PARAMETERS FOR THE MULTIOSCILLATOR MODEL FOR $AGTIO_2$

Oscillator	Parameter	Value
$\varepsilon_{TiO2}^{(D)}(w)$	$f\hbar\omega_p(eV)$	4.0
	$\hbar\gamma^{(D)}(eV)$	2.0
$\varepsilon_{Ag}^{(D)}(w)$	$\hbar\omega_p(eV)$	9.2
	$\hbar\gamma(eV)$	2.0
$\varepsilon_{TiO2}^{(L)}(w)$	$\hbar\omega_p(eV)$	7.89
	$\hbar\gamma^{(L)}(eV)$	0.92
	$\hbar\omega_0(eV)$	3.77
$\varepsilon_{Ag}^{(L)}(w)$	A_{lor}	1.70
	$\hbar\omega_{lor}(eV)$	3.95
	$\hbar\Gamma_{lor}(eV)$	0.25
	H	3.26
	b	0.19
	$\hbar\omega_c(eV)$	4.06
	$\hbar s(eV)$	0.09

5.3 Simulation of the illumination pattern

In Chapter 1 we have mentioned how in SIM it is possible to reconstruct a high-resolution object pattern by taking multiple diffraction-limited images of the object under different illumination patterns. We also anticipated how plasmonic nanostructures based on SPs and LSPs have been used in the recent years as promising platforms for SIM. In order to be used in SIM, a nanostructure must meet two important criteria: first, it has to support an optical mode with a high effective mode index near the surface of the structure; second, it has to be designed so that the phase of the illumination pattern can be sufficiently tuned. This is usually achieved by altering the angle of the plane wave incident to the nanostructures [173]. So far, different nanopatterned structures have been proposed as substrates for LPSIM: Ponsetto et al. used a silver nanodisc array embedded in glass [172], while Haug et al. employed a silver nanoridge array [173]. The main difference between existing Ag substrates and embedded Ag nanoparticles is that the illumination pattern in the first case will be determined by the frequency of the optical mode excited on the top of the surface, while in the case of embedded plasmonic nanoparticles the illumination pattern will result from the highly localized electric field generated from the plasmonic excitation. Nevertheless, to avoid "blind spots", i.e. regions where no plasmonic excitation is present, we must make sure that the optical modes excited in our nanostructures can be tuned in phase.

To do this, we set up a simulation in COMSOL to investigate the behaviour of the material under external plane wave excitation. We chose two different designs for our simulations, as shown in Figure 5.2. The first design consisted of a nanoridge array, with the ridges having width w, length l, thickness h, lateral periodicity ps, and longitudinal periodicity pl. The second design consisted of an array of nanocylinders of diameter d and thickness h,

with a periodicity of pc in both directions. The thickness, size, and spacing of the structures were set as sweep parameters in COMSOL, to choose the best possible design among different combinations. First, we considered a nanostructure made entirely out of the Ag/TiO_2 cluster-based material described so far.

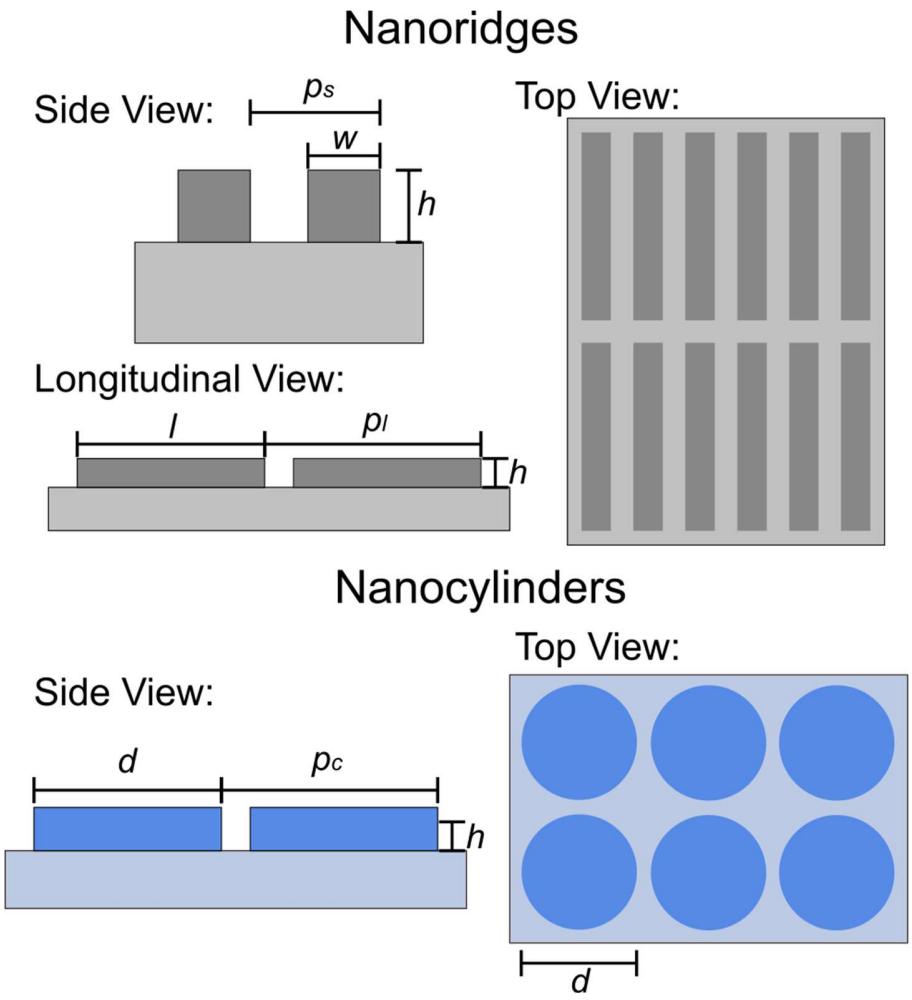

Figure 5.2: Schematic view of the nanoridge and nanocylinders arrays.

To simulate the properties of the Ag/TiO_2 nanocomposite, we defined a custom material within COMSOL using the real and imaginary refractive index obtained from the multilayer optical model simulation in the previous section. The substrate was set to silicon and the surrounding medium was set to water (n=1.33), to reproduce the conditions of a standard fluorescence microscopy setup. Of all the chosen thicknesses (20, 50, 100 nm), the 100 nm thick nanostructures showed an overall better phase tunability compared to the others, and a more pronounced electric field oscillation. For this reason, we chose to fabricate structures with this thickness. It is worth noting, however, that for the COMSOL simulations to be as accurate as possible, one should also repeat the simulation of the dielectric function from Section 5.2 with a 100 nm thick $AgTiO_2$ film, since the optical properties of the material could be different with thickness. The same is true for the 10 nm $AgTiO_2$ top layer described later. This was not possible to do in this work due to time limitations, but should surely be done in future simulations.

Figure 5.3 shows the electric field intensity distribution calculated using COMSOL eigenmode analysis for a 100 nm thick Ag/TiO_2 nanoridge. We can see that the nanostructure exhibits a high field intensity along the top of its surface, which can facilitate the excitation of phenomena within cells and objects placed on top of them. However, a high field intensity is also present at the interface with the substrate, which is not ideal because some of the light is conveyed far from the sample. To investigate the possibility of producing different illumination patterns by altering the phase of the standing wave, we used COMSOL to calculate the electric field magnitude on top of our nanostructures. This time, instead of performing an eigenmode analysis, we set up an incident plane wave with wavelength λ_0 = 458 nm and studied the behavior of the standing wave along the structure as a function of size, separation, and incident angle of the light. Figure 5.3b shows the calculated normalized

electric field on the top of the nanostructures, at a distance of 5 nm from their surface: we can see that the change in phase is roughly 45° for illumination angles ranging from 0° to 8°, or 90° from -8° to 8°, while for most applications a total shift of 4ω/3, or 240°, is required.

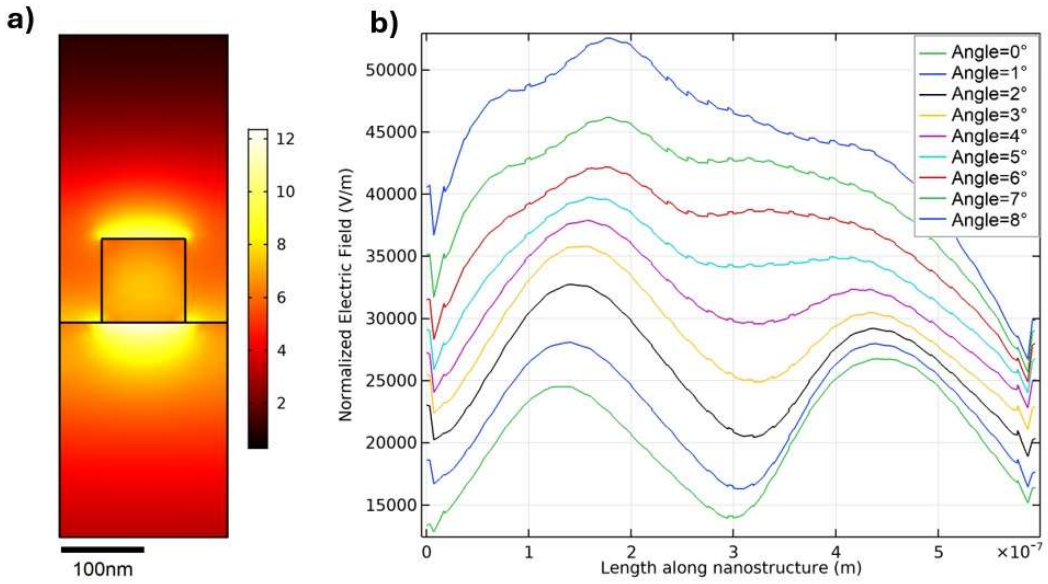

Figure 5.3: a) Calculated electric field mode profile obtained using COMSOL eigenmode analysis, for a 100 nm thick $AgTiO_2$ nanoridge; b) Calculated normalized electric field along the top of a 600 nm nanoantenna $AgTiO_2$ nanoantenna at different incident angles.

Since Ag-only nanoridges show an improved optical mode profile and a better ability to tune the phase of the standing wave pattern compared to an Ag/TiO_2-only nanoridge, we repeated the same simulations with a bilayer nanostructure, composed of a lower layer of Ag and an upper layer of Ag/TiO_2. As shown in Figure 5.4, the intensity of the electric field is mostly localized on the surface of the nanostructure, while the intensity at the interface with

the substrate is significantly lower than in the single-layer $AgTiO_2$ design. Furthermore, as shown in Figure 5.4, the change in phase for this design is more pronounced: in fact, we obtain an almost 180° phase shift for angles ranging from 0° to 8°, or double that amount for angles of -8° to 8°, meeting the requirements for standard SIM.

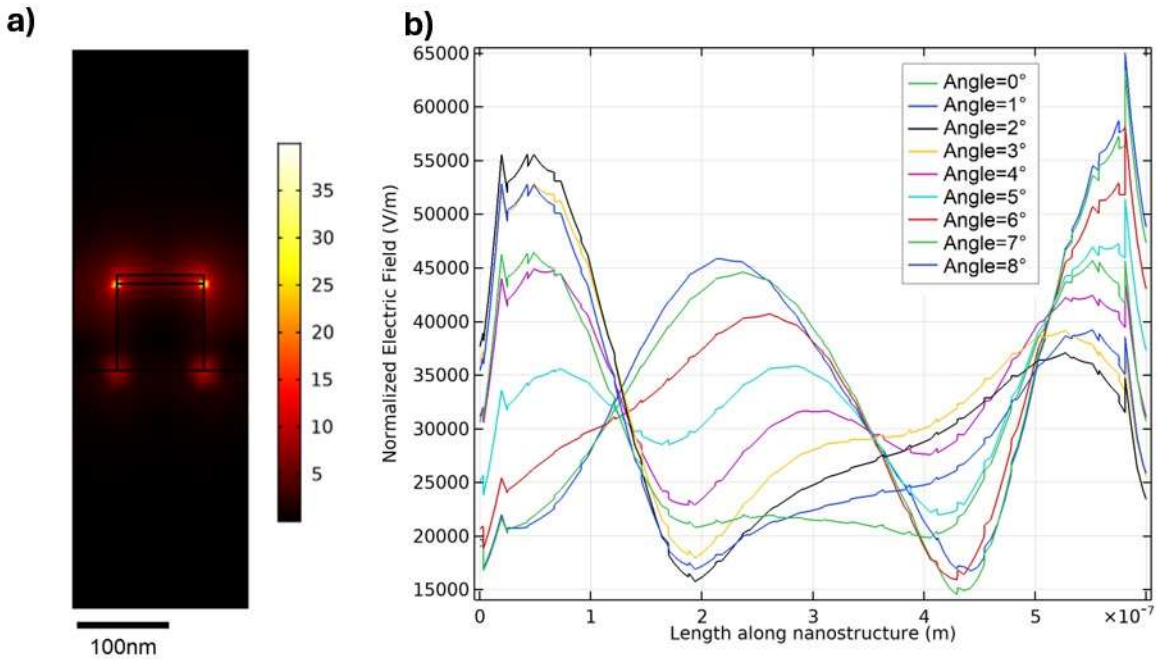

Figure 5.4: a) Calculated electric field mode profile obtained using COMSOL eigenmode analysis, for a 100 nm Ag + 10 nm Ag/TiO_2 nanoridge; b) Calculated normalized electric field along the top of a 600 nm nanoantenna made of 100 nm Ag + 10 nm Ag/TiO_2 at different incident angles.

5.4 Fabrication of the metacrystals

After choosing the most promising designs for nanostructures based on COMSOL simulations, we moved to fabrication. The fabrication method is shown in Figure 5.5: after cleaning the Si substrate with acetone, ethanol, and isopropyl alcohol, a MMA:PMMA electron beam resist bilayer (200 nm MMA + 100 nm PMMA) is deposited by spin-coating on top of the silicon wafer and baking each layer at 190°C. An MMA:PMMA bilayer was chosen over single-layer resist because it has been shown to produce a cleaner liftoff in many cases [180].

After applying the resist, the desired pattern is transferred to the resist by first exposing it with electron-beam lithography (EBL), and developing it with a MIBK:IPA:MEK (1:3:0.1) solution for 40 seconds. To validate the fabrication process and find the best settings for the EBL beam, we performed a dose test by using a simple nanoridge array as a test pattern, exposing the double-layer resist to doses ranging from 500 to 1400 $\mu C/cm^2$ (Figure 5.5a). The pattern consisted of nanoridges with different widths (100 nm and 200 nm), to evaluate the quality of the liftoff and deposition with differently sized structures. After exposing and developing the pattern, deposition of a 100 nm thick Ag/TiO_2 (50-50) film was achieved via SCBD directly on top of the pattern. Liftoff was performed in acetone at room temperature.

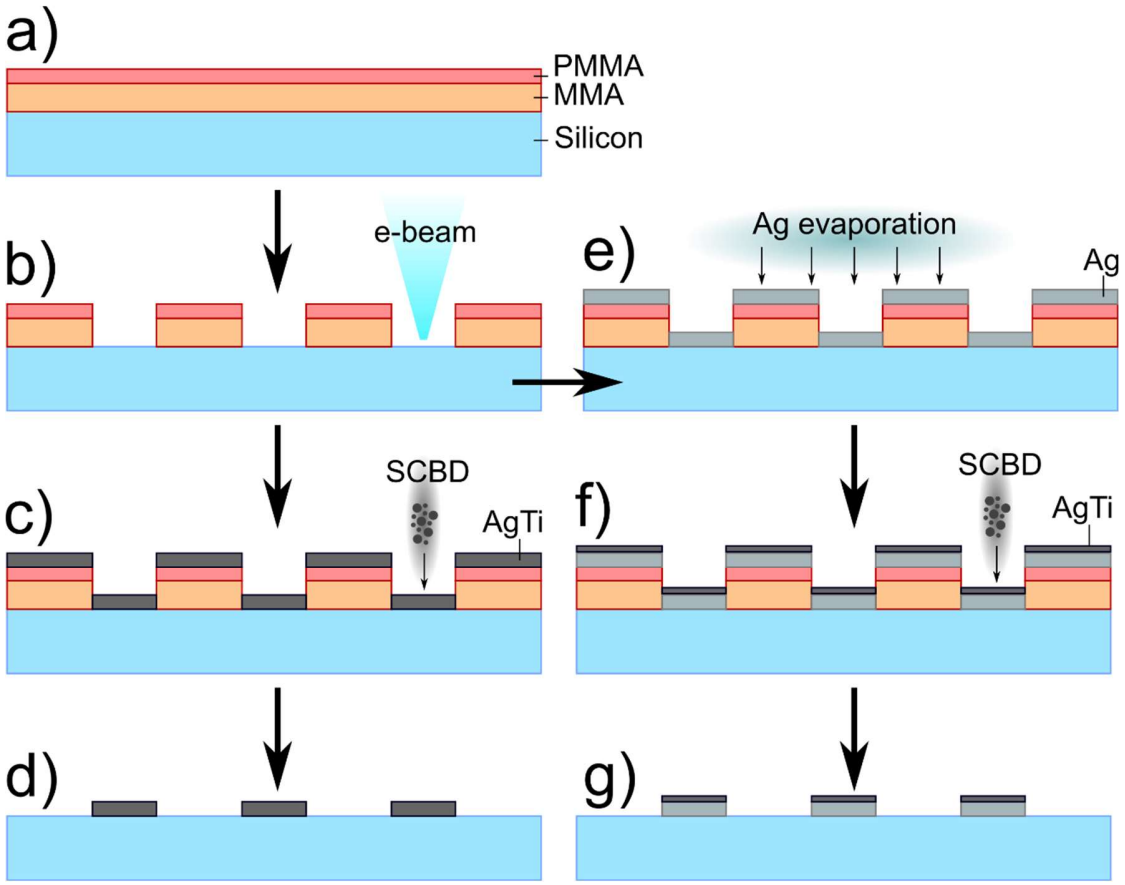

Figure 5.5: Fabrication process of cluster-based nanostructures for SIM. a) Bilayer MMA:PMMA resist spin coating on Si wafer; b) EBL nanopatterning of the resist; c) Supersonic cluster beam deposition of a thick (100 nm) layer of Ag/TiO_2 on top of the resist; d) Liftoff of the resist layer in acetone; e) e-beam evaporation of Ag; Supersonic cluster beam deposition of a thin (10 nm) layer of Ag/TiO2 on top of silver; g) Liftoff of the resist layer in acetone.

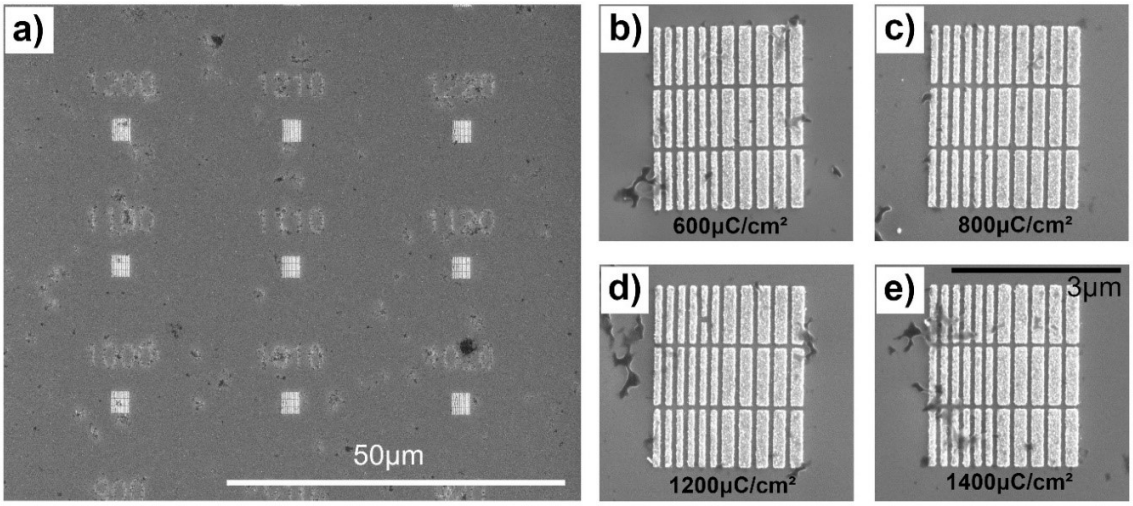

Figure 5.6: a) SEM image of the preliminary nanoridge pattern array for the EBL dose test. The numbers represent the different doses employed in $\mu C/cm^2$. b-e) SEM images of the preliminary nanoridge pattern for the following EBL doses: 600 $\mu C/cm^2$ (b), 800 $\mu C/cm^2$ (c), 1200 $\mu C/cm^2$ (d), 1400 $\mu C/cm^2$ (d).

Figure 5.6b-e shows the results of the preliminary dose test for different e-beam doses: the pattern is well-formed and consistent with the desired design for all doses. Following this information, we settled on 800 $\mu C/cm^2$ for all the following nanofabrication processes. Some of the resist is still present on the surface of the sample (visible as dark spots in Figure 5.6): this is likely due to the "gentle" liftoff process operated with acetone at room temperature.

To the best of our knowledge, this is the first time SCBD is used in conjunction with EBL patterning to produce patterned nanogranular structures, confirming its versatility. It is also worth mentioning that the patterning and liftoff processes were performed at the University of Notre Dame, Indiana, USA, while the SCBD deposition was performed at Università Cattolica del Sacro Cuore, Brescia, Italy.

After the preliminary tests, we chose two different designs for the fabrication of the metacrystals: a nanoridge array with ridge length = 500 nm, width = 100 nm, lateral spacing = 100 nm and longitudinal spacing = 90 nm, and a nanocylinder array with cylinder diameter = 600 nm and spacing = 90 nm. We also chose to fabricate both the single-layer Ag/TiO_2 and the double-layer $Ag + AgTiO_2$ nanostructures used in our COMSOL simulations (see Section 3), to investigate the differences and performance of both designs. After defining the deposition mask using EBL (Fig. 5.5b), the samples undergo different deposition steps depending on the desired outcome: for Ag/TiO_2-only nanostructures, SCBD is used to deposit a 100 nm film on top of the deposition mask (Figure 5.5c); for $Ag+AgTiO_2$ nanostructures, a 100 nm layer of Ag is deposited via e-beam evaporation (Figure 5.5e), then 10 nm of $AgTiO_2$ are deposited via SCBD on top (Figure 5.5f). In both cases, the liftoff is performed by soaking the sample in acetone at room temperature (Figure 5.5d, Figure 5.5g). Figure 5.7 shows an SEM image of the fabricated samples, highlighting how the fabrication process was successfully accomplished for all designs: Figure 5.7a shows the double-layer ($Ag+AgTiO_2$) nanocylinder array pattern; Figure 5.7b shows the single-layer ($AgTiO_2$)

nanocylinders; Figure 5.7c shows the double-layer nanoridge array, and Figure 5.7d shows the single-layer nanoridges.

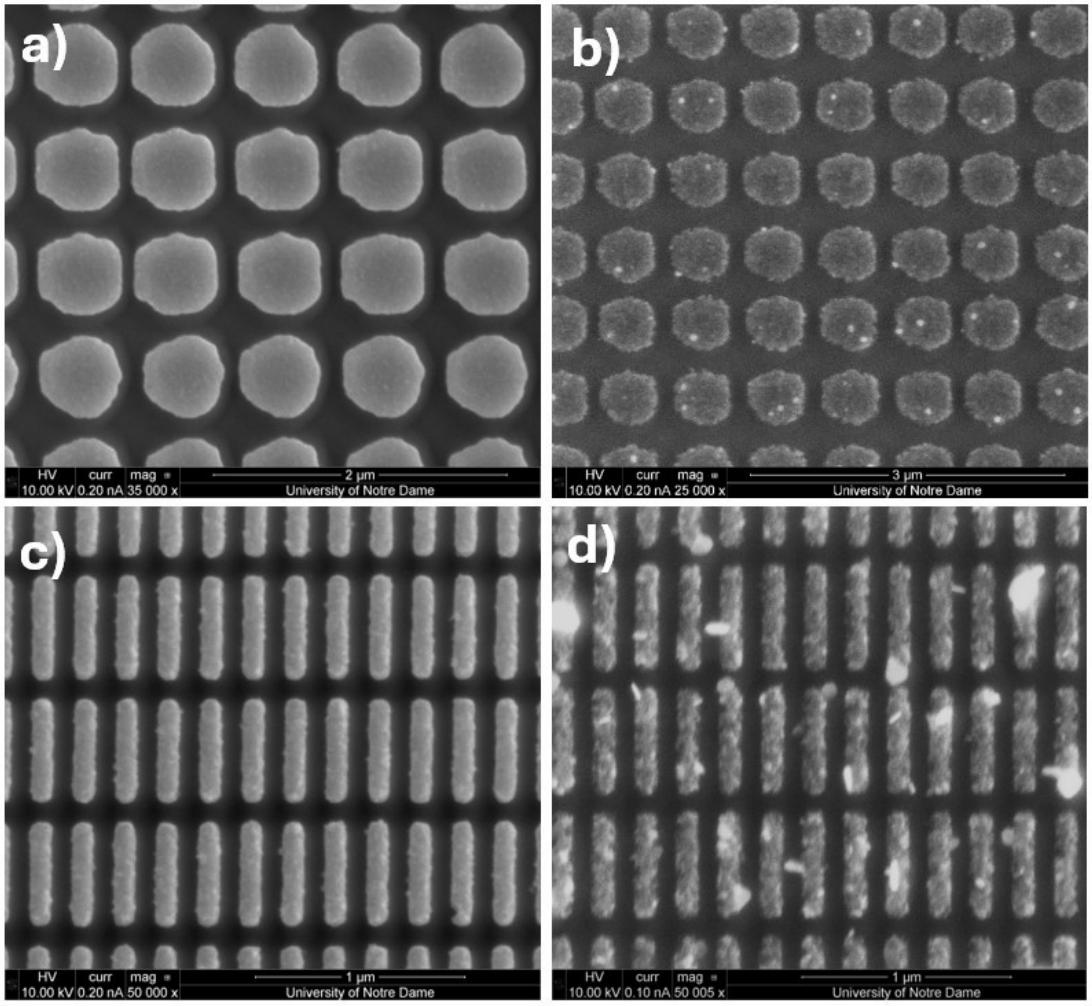

Figure 5.7: a) SEM image of 600 nm wide nanocylinders (100 nm Ag + 15 nm $AgTiO_2$); b) SEM image of 600 nm wide nanocylinders (100 nm $AgTiO_2$); c) SEM image of 100 nm wide, 500 nm long nanoridges (100 nm Ag + 15 nm $AgTiO_2$); d) SEM image of 100 nm wide, 500 nm long nanoridges (100 nm $AgTiO_2$).

5.5 Conclusions

In this chapter, we analyzed the viability of cluster-based Ag/TiO_2 nanostructured materials as substrates for LPSIM. In Section 2, we analyzed the optical properties of the Ag/TiO_2 nanostructured material, which at room temperature is composed of Ag nanoparticles finely dispersed in a TiO_2 matrix. To properly account for the material's porosity and roughness, we employed a two-layer model to calculate the effective complex refractive index of the material. The dielectric function of the Ag/TiO_2 clusters was approximated with a Drude-Lorentz oscillator model, to account for both intraband and interband transitions in both Ag and TiO_2. An effective medium approximation was performed using Bruggeman's formula to account for vacuum inclusions. The proposed model successfully reproduces the optical transmission, absorption and reflection spectra in the visible range, providing a solid base for further analysis.

In Section 3, we investigated the ability of hypothetical nanostructures fabricated using the Ag/TiO_2 nanocomposite material to support optical modes with a variable phase near the surface, which is a key requirement for SIM substrates. To do so, we performed some 2D simulation in COMSOL, calculating the electric field intensity distribution of selected nanostructures. A parameter sweep was performed to find the nanostructures which best suit the requirements of SIM. We performed the COMSOL simulations on both monolayer (100 nm $AgTiO_2$) and bilayer (100 nm Ag + 10 nm Ag/TiO_2) structures. Our analysis showed that the bilayer structure has a greater electric field intensity near the surface of the sample, while also featuring a standing wave with a highly variable phase. Finally, in Section 4, we showed a fabrication method for our substrates based on the creation of an EBL nanopatterned mask, followed by SCBD deposition of the desired material and liftoff. SCBD offers several

advantages over other deposition techniques (i.e. e-beam evaporation) commonly used in the deposition of patterned nanostructures: in particular, it allows the deposition of self-assembled metal nanoparticles supported by a dielectric matrix. The optical and geometrical properties of the supported nanoparticles have been shown to be tuneable over a wide range of possibilities through thermal annealing [49] and exposure to white light.

It is worth mentioning that the proposed fabrication method was only demonstrated with an as-deposited film of the Ag/TiO_2 nanocomposite: here, the supported Ag nanoparticles exhibit the smallest size (~1-2 nm, [52]), which theoretically should provide the best configuration for LPSIM. In fact, smaller, more finely dispersed plasmonic particles will generate a higher frequency (random) illumination pattern, which in turn should result in a higher resolution. To demonstrate the tunability of the substrate, we propose two possible pathways: the first is to simply perform an oven annealing of the fabricated nanopatterned substrates, in a similar way as shown in previous chapters. This should result in the coalescence of Ag particles, leading to a shift in the optical properties of the film and to the generation of a coarser illumination pattern due to the increase in size of the plasmonic particles. Another approach could be to start from an annealed Ag/TiO_2 sample, where the film already has the desired Ag NPs size and distribution: in this case, a selective etching of Ag/TiO_2 can lead to the formation of the desired nanostructured for use in LPSIM. Selective etching of TiO_2 has in fact already been demonstrated for waveguide fabrication, with resolutions as low as 100 nm [181,182]. Since the Ag nanoparticles are supported by the TiO_2 matrix, we expect this method to also work for Ag/TiO_2 nanocomposites.

CHAPTER 6:

CONCLUSIONS AND PERSPECTIVES

6.1 Summary

The goal of this work was to study the effects of post-deposition processing techniques, namely thermal annealing and photothermal heating, on the morphological and optical properties of nanostructured thin films composed of Ag nanocrystals embedded in an amorphous TiO_2 matrix, and evaluate the possible applications of such material. There are many reasons behind the choice of $AgTiO_2$. First, it provides a paradigmatic example of a plasmonic metal-oxide nanocomposite, where the optical properties of the material in the visible range are mainly dictated by the shape and size of the Ag nanocrystals. Furthermore, $AgTiO_2$ nanocomposites are well-studied for their applications in fields such as solar energy conversion and photocatalysis, where there is a strong interest in finding accessible and cost-efficient ways to tailor the optical and structural properties of the material. In this perspective, the choice of supersonic cluster-based synthesis represents a leap in terms of sustainability and deposition rate.

In Chapter 3, we studied the evolution of $AgTiO_2$ nanostructured thin films deposited via SCBD during thermal annealing at high temperatures, focusing on an important and often overlooked aspect of this post-deposition technique, i.e. the substrate. In fact, the properties of the substrate are often neglected when studying the thermal evolution of thin films, likely because there is a lack of a deep understanding of the film-substrate interactions during annealing. By using SCBD, we ensure that we are depositing the same film on different

substrates, since the film properties are determined only by the low-energy ballistic aggregation of clusters. Therefore, we deposited 50 nm-thick $AgTiO_2$ thin films on both silica and sapphire and characterized the evolution of their morphological and optical properties via AFM, Raman spectroscopy, SEM and spectrophotometry. Our findings clearly show that the substrate is able to steer the evolution of the morphological and optical properties of $AgTiO_2$ nanocomposites, especially for annealing temperatures higher than 600°C.

In Chapter 4, we combined conventional oven annealing and photo-induced thermal heating to further affect the properties of $AgTiO_2$ thin films deposited on silica. A 175W Xenon white light lamp was chosen as the illumination source, since the absorption band of Ag/TiO_2 nanocomposites is quite broad. Also, this type of lamp is more commonly available and allows the illumination of larger sample areas compared to monochromatic laser sources. In samples annealed at 600-700°C, photothermal heating produced a drastic change in the optical absorption spectrum, caused by the surfacing of the Ag nanoparticles on top of the sample. In both Chapter 3 and Chapter 4, we were able to drastically affect the size, shape and distribution of the silver nanoparticles inside the TiO_2 matrix, which are responsible for the visible absorption band of the material. Our results show the viability of post-deposition techniques as effective tools to functionalize $AgTiO_2$ plasmonic nanocomposites for different applications.

Finally, in Chapter 5, we explored the viability of cluster-based $AgTiO_2$ materials as substrates for LPSIM. First, we employed a bilayer effective medium approximation to determine the complex index of refraction of our material. Then, we used COMSOL to simulate the response of the excited electric field in selected nanostructures to ensure that they support standing waves with a high field intensity near the top of the nanostructure, as required

by SIM. Finally, we successfully fabricated some samples based on our designs by combining SCBD and EBL to produce cluster-based metacrystals.

6.2 Future work and perspectives

Our findings and results open new and exciting perspectives in the development and study of novel plasmonic nanocomposite materials. However, many unknowns and open issues remain regarding the post-deposition tuning of plasmonic nanocomposites. First of all, as we highlighted already in Chapter 3, all of our analyses focused on the study of materials composed of 50% wt. silver and 50% wt. titanium. Despite this limitation, we were able to tune the properties of the materials over a relatively wide range of possibilities by employing techniques such as thermal annealing and photothermal heating. However, it is certain that the initial distribution of silver and titanium can play an extremely important role in the evolution of these materials during annealing. Therefore, to further enhance the functionalization of these materials, it would be very interesting to repeat the measurements with different initial material concentrations.

Speaking of the actual tuning of the properties of $AgTiO_2$ nanomaterials, we have to underline two important results we obtained through post-deposition techniques, which could have interesting implications. The first one is the broadband absorption feature we achieved in Chapter 3 and Chapter 4 after annealing the 50 nm $AgTiO_2$ thin film at 600°C. As explained in Chapter 4, this feature is likely due to the formation of deep interconnected structures following the diffusion of silver inside the TiO_2 matrix. We mentioned how plasmonic broadband absorbers are of great interest in applications such as solar energy conversion and photocatalysis, due to their ability to harvest light from the entire visible spectrum. In this

perspective, our approach to the tuning of plasmonic thin films could represent a simple and efficient way to produce self-assembled plasmonic absorbers. For this reason, it would be extremely interesting to test the performance of these materials by comparing them with existing structures, as long as they can withstand the annealing process. For example, TiO_2 is already a widely used material in solar cells, and the presence of a broadband absorber could easily enhance its performance due to charge transfer effects. The implementation of $AgTiO_2$ thin films in photocatalytic would be an even more straightforward process, as annealing is already used to improve the properties of the electrodes.

The second important result is represented by the surfacing of Ag nanoparticles in samples annealed at 600-700°C after being exposed to white light. The ability to control the distribution of the nanoparticles, as well as their size, is a very interesting result, which probably arises from the difference between the local photothermal heating of plasmonic nanoparticles (generated by the enhancement of the electric field in the proximity of the particle) and the widespread heating induced by conventional heating. This manipulation of embedded Ag nanocrystals could be extremely useful in the fabrication of SERS substrates, where having a large quantity of plasmonic nanoparticles near the surface of the sample leads to better enhancements of the Raman signal.

Another aspect worthy of attention is the substrate-dependent evolution of our thin films: following our observations, it is clear that the role of substrate could represent a key factor for an effective tuning of the properties of plasmonic nanocomposites during thermal annealing. Despite our hypotheses on the interplay between film and substrate during the annealing of $AgTiO_2$ thin films, many questions remain on how the substrate impacts the properties of the film. To shine light on this phenomenon, one could systematically investigate the film-substrate interactions during annealing by depositing the same film on different

substrate and studying the thermodynamic, chemical and physical exchanges between the two layers, for example through cross-sectional TEM analysis. This approach could surely lead to a better understanding of the complex phenomena behind thermal annealing, as well as to better designs for tunable plasmonic nanostructures.

In the study of TiO_2 crystallization in Chapter 3, we also observed how our samples behaved differently from TiO_2-only thin films deposited with the same technique. In fact, TiO_2 in our samples remains amorphous for annealing temperatures up to 600°C, and shows coexistence of both anatase and rutile for temperatures higher than 600°C. We attributed this phenomenon to the Zener pinning pressure exerted by the finely dispersed Ag nanoparticles on the grain boundaries of TiO_2. The Zener pinning, which is a well-known phenomenon in metallurgy, is a noteworthy phenomenon when applied to nanostructured materials, as it could be intentionally exploited to enhance the thermal resistance properties of thin films or in cases where it is necessary to prevent or delay the crystallization of a material. For example, it might be interesting to use the cluster source to attempt the deposition of thin films composed of a large number of elements (four or five). If the materials are finely dispersed within the clusters, as observed in our $AgTiO_2$, these materials could exhibit very high thermal resistance properties due to the large number of interfaces, which increase the potential barrier required for melting.

Finally, we have shown how SCBD can be used in conjunction with EBL to produce cluster-based nanopatterned substrates for different applications. In Chapter 5, we have investigated how our $AgTiO_2$ nanocomposites could be used as efficient substrates for LPSIM. However, there is still much work to be done to achieve an actual implementation of those materials in a LPSIM setup. First, we must prove that we can couple light into an optical mode on the surface of the sample. This can be done qualitatively, by characterizing the samples via

spectroscopic ellipsometry: in fact, the presence of optical modes is usually reflected in the angle-dependent reflectivity spectrum of a sample in the form of sharp dips or phase changes in Ψ/Δ. If those features shift consistently with the wavelength/angle, they could indicate the presence of one or more optical modes forming a mode dispersion curve. After identifying the excited optical modes, one could then proceed with testing the substrate using benchmark samples. At this stage, it is necessary to determine whether the embedded Ag nanocrystals are capable of providing a set of illumination patterns of sufficient quality for the image reconstruction algorithm, or if additional fabrication steps are required. Undoubtedly, the ability to tune the plasmon resonance of the embedded nanocrystal is an invaluable tool for the development of better substrates for LPSIM.

BIBLIOGRAPHY

1. West, P.R.; Ishii, S.; Naik, G.V.; Emani, N.K.; Shalaev, V.M.; Boltasseva, A. Searching for Better Plasmonic Materials. *Laser & Photonics Reviews* **2010**, *4*, 795–808, doi:10.1002/lpor.200900055.

2. Faucheaux, J.A.; Stanton, A.L.D.; Jain, P.K. Plasmon Resonances of Semiconductor Nanocrystals: Physical Principles and New Opportunities. *J. Phys. Chem. Lett.* **2014**, *5*, 976–985, doi:10.1021/jz500037k.

3. Guo, Q.; Li, C.; Deng, B.; Yuan, S.; Guinea, F.; Xia, F. Infrared Nanophotonics Based on Graphene Plasmonics. *ACS Photonics* **2017**, *4*, 2989–2999, doi:10.1021/acsphotonics.7b00547.

4. Bontempi, N.; Cavaliere, E.; Cappello, V.; Pingue, P.; Gavioli, L. Ag@TiO $_2$ Nanogranular Films by Gas Phase Synthesis as Hybrid SERS Platforms. *Phys. Chem. Chem. Phys.* **2019**, *21*, 25090–25097, doi:10.1039/C9CP03998H.

5. Langer, J.; Jimenez De Aberasturi, D.; Aizpurua, J.; Alvarez-Puebla, R.A.; Auguié, B.; Baumberg, J.J.; Bazan, G.C.; Bell, S.E.J.; Boisen, A.; Brolo, A.G.; et al. Present and Future of Surface-Enhanced Raman Scattering. *ACS Nano* **2020**, *14*, 28–117, doi:10.1021/acsnano.9b04224.

6. Zhang, Z.; Zhang, C.; Zheng, H.; Xu, H. Plasmon-Driven Catalysis on Molecules and Nanomaterials. *Acc. Chem. Res.* **2019**, *52*, 2506–2515, doi:10.1021/acs.accounts.9b00224.

7. Manuel, A.; Shankar, K. Hot Electrons in TiO2–Noble Metal Nano-Heterojunctions: Fundamental Science and Applications in Photocatalysis. *Nanomaterials* **2021**, *11*, 1249, doi:10.3390/nano11051249.

8. Zhou, N.; López-Puente, V.; Wang, Q.; Polavarapu, L.; Pastoriza-Santos, I.; Xu, Q.-H. Plasmon-Enhanced Light Harvesting: Applications in Enhanced Photocatalysis, Photodynamic Therapy and Photovoltaics. *RSC Adv.* **2015**, *5*, 29076–29097, doi:10.1039/C5RA01819F.

9. Jain, P.K.; Huang, X.; El-Sayed, I.H.; El-Sayed, M.A. Noble Metals on the Nanoscale: Optical and Photothermal Properties and Some Applications in Imaging, Sensing, Biology, and Medicine. *Acc. Chem. Res.* **2008**, *41*, 1578–1586, doi:10.1021/ar7002804.

10. Goldys; Drozdowicz-Tomsi, K. Gold and Silver Nanowires for Fluorescence Enhancement. In *Nanowires - Fundamental Research*; Hashim, A., Ed.; InTech, 2011 ISBN 978-953-307-327-9.

11. Li, J.-F.; Li, C.-Y.; Aroca, R.F. Plasmon-Enhanced Fluorescence Spectroscopy. *Chem. Soc. Rev.* **2017**, *46*, 3962–3979, doi:10.1039/C7CS00169J.

12. Su, Q.; Jiang, C.; Gou, D.; Long, Y. Surface Plasmon-Assisted Fluorescence Enhancing and Quenching: From Theory to Application. *ACS Appl. Bio Mater.* **2021**, *4*, 4684–4705, doi:10.1021/acsabm.1c00320.

13. Dasgupta, S.; Ray, K. Plasmon-Enhanced Fluorescence for Biophotonics and Bio-Analytical Applications. *Front. Chem.* **2024**, *12*, 1407561, doi:10.3389/fchem.2024.1407561.

14. Maier, S.A. *Plasmonics: Fundamentals and Applications*; Springer: New York, 2007; ISBN 978-0-387-33150-8.

15. Otto, A. Excitation of Nonradiative Surface Plasma Waves in Silver by the Method of Frustrated Total Reflection. *Z. Physik* **1968**, *216*, 398–410, doi:10.1007/BF01391532.

16. Kretschmann, E.; Raether, H. Notizen: Radiative Decay of Non Radiative Surface Plasmons Excited by Light. *Zeitschrift für Naturforschung A* **1968**, *23*, 2135–2136, doi:10.1515/zna-1968-1247.

17. Prabowo, B.; Purwidyantri, A.; Liu, K.-C. Surface Plasmon Resonance Optical Sensor: A Review on Light Source Technology. *Biosensors* **2018**, *8*, 80, doi:10.3390/bios8030080.

18. Wiley, B.J.; Im, S.H.; Li, Z.-Y.; McLellan, J.; Siekkinen, A.; Xia, Y. Maneuvering the Surface Plasmon Resonance of Silver Nanostructures through Shape-Controlled Synthesis. *J. Phys. Chem. B* **2006**, *110*, 15666–15675, doi:10.1021/jp0608628.

19. Grzelczak, M.; Pérez-Juste, J.; Mulvaney, P.; Liz-Marzán, L.M. Shape Control in Gold Nanoparticle Synthesis. *Chem. Soc. Rev.* **2008**, *37*, 1783, doi:10.1039/b711490g.

20. Gao, P.; Pu, M.; Ma, X.; Li, X.; Guo, Y.; Wang, C.; Zhao, Z.; Luo, X. Plasmonic Lithography for the Fabrication of Surface Nanostructures with a Feature Size down to 9 Nm. *Nanoscale* **2020**, *12*, 2415–2421, doi:10.1039/C9NR08153D.

21. Mock, J.J.; Barbic, M.; Smith, D.R.; Schultz, D.A.; Schultz, S. Shape Effects in Plasmon Resonance of Individual Colloidal Silver Nanoparticles. *The Journal of Chemical Physics* **2002**, *116*, 6755–6759, doi:10.1063/1.1462610.

22. Calvo, R.; Thon, A.; Saad, A.; Salvador-Matar, A.; Manso-Silván, M.; Ahumada, Ó.; Pini, V. Size Characterization of Plasmonic Nanoparticles with Dark-Field Single Particle Spectrophotometry. *Sci Rep* **2022**, *12*, 17231, doi:10.1038/s41598-022-21649-8.

23. Vayssilov, G.N.; Lykhach, Y.; Migani, A.; Staudt, T.; Petrova, G.P.; Tsud, N.; Skála, T.; Bruix, A.; Illas, F.; Prince, K.C.; et al. Support Nanostructure Boosts Oxygen

Transfer to Catalytically Active Platinum Nanoparticles. *Nature Mater* **2011**, *10*, 310–315, doi:10.1038/nmat2976.

24. Liu, L.; Corma, A. Metal Catalysts for Heterogeneous Catalysis: From Single Atoms to Nanoclusters and Nanoparticles. *Chem. Rev.* **2018**, *118*, 4981–5079, doi:10.1021/acs.chemrev.7b00776.

25. Atwater, H.A.; Polman, A. Plasmonics for Improved Photovoltaic Devices. *Nature Mater* **2010**, *9*, 205–213, doi:10.1038/nmat2629.

26. Rodrigues, M.S.; Costa, D.; Domingues, R.P.; Apreutesei, M.; Pedrosa, P.; Martin, N.; Correlo, V.M.; Reis, R.L.; Alves, E.; Barradas, N.P.; et al. Optimization of Nanocomposite Au/TiO 2 Thin Films towards LSPR Optical-Sensing. *Applied Surface Science* **2018**, *438*, 74–83, doi:10.1016/j.apsusc.2017.09.162.

27. Huet, K.; Mazzamuto, F.; Tabata, T.; Toqué-Tresonne, I.; Mori, Y. Doping of Semiconductor Devices by Laser Thermal Annealing. *Materials Science in Semiconductor Processing* **2017**, *62*, 92–102, doi:10.1016/j.mssp.2016.11.008.

28. Fu, J.; Shang, H.; Li, Z.; Wang, W.; Chen, D. Thermal Annealing Effects on the Stress Stability in Silicon Dioxide Films Grown by Plasma-Enhanced Chemical Vapor Deposition. *Microsyst Technol* **2017**, *23*, 2753–2757, doi:10.1007/s00542-016-3005-1.

29. Pyo, J.; Ryu, H.Y.; Park, J.; Lee, M.; Ryu, H.-Y. Laser-Power Dependence of Poly-Silicon Crystallization Using 355-Nm Nanosecond Laser Annealing. *J. Korean Phys. Soc.* **2020**, *76*, 1116–1120, doi:10.3938/jkps.76.1116.

30. Singh, J.; Sahu, K.; Mohapatra, S. Thermal Annealing Induced Evolution of Morphological, Structural, Optical and Photocatalytic Properties of Ag-TiO2 Nanocomposite Thin Films. *Journal of Physics and Chemistry of Solids* **2019**, *129*, 317–323, doi:10.1016/j.jpcs.2019.01.034.

31. Chen, B.; Mokume, M.; Liu, C.; Hayashi, K. Structure and Localized Surface Plasmon Tuning of Sputtered Au Nano-Islands through Thermal Annealing. *Vacuum* **2014**, *110*, 94–101, doi:10.1016/j.vacuum.2014.09.005.

32. Mosquera, A.A.; Albella, J.M.; Navarro, V.; Bhattacharyya, D.; Endrino, J.L. Effect of Silver on the Phase Transition and Wettability of Titanium Oxide Films. *Sci Rep* **2016**, *6*, 32171, doi:10.1038/srep32171.

33. Torrell, M.; Kabir, R.; Cunha, L.; Vasilevskiy, M.I.; Vaz, F.; Cavaleiro, A.; Alves, E.; Barradas, N.P. Tuning of the Surface Plasmon Resonance in TiO2/Au Thin Films Grown by Magnetron Sputtering: The Effect of Thermal Annealing. *Journal of Applied Physics* **2011**, *109*, 074310, doi:10.1063/1.3565066.

34. Zhang, H.; Wang, G.; Chen, D.; Lv, X.; Li, J. Tuning Photoelectrochemical Performances of Ag−TiO $_2$ Nanocomposites via Reduction/Oxidation of Ag. *Chem. Mater.* **2008**, *20*, 6543–6549, doi:10.1021/cm801796q.

35. Lin, C.-P.; Chen, H.; Nakaruk, A.; Koshy, P.; Sorrell, C.C. Effect of Annealing Temperature on the Photocatalytic Activity of TiO2 Thin Films. *Energy Procedia* **2013**, *34*, 627–636, doi:10.1016/j.egypro.2013.06.794.

36. Huang, Q.J.; Li, X.Q.; Yao, J.L.; Ren, B.; Cai, W.B.; Gao, J.S.; Mao, B.W.; Tian, Z.Q. Extending Surface Raman Spectroscopic Studies to Transition Metals for Practical Applications. *Surface Science* **1999**, *427–428*, 162–166, doi:10.1016/S0039-6028(99)00258-7.

37. Fang, S.-U.; Hsu, C.-L.; Hsu, T.-C.; Juang, M.-Y.; Liu, Y.-C. Surface Roughness-Correlated SERS Effect on Au Island-Deposited Substrate. *Journal of Electroanalytical Chemistry* **2015**, *741*, 127–133, doi:10.1016/j.jelechem.2015.01.028.

38. Huygens, C. *Traité de La Lumière : Où Sont Expliquées Les Causes de Ce Qui Lui Arrive Dans La Reflexion, & Dans La Refraction et Particulièrement Dans l'étrange Réfraction Du Cristal d'Islande*; Chez Pierre vander Aa, marchand libraire: A Leide, 1690;

39. Magidson, V.; Khodjakov, A. Circumventing Photodamage in Live-Cell Microscopy. In *Methods in Cell Biology*; Elsevier, 2013; Vol. 114, pp. 545–560 ISBN 978-0-12-407761-4.

40. Erni, R.; Rossell, M.D.; Kisielowski, C.; Dahmen, U. Atomic-Resolution Imaging with a Sub-50-Pm Electron Probe. *Phys. Rev. Lett.* **2009**, *102*, 096101, doi:10.1103/PhysRevLett.102.096101.

41. Hell, S.W.; Wichmann, J. Breaking the Diffraction Resolution Limit by Stimulated Emission: Stimulated-Emission-Depletion Fluorescence Microscopy. *Opt. Lett.* **1994**, *19*, 780, doi:10.1364/OL.19.000780.

42. Betzig, E.; Patterson, G.H.; Sougrat, R.; Lindwasser, O.W.; Olenych, S.; Bonifacino, J.S.; Davidson, M.W.; Lippincott-Schwartz, J.; Hess, H.F. Imaging Intracellular Fluorescent Proteins at Nanometer Resolution. *Science* **2006**, *313*, 1642–1645, doi:10.1126/science.1127344.

43. Hess, S.T.; Girirajan, T.P.K.; Mason, M.D. Ultra-High Resolution Imaging by Fluorescence Photoactivation Localization Microscopy. *Biophysical Journal* **2006**, *91*, 4258–4272, doi:10.1529/biophysj.106.091116.

44. Bates, M.; Huang, B.; Dempsey, G.T.; Zhuang, X. Multicolor Super-Resolution Imaging with Photo-Switchable Fluorescent Probes. *Science* **2007**, *317*, 1749–1753, doi:10.1126/science.1146598.

45. Gustafsson, M.G.L. Surpassing the Lateral Resolution Limit by a Factor of Two Using Structured Illumination Microscopy: SHORT COMMUNICATION. *Journal of Microscopy* **2000**, *198*, 82–87, doi:10.1046/j.1365-2818.2000.00710.x.

46. Ponsetto, J.L.; Wei, F.; Liu, Z. Localized Plasmon Assisted Structured Illumination Microscopy for Wide-Field High-Speed Dispersion-Independent Super Resolution Imaging. *Nanoscale* **2014**, *6*, 5807–5812, doi:10.1039/C4NR00443D.

47. Mudry, E.; Belkebir, K.; Girard, J.; Savatier, J.; Le Moal, E.; Nicoletti, C.; Allain, M.; Sentenac, A. Structured Illumination Microscopy Using Unknown Speckle Patterns. *Nature Photon* **2012**, *6*, 312–315, doi:10.1038/nphoton.2012.83.

48. Guan, Y.; Masui, S.; Kadoya, S.; Michihata, M.; Takahashi, S. Super-Resolution by Localized Plasmonic Structured Illumination Microscopy Using Self-Assembled Nanoparticle Substrates. *Nanomanuf Metrol* **2024**, *7*, 14, doi:10.1007/s41871-024-00233-w.

49. Balzano, V.; Cavaliere, E.; Fanetti, M.; Gardonio, S.; Gavioli, L. The Role of Substrate on Thermal Evolution of Ag/TiO2 Nanogranular Thin Films. *Nanomaterials* **2021**, *11*, 2253, doi:10.3390/nano11092253.

50. Milani, P.; Iannotta, S. *Cluster Beam Synthesis of Nanostructured Materials*; 1999; ISBN 978-3-642-64173-2.

51. Benetti, G.; Cavaliere, E.; Canteri, A.; Landini, G.; Rossolini, G.M.; Pallecchi, L.; Chiodi, M.; Van Bael, M.J.; Winckelmans, N.; Bals, S.; et al. Direct Synthesis of Antimicrobial Coatings Based on Tailored Bi-Elemental Nanoparticles. *APL Materials* **2017**, *5*, 036105, doi:10.1063/1.4978772.

52. Cavaliere, E.; Benetti, G.; Van Bael, M.; Winckelmans, N.; Bals, S.; Gavioli, L. Exploring the Optical and Morphological Properties of Ag and Ag/TiO2 Nanocomposites Grown by Supersonic Cluster Beam Deposition. *Nanomaterials* **2017**, *7*, 442, doi:10.3390/nano7120442.

53. Sun, W.; Tan, A.W.-Y.; Wu, K.; Yin, S.; Yang, X.; Marinescu, I.; Liu, E. Post-Process Treatments on Supersonic Cold Sprayed Coatings: A Review. *Coatings* **2020**, *10*, 123, doi:10.3390/coatings10020123.

54. Shao, F.; Wan, Q. Recent Progress on Jet Printing of Oxide-Based Thin Film Transistors. *J. Phys. D: Appl. Phys.* **2019**, *52*, 143002, doi:10.1088/1361-6463/aafd79.

55. Benetti, G.; Cavaliere, E.; Brescia, R.; Salassi, S.; Ferrando, R.; Vantomme, A.; Pallecchi, L.; Pollini, S.; Boncompagni, S.; Fortuni, B.; et al. Tailored Ag–Cu–Mg Multielemental Nanoparticles for Wide-Spectrum Antibacterial Coating. *Nanoscale* **2019**, *11*, 1626–1635, doi:10.1039/C8NR08375D.

56. García-Serrano, J.; Gómez-Hernández, E.; Ocampo-Fernández, M.; Pal, U. Effect of Ag Doping on the Crystallization and Phase Transition of TiO2 Nanoparticles. *Current Applied Physics* **2009**, *9*, 1097–1105, doi:10.1016/j.cap.2008.12.008.

57. Mathpal, M.C.; Tripathi, A.K.; Singh, M.K.; Gairola, S.P.; Pandey, S.N.; Agarwal, A. Effect of Annealing Temperature on Raman Spectra of TiO2 Nanoparticles. *Chemical Physics Letters* **2013**, *555*, 182–186, doi:10.1016/j.cplett.2012.10.082.

58. Adochite, R.C.; Munteanu, D.; Torrell, M.; Cunha, L.; Alves, E.; Barradas, N.P.; Cavaleiro, A.; Riviere, J.P.; Le Bourhis, E.; Eyidi, D.; et al. The Influence of Annealing Treatments on the Properties of Ag:TiO2 Nanocomposite Films Prepared by Magnetron Sputtering. *Applied Surface Science* **2012**, *258*, 4028–4034, doi:10.1016/j.apsusc.2011.12.095.

59. Bukauskas, V.; Kaciulis, S.; Mezzi, A.; Mironas, A.; Niaura, G.; Rudzikas, M.; Šimkienė, I.; Šetkus, A. Effect of Substrate Temperature on the Arrangement of Ultra-Thin TiO2 Films Grown by a Dc-Magnetron Sputtering Deposition. *Thin Solid Films* **2015**, *585*, 5–12, doi:10.1016/j.tsf.2015.04.007.

60. Kulczyk-Malecka, J.; Kelly, P.J.; West, G.; Clarke, G.C.B.; Ridealgh, J.A.; Almtoft, K.P.; Greer, A.L.; Barber, Z.H. Investigation of Silver Diffusion in TiO2/Ag/TiO2 Coatings. *Acta Materialia* **2014**, *66*, 396–404, doi:10.1016/j.actamat.2013.11.030.

61. Herrmann, J.; Tahiri, H.; Aitichou, Y.; Lassaletta, G.; Gonzalezelipe, A.; Fernandez, A. Characterization and Photocatalytic Activity in Aqueous Medium of TiO2 and Ag-TiO2 Coatings on Quartz. *Applied Catalysis B: Environmental* **1997**, *13*, 219–228, doi:10.1016/S0926-3373(96)00107-5.

62. Jana, S.; Bera, P.; Chakraborty, B.; Mitra, B.C.; Mondal, A. Impact of Annealing on the Electrodeposited WS2 Thin Films: Enhanced Photodegradation of Coupled Semiconductor. *Applied Surface Science* **2014**, *317*, 154–159, doi:10.1016/j.apsusc.2014.07.151.

63. Tsay, C.-Y.; Huang, T.-T. Improvement of Physical Properties of IGZO Thin Films Prepared by Excimer Laser Annealing of Sol–Gel Derived Precursor Films. *Materials Chemistry and Physics* **2013**, *140*, 365–372, doi:10.1016/j.matchemphys.2013.03.051.

64. Barborini, E.; Kholmanov, I.N.; Piseri, P.; Ducati, C.; Bottani, C.E.; Milani, P. Engineering the Nanocrystalline Structure of TiO2 Films by Aerodynamically Filtered Cluster Deposition. *Appl. Phys. Lett.* **2002**, *81*, 3052–3054, doi:10.1063/1.1510579.

65. Kholmanov, I.N.; Barborini, E.; Vinati, S.; Piseri, P.; Podestà, A.; Ducati, C.; Lenardi, C.; Milani, P. The Influence of the Precursor Clusters on the Structural and Morphological Evolution of Nanostructured TiO $_2$ under Thermal Annealing. *Nanotechnology* **2003**, *14*, 1168–1173, doi:10.1088/0957-4484/14/11/002.

66. Cavaliere, E.; Benetti, G.; Banfi, F.; Gavioli, L. Antimicrobial Nanostructured Coating. In *Frontiers of Nanoscience*; Elsevier, 2020; Vol. 15, pp. 291–311 ISBN 978-0-08-102515-4.

67. Sanzone, G.; Zimbone, M.; Cacciato, G.; Ruffino, F.; Carles, R.; Privitera, V.; Grimaldi, M.G. Ag/TiO2 Nanocomposite for Visible Light-Driven Photocatalysis. *Superlattices and Microstructures* **2018**, *123*, 394–402, doi:10.1016/j.spmi.2018.09.028.

68. Yang, J.-K.; Davis, A.P. Photocatalytic Oxidation of Cu(II)−EDTA with Illuminated TiO_2: Kinetics. *Environ. Sci. Technol.* **2000**, *34*, 3789–3795, doi:10.1021/es990874p.

69. Anpo, M.; Takeuchi, M. The Design and Development of Highly Reactive Titanium Oxide Photocatalysts Operating under Visible Light Irradiation. *Journal of Catalysis* **2003**, *216*, 505–516, doi:10.1016/S0021-9517(02)00104-5.

70. Fraters, B.D.; Cavaliere, E.; Mul, G.; Gavioli, L. Synthesis of Photocatalytic TiO2 Nano-Coatings by Supersonic Cluster Beam Deposition. *Journal of Alloys and Compounds* **2014**, *615*, S467–S471, doi:10.1016/j.jallcom.2013.12.037.

71. Hayakawa, I.; Iwamoto, Y.; Kikuta, K.; Hirano, S. Gas Sensing Properties of Platinum Dispersed-TiO2 Thin Film Derived from Precursor. *Sensors and Actuators B: Chemical* **2000**, *62*, 55–60, doi:10.1016/S0925-4005(99)00303-2.

72. Zhu, Z.; Kao, C.-T.; Wu, R.-J. A Highly Sensitive Ethanol Sensor Based on Ag@TiO 2 Nanoparticles at Room Temperature. *Applied Surface Science* **2014**, *320*, 348–355, doi:10.1016/j.apsusc.2014.09.108.

73. Zhu, Y.; Shi, J.; Zhang, Z.; Zhang, C.; Zhang, X. Development of a Gas Sensor Utilizing Chemiluminescence on Nanosized Titanium Dioxide. *Anal. Chem.* **2002**, *74*, 120–124, doi:10.1021/ac010450p.

74. Tanahashi, I.; Yamazaki, F.; Hamada, K. Localized Surface Plasmon Resonance Sensing Properties of Ag/TiO_2 Films. *Chem. Lett.* **2006**, *35*, 454–455, doi:10.1246/cl.2006.454.

75. Bach, U.; Lupo, D.; Comte, P.; Moser, J.E.; Weissörtel, F.; Salbeck, J.; Spreitzer, H.; Grätzel, M. Solid-State Dye-Sensitized Mesoporous TiO2 Solar Cells with High Photon-to-Electron Conversion Efficiencies. *Nature* **1998**, *395*, 583–585, doi:10.1038/26936.

76. Kawamura, G.; Ohmi, H.; Tan, W.K.; Lockman, Z.; Muto, H.; Matsuda, A. Ag Nanoparticle-Deposited TiO2 Nanotube Arrays for Electrodes of Dye-Sensitized Solar Cells. *Nanoscale Res Lett* **2015**, *10*, 219, doi:10.1186/s11671-015-0924-1.

77. Wang, J.; Polleux, J.; Lim, J.; Dunn, B. Pseudocapacitive Contributions to Electrochemical Energy Storage in TiO_2 (Anatase) Nanoparticles. *J. Phys. Chem. C* **2007**, *111*, 14925–14931, doi:10.1021/jp074464w.

78. Nes, E.; Ryum, N.; Hunderi, O. On the Zener Drag. *Acta Metallurgica* **1985**, *33*, 11–22, doi:10.1016/0001-6160(85)90214-7.

79. Andrievski, R.A. Review of Thermal Stability of Nanomaterials. *J Mater Sci* **2014**, *49*, 1449–1460, doi:10.1007/s10853-013-7836-1.

80. O'Dell, L.A.; Savin; Chadwick, A.V.; Smith, M.E. Structural Characterization of SiO_2 and Al_2O_3 Zener-Pinned Nanocrystalline TiO_2 by NMR, XRD and Electron Microscopy. *J. Phys. Chem. C* **2007**, *111*, 13740–13746, doi:10.1021/jp0739871.

81. Viana, M.M.; Mohallem, N.D.S.; Miquita, D.R.; Balzuweit, K.; Silva-Pinto, E. Preparation of Amorphous and Crystalline Ag/TiO2 Nanocomposite Thin Films. *Applied Surface Science* **2013**, *265*, 130–136, doi:10.1016/j.apsusc.2012.10.151.

82. Chuang, H.-Y.; Chen, D.-H. Fabrication and Photoelectrochemical Study of Ag@TiO2 Nanoparticle Thin Film Electrode. *International Journal of Hydrogen Energy* **2011**, *36*, 9487–9495, doi:10.1016/j.ijhydene.2011.05.093.

83. Oh, J.-H.; Lee, H.; Kim, D.; Seong, T.-Y. Effect of Ag Nanoparticle Size on the Plasmonic Photocatalytic Properties of TiO2 Thin Films. *Surface and Coatings Technology* **2011**, *206*, 185–189, doi:10.1016/j.surfcoat.2011.07.018.

84. Akhavan, O. Lasting Antibacterial Activities of Ag–TiO2/Ag/a-TiO2 Nanocomposite Thin Film Photocatalysts under Solar Light Irradiation. *Journal of Colloid and Interface Science* **2009**, *336*, 117–124, doi:10.1016/j.jcis.2009.03.018.

85. Borges, J.; Rodrigues, M.S.; Lopes, C.; Costa, D.; Couto, F.M.; Kubart, T.; Martins, B.; Duarte, N.; Dias, J.P.; Cavaleiro, A.; et al. Thin Films Composed of Ag Nanoclusters Dispersed in TiO2: Influence of Composition and Thermal Annealing on the Microstructure and Physical Responses. *Applied Surface Science* **2015**, *358*, 595–604, doi:10.1016/j.apsusc.2015.08.148.

86. Naoi, K.; Ohko, Y.; Tatsuma, T. TiO_2 Films Loaded with Silver Nanoparticles: Control of Multicolor Photochromic Behavior. *J. Am. Chem. Soc.* **2004**, *126*, 3664–3668, doi:10.1021/ja039474z.

87. Ohko, Y.; Tatsuma, T.; Fujii, T.; Naoi, K.; Niwa, C.; Kubota, Y.; Fujishima, A. Multicolour Photochromism of TiO2 Films Loaded with Silver Nanoparticles. *Nature Mater* **2003**, *2*, 29–31, doi:10.1038/nmat796.

88. Roguska, A.; Kudelski, A.; Pisarek, M.; Opara, M.; Janik-Czachor, M. Surface-Enhanced Raman Scattering (SERS) Activity of Ag, Au and Cu Nanoclusters on TiO2-Nanotubes/Ti Substrate. *Applied Surface Science* **2011**, *257*, 8182–8189, doi:10.1016/j.apsusc.2010.12.048.

89. Yang, L.; Jiang, X.; Ruan, W.; Yang, J.; Zhao, B.; Xu, W.; Lombardi, J.R. Charge-Transfer-Induced Surface-Enhanced Raman Scattering on Ag−TiO_2 Nanocomposites. *J. Phys. Chem. C* **2009**, *113*, 16226–16231, doi:10.1021/jp903600r.

90. Bowker, M.; James, D.; Stone, P.; Bennett, R.; Perkins, N.; Millard, L.; Greaves, J.; Dickinson, A. Catalysis at the Metal-Support Interface: Exemplified by the Photocatalytic Reforming of Methanol on Pd/TiO2. *Journal of Catalysis* **2003**, *217*, 427–433, doi:10.1016/S0021-9517(03)00074-5.

91. Zhang, F.; Pi, Y.; Cui, J.; Yang, Y.; Zhang, X.; Guan, N. Unexpected Selective Photocatalytic Reduction of Nitrite to Nitrogen on Silver-Doped Titanium Dioxide. *J. Phys. Chem. C* **2007**, *111*, 3756–3761, doi:10.1021/jp067807j.

92. Kumar, M.; Kumar, T.; Avasthi, D.K. Study of Thermal Annealing Induced Plasmonic Bleaching in Ag:TiO2 Nanocomposite Thin Films. *Scripta Materialia* **2015**, *105*, 46–49, doi:10.1016/j.scriptamat.2015.04.030.

93. Piseri, P.; Podestà, A.; Barborini, E.; Milani, P. Production and Characterization of Highly Intense and Collimated Cluster Beams by Inertial Focusing in Supersonic Expansions. *Review of Scientific Instruments* **2001**, *72*, 2261–2267, doi:10.1063/1.1361082.

94. Perez, A.; Melinon, P.; Dupuis, V.; Jensen, P.; Prevel, B.; Tuaillon, J.; Bardotti, L.; Martet, C.; Treilleux, M.; Broyer, M.; et al. Cluster Assembled Materials: A Novel Class of Nanostructured Solids with Original Structures and Properties. *J. Phys. D: Appl. Phys.* **1997**, *30*, 709–721, doi:10.1088/0022-3727/30/5/003.

95. Haberland, H.; Insepov, Z.; Moseler, M. Molecular-Dynamics Simulation of Thin-Film Growth by Energetic Cluster Impact. *Phys. Rev. B* **1995**, *51*, 11061–11067, doi:10.1103/PhysRevB.51.11061.

96. Peli, S.; Cavaliere, E.; Benetti, G.; Gandolfi, M.; Chiodi, M.; Cancellieri, C.; Giannetti, C.; Ferrini, G.; Gavioli, L.; Banfi, F. Mechanical Properties of Ag Nanoparticle Thin Films Synthesized by Supersonic Cluster Beam Deposition. *J. Phys. Chem. C* **2016**, *120*, 4673–4681, doi:10.1021/acs.jpcc.6b00160.

97. Benetti, G.; Gandolfi, M.; Van Bael, M.J.; Gavioli, L.; Giannetti, C.; Caddeo, C.; Banfi, F. Photoacoustic Sensing of Trapped Fluids in Nanoporous Thin Films: Device Engineering and Sensing Scheme. *ACS Appl. Mater. Interfaces* **2018**, *10*, 27947–27954, doi:10.1021/acsami.8b07925.

98. Benetti, G.; Caddeo, C.; Melis, C.; Ferrini, G.; Giannetti, C.; Winckelmans, N.; Bals, S.; Van Bael, M.J.; Cavaliere, E.; Gavioli, L.; et al. Bottom-Up Mechanical Nanometrology of Granular Ag Nanoparticles Thin Films. *J. Phys. Chem. C* **2017**, *121*, 22434–22441, doi:10.1021/acs.jpcc.7b05795.

99. Doghmane, H.E.; Touam, T.; Chelouche, A.; Challali, F.; Bordji, B. Investigation of the Influences of Post-Thermal Annealing on Physical Properties of TiO2 Thin Films Deposited by RF Sputtering. *Semiconductors* **2020**, *54*, 268–273, doi:10.1134/S1063782620020086.

100. Hou, Y.-Q.; Zhuang, D.-M.; Zhang, G.; Zhao, M.; Wu, M.-S. Influence of Annealing Temperature on the Properties of Titanium Oxide Thin Film. *Applied Surface Science* **2003**, *218*, 98–106, doi:10.1016/S0169-4332(03)00569-5.

101. Mathews, N.R.; Morales, E.R.; Cortés-Jacome, M.A.; Toledo Antonio, J.A. TiO2 Thin Films – Influence of Annealing Temperature on Structural, Optical and Photocatalytic Properties. *Solar Energy* **2009**, *83*, 1499–1508, doi:10.1016/j.solener.2009.04.008.

102. Nes, E. The Effect of a Fine Particle Dispersion on Heterogeneous Recrystallization. *Acta Metallurgica* **1976**, *24*, 391–398, doi:10.1016/0001-6160(76)90059-6.

103. Doherty, R.D.; Hughes, D.A.; Humphreys, F.J.; Jonas, J.J.; Jensen, D.J.; Kassner, M.E.; King, W.E.; McNelley, T.R.; McQueen, H.J.; Rollett, A.D. Current Issues in Recrystallization: A Review. *Materials Science and Engineering: A* **1997**, *238*, 219–274, doi:10.1016/S0921-5093(97)00424-3.

104. Manohar, P.A.; Ferry, M.; Chandra, T. Five Decades of the Zener Equation. *ISIJ International* **1998**, *38*, 913–924, doi:10.2355/isijinternational.38.913.

105. Wörner, C.H.; Hazzledine, P.M. Grain Growth Stagnation by Inclusions or Pores. *JOM* **1992**, *44*, 16–20, doi:10.1007/BF03222320.

106. Hillert, M. Inhibition of Grain Growth by Second-Phase Particles. *Acta Metallurgica* **1988**, *36*, 3177–3181, doi:10.1016/0001-6160(88)90053-3.

107. Wang, G.; Xu, D.S.; Payton, E.J.; Ma, N.; Yang, R.; Mills, M.J.; Wang, Y. Mean-Field Statistical Simulation of Grain Coarsening in the Presence of Stable and Unstable Pinning Particles. *Acta Materialia* **2011**, *59*, 4587–4594, doi:10.1016/j.actamat.2011.04.004.

108. Ng, C.; Cadusch, J.J.; Dligatch, S.; Roberts, A.; Davis, T.J.; Mulvaney, P.; Gómez, D.E. Hot Carrier Extraction with Plasmonic Broadband Absorbers. *ACS Nano* **2016**, *10*, 4704–4711, doi:10.1021/acsnano.6b01108.

109. Robatjazi, H.; Bahauddin, S.M.; Doiron, C.; Thomann, I. Direct Plasmon-Driven Photoelectrocatalysis. *Nano Lett.* **2015**, *15*, 6155–6161, doi:10.1021/acs.nanolett.5b02453.

110. Battiston, G.A.; Gerbasi, R.; Porchia, M.; Marigo, A. Influence of Substrate on Structural Properties of TiO2 Thin Films Obtained via MOCVD. *Thin Solid Films* **1994**, *239*, 186–191, doi:10.1016/0040-6090(94)90849-4.

111. Singh, P.; Kumar, A.; Kaur, D. Substrate Effect on Texture Properties of Nanocrystalline TiO2 Thin Films. *Physica B: Condensed Matter* **2008**, *403*, 3769–3773, doi:10.1016/j.physb.2008.07.021.

112. Schuler, L.P.; Valanoor, N.; Miller, P.; Guy, I.; Reeves, R.J.; Alkaisi, M.M. The Effect of Substrate Material and Postannealing on the Photoluminescence and Piezo Properties of DC-Sputtered ZnO. *Journal of Elec Materi* **2007**, *36*, 507–518, doi:10.1007/s11664-006-0046-8.

113. Lin, X.; Zhang, C.; Yang, S.; Guo, W.; Zhang, Y.; Yang, Z.; Ding, G. The Impact of Thermal Annealing on the Temperature Dependent Resistance Behavior of Pt Thin Films Sputtered on Si and Al2O3 Substrates. *Thin Solid Films* **2019**, *685*, 372–378, doi:10.1016/j.tsf.2019.06.036.

114. McBrayer, J.D.; Swanson, R.M.; Sigmon, T.W.; Bravman, J. Observation of Rapid Field Aided Diffusion of Silver in Metal-oxide-semiconductor Structures. *Appl. Phys. Lett.* **1983**, *43*, 653–654, doi:10.1063/1.94472.

115. Nason, T.C.; Yang, G. -R.; Park, K. -H.; Lu, T. -M. Study of Silver Diffusion into Si(111) and SiO $_2$ at Moderate Temperatures. *Journal of Applied Physics* **1991**, *70*, 1392–1396, doi:10.1063/1.349547.

116. Jiménez, J.A.; Sendova, M. Unfolding Diffusion-Based Ag Nanoparticle Growth in SiO2 Nanofilms Heat-Treated in Air via in Situ Optical Microspectroscopy. *Optical Materials* **2013**, *35*, 968–972, doi:10.1016/j.optmat.2012.11.019.

117. Dobrovinskaya, E.R.; Lytvynov, L.A.; Pishchik, V. Properties of Sapphire. In *Sapphire*; Springer US: Boston, MA, 2009; pp. 55–176 ISBN 978-0-387-85694-0.

118. Wray, K.L.; Connolly, T.J. Thermal Conductivity of Clear Fused Silica at High Temperatures. *Journal of Applied Physics* **1959**, *30*, 1702–1705, doi:10.1063/1.1735040.

119. Xuefeng Li; Shuo Lin; Jinxing Liang; Yupeng Zhang; Oigawa, H.; Ueda, T. Fiber-Optic Temperature Sensor Based on Difference of Thermal Expansion Coefficient Between Fused Silica and Metallic Materials. *IEEE Photonics J.* **2012**, *4*, 155–162, doi:10.1109/JPHOT.2011.2181943.

120. Sugapriya, S.; Sriram, R.; Lakshmi, S. Effect of Annealing on TiO2 Nanoparticles. *Optik* **2013**, *124*, 4971–4975, doi:10.1016/j.ijleo.2013.03.040.

121. Waterhouse, G.I.N.; Bowmaker, G.A.; Metson, J.B. The Thermal Decomposition of Silver (I, III) Oxide: A Combined XRD, FT-IR and Raman Spectroscopic Study. *Phys. Chem. Chem. Phys.* **2001**, *3*, 3838–3845, doi:10.1039/b103226g.

122. Wang, C.-B.; Deo, G.; Wachs, I.E. Interaction of Polycrystalline Silver with Oxygen, Water, Carbon Dioxide, Ethylene, and Methanol: In Situ Raman and Catalytic Studies. *J. Phys. Chem. B* **1999**, *103*, 5645–5656, doi:10.1021/jp984363l.

123. Govorov, A.O.; Richardson, H.H. Generating Heat with Metal Nanoparticles. *Nano Today* **2007**, *2*, 30–38, doi:10.1016/S1748-0132(07)70017-8.

124. Fang, X.; Deng, Y.; Li, J. Plasmon Resonance and Heat Generation in Nanostructures. *Math Methods in App Sciences* **2015**, *38*, 4663–4672, doi:10.1002/mma.3448.

125. Qiu, J.; Wei, W.D. Surface Plasmon-Mediated Photothermal Chemistry. *J. Phys. Chem. C* **2014**, *118*, 20735–20749, doi:10.1021/jp5042553.

126. Al-Amin, Md.; Hemmer, J.V.; Joshi, P.B.; Fogelman, K.; Wilson, A.J. Quantification and Description of Photothermal Heating Effects in Plasmon-Assisted Electrochemistry. *Commun Chem* **2024**, *7*, 70, doi:10.1038/s42004-024-01157-8.

127. Kalteh, M. Investigating the Effect of Various Nanoparticle and Base Liquid Types on the Nanofluids Heat and Fluid Flow in a Microchannel. *Applied Mathematical Modelling* **2013**, *37*, 8600–8609, doi:10.1016/j.apm.2013.03.067.

128. Zhao, W.; Karp, J.M. Nanoantennas Heat Up. *Nature Mater* **2009**, *8*, 453–454, doi:10.1038/nmat2463.

129. Buffat, Ph.; Borel, J.-P. Size Effect on the Melting Temperature of Gold Particles. *Phys. Rev. A* **1976**, *13*, 2287–2298, doi:10.1103/PhysRevA.13.2287.

130. Allen, G.L.; Bayles, R.A.; Gile, W.W.; Jesser, W.A. Small Particle Melting of Pure Metals. *Thin Solid Films* **1986**, *144*, 297–308, doi:10.1016/0040-6090(86)90422-0.

131. Nanda, K.K. Size-Dependent Melting of Nanoparticles: Hundred Years of Thermodynamic Model. *Pramana - J Phys* **2009**, *72*, 617–628, doi:10.1007/s12043-009-0055-2.

132. Baletto, F.; Ferrando, R. Structural Properties of Nanoclusters: Energetic, Thermodynamic, and Kinetic Effects. *Rev. Mod. Phys.* **2005**, *77*, 371–423, doi:10.1103/RevModPhys.77.371.

133. Sheng, H.W. Superheating and Melting-Point Depression of Pb Nanoparticles Embedded in Al Matrices. *Philosophical Magazine Letters* **1996**, *73*, 179–186, doi:10.1080/095008396180812.

134. Sheng, H.W.; Ren, G.; Peng, L.M.; Hu, Z.Q.; Lu, K. Epitaxial Dependence of the Melting Behavior of In Nanoparticles Embedded in Al Matrices. *J. Mater. Res.* **1997**, *12*, 119–123, doi:10.1557/JMR.1997.0019.

135. Zhong, J. Superheating of Ag Nanoparticles Embedded in Ni Matrix. *Acta Materialia* **2001**, *49*, 2897–2904, doi:10.1016/S1359-6454(01)00212-9.

136. R. W. Powell; C. Y. Ho; P. E. Liley *Thermal Conductivity of Selected Materials*; US Department of Commerce, National Bureau of Standards Washington, DC, 1966; Vol. 8;.

137. Letfullin, R.R.; George, T.F.; Duree, G.C.; Bollinger, B.M. Ultrashort Laser Pulse Heating of Nanoparticles: Comparison of Theoretical Approaches. *Advances in Optical Technologies* **2008**, *2008*, 251718, doi:10.1155/2008/251718.

138. Jones, S.; Andrén, D.; Karpinski, P.; Käll, M. Photothermal Heating of Plasmonic Nanoantennas: Influence on Trapped Particle Dynamics and Colloid Distribution. *ACS Photonics* **2018**, *5*, 2878–2887, doi:10.1021/acsphotonics.8b00231.

139. Chen, K.; Feng, X.; Hu, R.; Li, Y.; Xie, K.; Li, Y.; Gu, H. Effect of Ag Nanoparticle Size on the Photoelectrochemical Properties of Ag Decorated TiO2 Nanotube Arrays. *Journal of Alloys and Compounds* **2013**, *554*, 72–79, doi:10.1016/j.jallcom.2012.11.126.

140. Govorov, A.O.; Zhang, H.; Gun'ko, Y.K. Theory of Photoinjection of Hot Plasmonic Carriers from Metal Nanostructures into Semiconductors and Surface Molecules. *J. Phys. Chem. C* **2013**, *117*, 16616–16631, doi:10.1021/jp405430m.

141. Liu, Z.; Destouches, N.; Vitrant, G.; Lefkir, Y.; Epicier, T.; Vocanson, F.; Bakhti, S.; Fang, Y.; Bandyopadhyay, B.; Ahmed, M. Understanding the Growth Mechanisms of Ag Nanoparticles Controlled by Plasmon-Induced Charge Transfers in Ag-TiO2 Films. *J. Phys. Chem. C* **2015**, *119*, 9496–9505, doi:10.1021/acs.jpcc.5b01350.

142. Babonneau, D.; Diop, D.K.; Simonot, L.; Lamongie, B.; Blanc, N.; Boudet, N.; Vocanson, F.; Destouches, N. Real-Time Investigations of Structural and Optical Changes in Photochromic Ag/TiO $_2$ Nanocomposite Thin Films under Laser Irradiation. *Nano Futures* **2018**, *2*, 015002, doi:10.1088/2399-1984/aaa665.

143. Egerton, R.F. *Physical Principles of Electron Microscopy*; Springer US: Boston, MA, 2005; ISBN 978-0-387-25800-3.

144. Feng, D.; Feng, Y.; Yuan, S.; Zhang, X.; Wang, G. Melting Behavior of Ag Nanoparticles and Their Clusters. *Applied Thermal Engineering* **2017**, *111*, 1457–1463, doi:10.1016/j.applthermaleng.2016.05.087.

145. Lee, K.-C.; Lin, S.-J.; Lin, C.-H.; Tsai, C.-S.; Lu, Y.-J. Size Effect of Ag Nanoparticles on Surface Plasmon Resonance. *Surface and Coatings Technology* **2008**, *202*, 5339–5342, doi:10.1016/j.surfcoat.2008.06.080.

146. Liu, P.; Yang, S.; Ma, Y.; Lu, X.; Jia, Y.; Ding, D.; Chen, Y. Design of Ag Nanograting for Broadband Absorption Enhancement in Amorphous Silicon Thin Film Solar Cells. *Materials Science in Semiconductor Processing* **2015**, *39*, 760–763, doi:10.1016/j.mssp.2015.06.047.

147. Biswas, A.; Eilers, H.; Hidden, F.; Aktas, O.C.; Kiran, C.V.S. Large Broadband Visible to Infrared Plasmonic Absorption from Ag Nanoparticles with a Fractal Structure Embedded in a Teflon AF ® Matrix. *Appl. Phys. Lett.* **2006**, *88*, 013103, doi:10.1063/1.2161401.

148. Borges, J.; Pereira, R.M.S.; Rodrigues, M.S.; Kubart, T.; Kumar, S.; Leifer, K.; Cavaleiro, A.; Polcar, T.; Vasilevskiy, M.I.; Vaz, F. Broadband Optical Absorption Caused by the Plasmonic Response of Coalesced Au Nanoparticles Embedded in a TiO 2 Matrix. *J. Phys. Chem. C* **2016**, *120*, 16931–16945, doi:10.1021/acs.jpcc.6b03684.

149. Huang, S.; Wu, C.; Wang, Y.; Yang, X.; Yuan, R.; Chai, Y. Ag/TiO2 Nanocomposites as a Novel SERS Substrate for Construction of Sensitive Biosensor. *Sensors and Actuators B: Chemical* **2021**, *339*, 129843, doi:10.1016/j.snb.2021.129843.

150. Das, S.; Saxena, K.; Mehta, D.S. A Highly Sensitive SERS Substrate Based on a Mesoporous Ag–TiO 2 Thin Film for the Detection of Dye Molecules. *Mater. Adv.* **2022**, *3*, 5337–5343, doi:10.1039/D2MA00211F.

151. Zhang, Y.; Xu, Z.; Wu, S.; Zhu, A.; Zhao, X.; Wang, Y. Enhanced Surface Plasmon by Clusters in TiO2-Ag Composite. *Materials* **2022**, *15*, 7519, doi:10.3390/ma15217519.

152. Liu, Y.; Ma, H.; Han, X.X.; Zhao, B. Metal–Semiconductor Heterostructures for Surface-Enhanced Raman Scattering: Synergistic Contribution of Plasmons and Charge Transfer. *Mater. Horiz.* **2021**, *8*, 370–382, doi:10.1039/D0MH01356K.

153. Renz, M. Fluorescence Microscopy—A Historical and Technical Perspective. *Cytometry Pt A* **2013**, *83*, 767–779, doi:10.1002/cyto.a.22295.

154. Coons, A.H.; Creech, H.J.; Jones, R.N.; Berliner, E. The Demonstration of Pneumococcal Antigen in Tissues by the Use of Fluorescent Antibody. *The Journal of Immunology* **1942**, *45*, 159–170, doi:10.4049/jimmunol.45.3.159.

155. Prasher, D.C.; Eckenrode, V.K.; Ward, W.W.; Prendergast, F.G.; Cormier, M.J. Primary Structure of the Aequorea Victoria Green-Fluorescent Protein. *Gene* **1992**, *111*, 229–233, doi:10.1016/0378-1119(92)90691-H.

156. Heim, R.; Tsien, R.Y. Engineering Green Fluorescent Protein for Improved Brightness, Longer Wavelengths and Fluorescence Resonance Energy Transfer. *Current Biology* **1996**, *6*, 178–182, doi:10.1016/S0960-9822(02)00450-5.

157. Elliott, A.D. Confocal Microscopy: Principles and Modern Practices. *CP Cytometry* **2020**, *92*, e68, doi:10.1002/cpcy.68.

158. Heintzmann, R.; Ficz, G. Breaking the Resolution Limit in Light Microscopy. *Briefings in Functional Genomics and Proteomics* **2006**, *5*, 289–301, doi:10.1093/bfgp/ell036.

159. Huang, B.; Bates, M.; Zhuang, X. Super-Resolution Fluorescence Microscopy. *Annu. Rev. Biochem.* **2009**, *78*, 993–1016, doi:10.1146/annurev.biochem.77.061906.092014.

160. Lippincott-Schwartz, J.; Altan-Bonnet, N.; Patterson, G.H. Photobleaching and Photoactivation: Following Protein Dynamics in Living Cells. *Nat Cell Biol* **2003**, *Suppl*, S7-14.

161. Klar, T.A.; Hell, S.W. Subdiffraction Resolution in Far-Field Fluorescence Microscopy. *Opt. Lett.* **1999**, *24*, 954, doi:10.1364/OL.24.000954.

162. Hell, S.W. Far-Field Optical Nanoscopy. *Science* **2007**, *316*, 1153–1158, doi:10.1126/science.1137395.

163. Rust, M.J.; Bates, M.; Zhuang, X. Sub-Diffraction-Limit Imaging by Stochastic Optical Reconstruction Microscopy (STORM). *Nat Methods* **2006**, *3*, 793–796, doi:10.1038/nmeth929.

164. Betzig, E.; Lewis, A.; Harootunian, A.; Isaacson, M.; Kratschmer, E. Near Field Scanning Optical Microscopy (NSOM). *Biophysical Journal* **1986**, *49*, 269–279, doi:10.1016/S0006-3495(86)83640-2.

165. Ströhl, F.; Kaminski, C.F. Frontiers in Structured Illumination Microscopy. *Optica* **2016**, *3*, 667, doi:10.1364/OPTICA.3.000667.

166. Gustafsson, M.G.L. Nonlinear Structured-Illumination Microscopy: Wide-Field Fluorescence Imaging with Theoretically Unlimited Resolution. *Proc. Natl. Acad. Sci. U.S.A.* **2005**, *102*, 13081–13086, doi:10.1073/pnas.0406877102.

167. Fiolka, R.; Beck, M.; Stemmer, A. Structured Illumination in Total Internal Reflection Fluorescence Microscopy Using a Spatial Light Modulator. *Opt. Lett.* **2008**, *33*, 1629, doi:10.1364/OL.33.001629.

168. Gustafsson, M.G.L.; Shao, L.; Carlton, P.M.; Wang, C.J.R.; Golubovskaya, I.N.; Cande, W.Z.; Agard, D.A.; Sedat, J.W. Three-Dimensional Resolution Doubling in Wide-Field Fluorescence Microscopy by Structured Illumination. *Biophysical Journal* **2008**, *94*, 4957–4970, doi:10.1529/biophysj.107.120345.

169. Wei, F.; Liu, Z. Plasmonic Structured Illumination Microscopy. *Nano Lett.* **2010**, *10*, 2531–2536, doi:10.1021/nl1011068.

170. Wei, F.; Lu, D.; Shen, H.; Wan, W.; Ponsetto, J.L.; Huang, E.; Liu, Z. Wide Field Super-Resolution Surface Imaging through Plasmonic Structured Illumination Microscopy. *Nano Lett.* **2014**, *14*, 4634–4639, doi:10.1021/nl501695c.

171. Sentenac, A.; Belkebir, K.; Giovannini, H.; Chaumet, P.C. High-Resolution Total-Internal-Reflection Fluorescence Microscopy Using Periodically Nanostructured Glass Slides. *J. Opt. Soc. Am. A* **2009**, *26*, 2550, doi:10.1364/JOSAA.26.002550.

172. Ponsetto, J.L.; Bezryadina, A.; Wei, F.; Onishi, K.; Shen, H.; Huang, E.; Ferrari, L.; Ma, Q.; Zou, Y.; Liu, Z. Experimental Demonstration of Localized Plasmonic

Structured Illumination Microscopy. *ACS Nano* **2017**, *11*, 5344–5350, doi:10.1021/acsnano.7b01158.

173. Haug, J.; Palei, M.; Shrout, J.D.; Narimanov, E.; Bohn, P.W.; Hoffman, A.J. Confined Hyperbolic Metasurface Modes for Structured Illumination Microscopy. *Opt. Express* **2021**, *29*, 42331, doi:10.1364/OE.441422.

174. Rizzi, G.; Benetti, G.; Giannetti, C.; Gavioli, L.; Banfi, F. Analytical Model of the Acoustic Response of Nanogranular Films Adhering to a Substrate. *Phys. Rev. B* **2021**, *104*, 035416, doi:10.1103/PhysRevB.104.035416.

175. Bruggeman, D.A.G. Berechnung verschiedener physikalischer Konstanten von heterogenen Substanzen. I. Dielektrizitätskonstanten und Leitfähigkeiten der Mischkörper aus isotropen Substanzen. *Ann. Phys.* **1935**, *416*, 636–664, doi:10.1002/andp.19354160705.

176. Choy, T.C. *Effective Medium Theory: Principles and Applications*; Second edition.; Oxford University Press: Oxford, 2016; ISBN 978-0-19-177417-1.

177. Lehmann, D.; Seidel, F.; Zahn, D.R. Thin Films with High Surface Roughness: Thickness and Dielectric Function Analysis Using Spectroscopic Ellipsometry. *SpringerPlus* **2014**, *3*, 82, doi:10.1186/2193-1801-3-82.

178. Ciambriello, L.; Cavaliere, E.; Gavioli, L. Influence of Roughness, Porosity and Grain Morphology on the Optical Properties of Ultrathin Ag Films. *Applied Surface Science* **2022**, *576*, 151885, doi:10.1016/j.apsusc.2021.151885.

179. Rakić, A.D.; Djurišić, A.B.; Elazar, J.M.; Majewski, M.L. Optical Properties of Metallic Films for Vertical-Cavity Optoelectronic Devices. *Appl. Opt.* **1998**, *37*, 5271, doi:10.1364/AO.37.005271.

180. Yaghmaie, F.; Fleck, J.; Gusman, A.; Prohaska, R. Improvement of PMMA Electron-Beam Lithography Performance in Metal Liftoff through a Poly-Imide Bi-Layer System. *Microelectronic Engineering* **2010**, *87*, 2629–2632, doi:10.1016/j.mee.2010.07.030.

181. Quan, D.; Jia, H.; Li, W.; Cheng, X.; Kwok, H.-S. 77-4: Large Form Birefringence Realized by Dielectric Subwavelength Grating. *Symp Digest of Tech Papers* **2019**, *50*, 1110–1113, doi:10.1002/sdtp.13123.

182. Hotovy, I.; Kostic, I.; Nemec, P.; Predanocy, M.; Rehacek, V. Patterning of Titanium Oxide Nanostructures by Electron-Beam Lithography Combined with Plasma Etching. *J. Micromech. Microeng.* **2015**, *25*, 074006, doi:10.1088/0960-1317/25/7/074006.